UNIWERSYTET ŚLĄSKI W KATOWICACH

Wydział Nauk Ścisłych i Technicznych

Instytut Fizyki im. Augusta Chełkowskiego

PRACA DOKTORSKA

Chelatory żelaza jako inhibitory kinaz tyrozynowych – nowa strategia leczenia glejaka wielopostaciowego

Patryk Zioła

Promotor: dr hab. Anna Mrozek-Wilczkiewicz, prof. UŚ

Promotor pomocniczy: dr Katarzyna Malarz, prof. UŚ

Chorzów, 2026

Autor uzyskał środki finansowe w ramach finansowania projektu badawczego “Chelatory żelaza jako inhibitory kinaz tyrozynowych - nowa strategia leczenia glejaka wielopostaciowego” (2020/39/O/NZ5/02342) z Narodowego Centrum Nauki.

NARODOWE CENTRUM NAUKI

Chciałbym w tym miejscu podziękować moim Promotorkom, dr hab. Annie Mrozek-Wilczkiewicz, prof. UŚ oraz dr Katarzynie Malarz, prof. UŚ, za ich bezgraniczne wsparcie przez cały okres naszej współpracy – zarówno w sferze naukowej, jak i prywatnej. Dzięki ich pomocy oraz wytrwałości, otrzymałem wyjątkową szansę rozwoju.

Moim największym wsparciem przez cały czas doktoratu zawsze była rodzina, w szczególności Żona Weronika oraz nasz Syn Stanisław.

Serdecznie dziękuję Wam, a także wszystkim moim najbliższym - Mamie Iwonie i Ryszardowi, Siostrze Agnieszce i Łukaszowi.

Ogromne podziękowania składam również całemu Zespołowi Biofizyki Farmaceutycznej, każdy z Was przyczynił się do powstania tej pracy.

Spis treści

1. WPROWADZENIE

1.1. Charakterystyka glejaka wielopostaciowego (GBM)

Jednym z największych wyzwań współczesnej medycyny są choroby nowotworowe ze względu na powszechność ich występowania, niedoskonałość profilaktyki oraz trudności w procesie leczenia. Zgodnie z szacunkami Międzynarodowej Agencji Badań nad Rakiem (ang. *International Agency for Research on Cancer*, IACR) z 2022 roku, odnotowano blisko 20 milionów przypadków zachorowań na nowotwory oraz około 9,7 miliona spowodowanych przez nie zgonów. Poszczególne rodzaje nowotworów różnią się od siebie częstością występowania oraz wskaźnikami przeżywalności pacjentów. Jednym z najbardziej śmiertelnych typów są nowotwory mózgu oraz ośrodkowego układu nerwowego (OUN), które były przyczyną około 250 tysięcy zgonów przy 320 tysiącach stwierdzonych nowych przypadków (1). Ze względu na pełnioną funkcję, OUN jest częściowo izolowany od reszty organizmu przez tzw. uprzywilejowanie immunologiczne, m.in. dzięki obecności bariery krew-mózg (ang. *blood-brain barrier*, BBB) (2, 3). Ogranicza ona kontakt komórek nerwowych ze środowiskiem zewnętrznym przy jednoczesnym zapewnieniu im optymalnych warunków do funkcjonowania, lecz stanowi również barierę dla ponad 98% stosowanych terapeutyków, w tym wielu leków stosowanych w terapii przeciwnowotworowej (4).

Najczęściej występującym złośliwym nowotworem mózgu o medianie przeżywalności wynoszącej 14-15 miesięcy jest glejak (ang. *glioblastoma*, GBM) (5). Około 90% przypadków stanowią nowotwory pierwotne, czyli rozwijające się *de novo* ze zdrowych komórek glejowych – rozwój guza w ich przypadku jest bardzo szybki oraz szybko prowadzi do zgonu. Występowanie pierwotnego GBM obserwuje się głównie u osób starszych o medianie wieku wynoszącej 65 lat, w odróżnieniu od rzadziej występujących wtórnych GBM, które zazwyczaj rozwijają się stopniowo z glejaków o niskim stopniu złośliwości, występują u młodszych pacjentów niż w przypadku pierwotnych GBM (mediana wieku 39 lat) i charakteryzują się większą przeżywalnością (6-8). Trudności w leczeniu pierwotnych GBM wynikają również z dużej heterogeniczności guza oraz obecności komórek glejowych o właściwościach komórek macierzystych (ang. *glial stem-like cells,* GSCs), które pełnią ważną rolę w procesach wzrostu guza oraz nabywania oporności na leki i promieniowanie dzięki swojej zdolności do różnicowania oraz naprawy uszkodzonego DNA (9, 10). Dodatkowym czynnikiem

utrudniającym opracowanie skutecznej terapii jest obecność BBB, która uniemożliwia zastosowanie wielu potencjalnie skutecznych leków. Aktualny standard leczenia polega na bezpiecznej resekcji guza, po której pacjent poddany zostaje zlokalizowanej radioterapii połączonej z jednoczesnym przyjmowaniem adiuwantu w postaci temozolomidu. Efektem terapii jest nieznaczne wydłużenie czasu przeżycia pacjentów, lecz wciąż poszukiwane są skuteczniejsze metody walki z GBM w oparciu o najnowsze odkrycia genetyki molekularnej.

1.2. Znaczenie żelaza w rozwoju GBM

Żelazo jest pierwiastkiem odgrywającym bardzo istotną rolę w funkcjonowaniu organizmu człowieka, stanowiąc integralny element budowy blisko 400 białek, w których występuje jako kofaktor w formie wolnych jonów żelaza, hemu lub centrów żelazowo-siarkowych (11). Fizykochemiczne właściwości tego metalu pozwalają mu na swobodną wymianę elektronów poprzez reakcje redoks, dzięki którym enzymy wykorzystujące żelazo mogą brać udział m.in. w transporcie i magazynowaniu tlenu, replikacji DNA, regulacji ekspresji genów oraz transferze elektronów w ramach łańcucha oddechowego (12). Ze względu na rozległe zastosowanie w wielu kluczowych procesach metabolicznych, niedobór żelaza w mikrośrodowisku komórki prowadzi do zaburzenia homeostazy uniemożliwiającego jej prawidłowy rozwój. Pomimo dużej zawartości żelaza w przyrodzie, w większości występuje ono w biologicznie niedostępnej postaci trójwartościowej (Fe^{3+}), dlatego na drodze ewolucji powstały liczne mechanizmy przyswajania żelaza z otoczenia oraz jego wewnętrznego odzyskiwania. W przypadku łatwej dostępności tego pierwiastka istnieje jednak ryzyko nadmiernej akumulacji żelaza, której skutkiem jest powstanie stresu oksydacyjnego. Jednym z produktów reakcji redoks zachodzących z udziałem żelaza, nazywanej reakcją Fentona, jest rodnik hydroksylowy (·OH) będący jedną z reaktywnych form tlenu (RFT) (13). Wysokie stężenie RFT prowadzi do uszkodzenia białek, kwasów nukleinowych oraz peroksydacji lipidów, zwiększa ryzyko wystąpienia mutacji prowadzących do transformacji nowotworowej, a w skrajnych przypadkach może prowadzić do śmierci komórki na drodze ferroptozy. Utrzymanie homeostazy żelaza w komórce stanowi zatem wyzwanie polegające na kontrolowaniu ilości uwolnionych jonów żelaza, magazynowaniu nadmiaru jonów poprzez związanie z uniemożliwiającą zachodzenie reakcji redoks ferrytyną oraz ochronie przed stresem oksydacyjnym (14).

Badania prowadzone na komórkach GBM wskazują na zwiększone zapotrzebowanie na żelazo w porównaniu ze zdrowymi komórkami glejowymi. Jednym z aspektów jest zwiększona proliferacja charakterystyczna dla wszystkich rodzajów nowotworów, która w celu szybszego przeprowadzania podziałów komórkowych wymaga większej ilości wszystkich potrzebnych substratów. Enzymy zależne od żelaza biorą również istotny udział w procesach replikacji DNA oraz regulacji cyklu komórkowego, dodatkowo zwiększając ilość potrzebnego labilnego żelaza wewnątrz GBM (15). Oprócz tego duże znaczenie ma intensywność procesów metabolicznych w komórkach GSC, które nadają guzowi agresywnego charakteru wzrostu oraz uczestniczą w procesie nabywania oporności na leczenie dzięki swojej zdolności do samoodnowy oraz różnicowania. Schonberg i in. (16) wykazali, wykorzystując metodę znakowania radioaktywnego, że komórki GSC pobierają więcej żelaza niż komórki glejaka pozbawione właściwości komórek macierzystych. Większa zawartość jonów żelaza w komórkach GBM może być wykorzystana jako cel terapeutyczny. Zastosowanie chelatorów pozbawia komórkę biodostępnego żelaza, przez co procesy metaboliczne zależne od tego kofaktora zostają zaburzone. Na szczególną uwagę zasługują związki z grupy tiosemikarbazonu, które charakteryzują się zachowaniem zdolności skompleksowanego żelaza do uczestnictwa w reakcjach redoks (17). Potencjalnie skuteczne może być również zwiększone podawanie żelaza celem doprowadzenia do przeładowania komórek oraz powiązanego wzrostu poziomu RFT w komórkach guza. Badania przeprowadzone na modelu *in vitro* przez Trujillo-Alonso i in. udowodniły, że podanie nanocząstek tlenku żelaza wywołuje stres oksydacyjny i prowadzi do śmierci komórkowej (18).

1.3. Znaczenie białka IGF1R oraz jego mutacji w rozwoju GBM

Znaczenie receptorowych kinaz tyrozynowych w regulacji różnych procesów komórkowych, takich jak wzrost i proliferacja komórek, jest zagadnieniem bardzo złożonym i pomimo znajomości mechanizmów związanych z poszczególnymi ścieżkami sygnałowymi pełne zrozumienie interakcji między ligandami, ich receptorami i białkami modulowanymi przez te receptory wciąż wymaga głębszego poznania (19). Jednym z ważniejszych białek należących do tej grupy jest receptor insulinopodobnego czynnika wzrostu 1 (ang. insulin-like growth factor-1 receptor, IGF1R), występujący na powierzchni komórki w formie dimeru zdolnego wiązać się z insulinopodobnymi czynnikami wzrostu 1 i 2 oraz w mniejszym stopniu z insuliną. Jest to receptor blisko

spokrewniony z receptorem insuliny (IR), z którym posiada około 70% wspólnej sekwencji oraz możliwość wiązania tych samych ligandów, a także obserwuje się częściowe oddziaływanie krzyżowe regulowanego sygnału. W związku z tym IGF1R jest w stanie dokonywać transdukcji sygnału w wielu ścieżkach sygnałowych, lecz przede wszystkim odpowiada on za regulację szlaku MAPK/ERK poprzez aktywację białka Ras, a także wykazuje wpływ na ścieżkę PI3K/AKT/mTOR (20, 21).

Receptorowe kinazy tyrozynowe często ulegają zmianom w komórkach nowotworowych, które w efekcie prowadzą do przyspieszenia proliferacji, angiogenezy oraz nabywania oporności na stosowaną terapię. Przykładowo, w wyniku mutacji możliwe jest zwiększenie powinowactwa do ligandu lub wzrost aktywności domeny kinazy tyrozynowej (22). W przypadku białka IGF1R często obserwuje się jego nadekspresję w komórkach GSC, gdzie odpowiada ono za proces autoodnowy oraz poprzez fosforylację białka Akt chroni komórki guza przed wejściem na ścieżkę apoptotyczną (23).

Obecnie, stosowanie inhibitorów kinaz tyrozynowych wzbudza coraz większe zainteresowanie badaczy ze względu na obiecujące wyniki badań przedklinicznych pokazujących ich skuteczność przeciwko komórkom nowotworowym, w tym GBM. Zmniejszenie ekspresji oraz zatrzymanie aktywności receptorów takich jak IGF1R stanowią jedną z metod ukierunkowanego oddziaływania na guza przy zachowaniu bezpieczeństwa zdrowych komórek (24).

1.4. Cel pracy

Wykorzystanie chelatorów żelaza w terapii celowanej przeciwko GBM wciąż jest niedostatecznie zbadanym zagadnieniem. Aktualnie dostępne wyniki badań na modelu *in vitro* oraz badań klinicznych (25, 26) wskazują na duży potencjał ich zastosowania, szczególnie przy równoczesnym oddziaływaniu na inne cele molekularne. Pomysł zaprojektowania chelatorów żelaza z domeną wykazującą powinowactwo do białek receptorowych, czego efektem byłoby wielokierunkowe oddziaływanie na szlaki metaboliczne, stanowi innowacyjne podejście do postawionego problemu. Celem niniejszej pracy było zweryfikowanie słuszności tego założenia poprzez:

- sprawdzenie aktywności przeciwnowotworowej trzech grup związków zdolnych do chelatacji jonów żelaza i dokonanie selekcji najbardziej efektywnych spośród nich,
- analizę interakcji badanych związków z jonami żelaza oraz zdolność do inhibicji wybranych kinaz tyrozynowych,
- ocenę wpływu chelatorów na przebieg cyklu komórkowego, generowanie stresu oksydacyjnego oraz zdolność indukcji apoptozy,
- określenie molekularnego mechanizmu działania aktywnych związków w oparciu o analizę ekspresji białek oraz genów związanych z metabolizmem żelaza, stanowiących część istotnych ścieżek sygnałowych oraz odpowiedzialnych za inicjację procesu apoptozy.

Przedstawione poniżej wyniki otrzymano podczas badań prowadzonych w ramach projektu Narodowego Centrum Nauki PRELUDIUM BIS 2 (2020/39/O/NZ5/02342) pod kierownictwem dr hab. Anny Mrozek-Wilczkiewicz, prof. UŚ, którego byłem wykonawcą.

1.5. Materiały i metody

Wszystkie przedstawione w tej pracy badania zostały wykonane w Zespole Biofizyki Farmaceutycznej w Instytucie Fizyki im. Augusta Chełkowskiego Uniwersytetu Śląskiego w Katowicach, pod kierownictwem dr hab. Anny Mrozek-Wilczkiewicz, prof. UŚ. Promotorem pomocniczym niniejszej pracy jest dr Katarzyna Malarz, prof. UŚ.

1.5.1. Synteza badanych związków

Związki, których właściwości były określane podczas badań zostały zaprojektowane i otrzymane we współpracy z następującymi badaczami:

- synteza bis(terpirydyn) (BC) (**Rys. 1A**) - dr hab. Dawid Zych, prof. UO (Wydział Chemii Uniwersytetu Opolskiego),
- synteza tiosemikarbazonów (TSC) (**Rys. 1B**) - dr hab. Mateusz Korzec oraz dr hab. inż. Maciej Serda, prof. UŚ (Instytut Chemii Uniwersytetu Śląskiego)
- synteza styrylochinolin (SQ) (**Rys. 1C**) - prof. dr hab. Robert Musioł (Instytut Chemii Uniwersytetu Śląskiego).

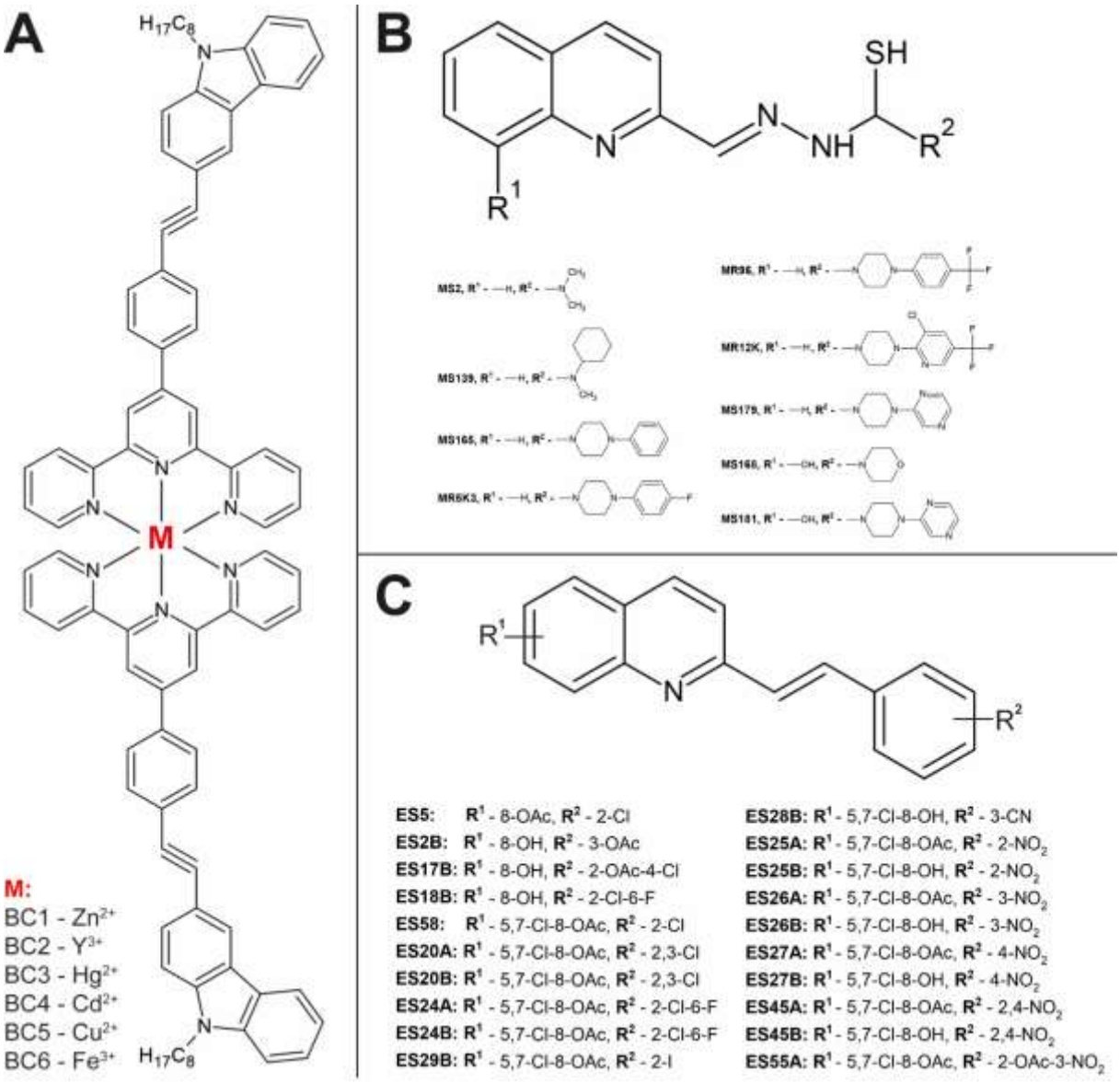

Rys. 1. Struktury badanych związków: **(A)** bis(terpirydyn), **(B)** tiosemikarbazonów, **(C)** styrylochinolin

1.5.2. Hodowla komórek w warunkach in vitro

Podczas prac badawczych wykorzystano następujące ludzkie linie komórkowe: pięć linii glejaka wielopostaciowego LN-18, LN-229, T98G, U-87 MG, U-251; linię gruczolakoraka płuca PC-9; linię gruczolakoraka piersi MCF-7; linię gruczolakoraka trzustki PANC-1 oraz linię prawidłowych fibroblastów NHDF. Linia komórkowa U-251 została udostępniona przez prof. Gabrielę Kramer-Marek (Institute of Cancer Research, Londyn, Wielka Brytania), linię NHDF zakupiono w PromoCell, podczas gdy pozostałe linie komórkowe nabyto w American Type Culture Collection (ATCC).

Hodowlę wszystkich linii komórkowych prowadzono w butelkach o objętości 75 cm^3 (Nunc) w standardowych warunkach – w temperaturze 37°C, w atmosferze wysyconej parą wodną zawierającej 5% CO_2. Linie glejaka hodowano na pożywce Dulbecco's Modified Eagle's Medium (DMEM) suplementowanej 10% v/v płodową surowicą bydlęcą (FBS), natomiast dla linii NHDF stosowano rekomendowaną przez producenta pożywkę Fibroblast Growth Medium (FGM) wraz z suplementem. Obydwie pożywki zostały dodatkowo wzbogacone mieszaniną antybiotyków penicyliny i streptomycyny – 1% v/v w przypadku pożywki DMEM oraz 0,5% v/v dla pożywki FGM. Linie komórkowe poddawano regularnym testom pod kątem potencjalnej kontaminacji bakteriami z rodzaju *Mycoplasma* przy użyciu techniki PCR z zastosowaniem starterów specyficznych wobec genu kodującego 16S rRNA.

1.5.3. Badania cytotoksyczności

Cytotoksyczność na dwuwymiarowym modelu hodowli *in vitro* oznaczano dla wszystkich grup związków przy użyciu testu kolorymetrycznego MTS. Zasada działania tego testu polega na redukcji soli tetrazolowej do barwnego formazanu przez dehydrogenazy znajdujące się w metabolicznie aktywnych komórkach. Ilość produktu reakcji enzymatycznej można oznaczyć ilościowo poprzez pomiar absorbancji.

Komórki wysiano na płytkach 96-dołkowych (Nunc) w ilości 5×10^3 komórek na dołek w objętości 100 µL, za wyjątkiem linii NHDF, której komórki wysiano w ilości 4×10^3 na dołek. Przygotowane w ten sposób płytki inkubowano przez 24 godziny w standardowych warunkach, a następnie podano 200 µL pożywki zawierającej badane związki w różnych stężeniach na okres 72 godzin. Po upłynięciu tego czasu wymieniono pożywkę DMEM na 100 µL świeżej, pozbawionej czerwieni fenolowej oraz 20 µL odczynnika CellTiter 96® AQueous One Solution (Promega). Po trwającej 1 godzinę inkubacji zmierzono absorbancję dla długości fali $\lambda = 490$ nm z użyciem czytnika płytek wielodołkowych (Varioskan LUX, Thermo Scientific). Każdy pomiar został wykonany w duplikacie oraz powtórzony minimum trzykrotnie, znormalizowany do nietraktowanej kontroli, a uzyskane wyniki wykorzystano do obliczenia wartości IC_{50} – stężenia substancji, dla którego proliferacja populacji komórek zostaje spowolniona o 50%. Wartości te obliczono w programie GraphPad Prism 9.

Dodatkowo dla grupy związków TSC sprawdzano cytotoksyczność na trójwymiarowym modelu hodowli sferoidów *in vitro* z użyciem testu CellTiter-Glo® 3D Cell Viability Assay. W wyniku działania odczynnika komórki ulegają lizie, po zakończeniu której uwolnione zostaje znajdujące się w komórkach ATP. Zawarta w odczynniku lucyferaza wchodzi z nim w kontakt i generuje sygnał luminescencyjny, którego wartość można określić przy użyciu spektroskopu.

W badaniach cytotoksyczności na wspomnianym wcześniej modelu wykorzystano wyłącznie komórki glejakowe. Komórki wysiano na nieadherentnych płytkach 96-dołkowych o U-kształtnym dnie (Sarstedt) w ilości 4×10^3 na dołek w objętości 200 µL, a następnie inkubowano je przez 96 godzin w standardowych warunkach. Po zakończeniu procesu formowania sferoidów z dołków ostrożnie usunięto 100 µL pożywki oraz dodano 100 µL pożywki zawierającej badane związki w różnych stężeniach – roztwory przygotowano w stężeniu dwukrotnie wyższym, aby po wymieszaniu z obecnym w dołku medium uzyskać roztwory o oczekiwanym stężeniu. Płytki inkubowano ze związkami przez 72 godziny, a następnie umieszczono w temperaturze pokojowej na około 1 godzinę w celu wyrównania temperatury. Z dołków ponownie usunięto 100 µL pożywki, dodano taką samą objętość odczynnika CellTiter-Glo® 3D Cell Viability Assay Reagent, po czym płytkę wymieszano (600 obrotów na minutę, 5 minut) oraz inkubowano w temperaturze pokojowej kolejne 25 minut. Następnie 100 µL płynu znajdującego się w dołkach przeniesiono do białej, nieprzezroczystej płytki 96-dołkowej i zmierzono luminescencję. Wyniki znormalizowano do nietraktowanej kontroli, które następnie posłużyły do wyznaczenia wartości IC_{50}.

1.5.4. Zestawienie związków wyselekcjonowanych do dalszych badań

Na podstawie wyników testów cytotoksyczności na obydwu modelach komórkowych wybrano najbardziej aktywne związki do dalszych analiz. Wybrane związki, stosowane stężenia oraz przeprowadzone testy zestawiono w **Tabeli 1**.

Tabela 1. Zestawienie związków wybranych do dalszych badań oraz wykorzystywanych stężeń

Nazwa związku	Stosowane stężenie związku	Badania z użyciem związku
MS165 (TSC)	2,5 μM	analiza spektroskopowa, generowanie RFT, inhibicja kinaz, indukcja apoptozy, analiza ekspresji białek
MS179 (TSC)	5 μM	analiza spektroskopowa, generowanie RFT, inhibicja kinaz, indukcja apoptozy, analiza ekspresji białek
MR5K3 (TSC)	1 μM	analiza spektroskopowa, generowanie RFT, inhibicja kinaz, termoforeza mikroskalowa, dokowanie molekularne, indukcja apoptozy, analiza ekspresji białek
MS168 (TSC)	65 μM	analiza spektroskopowa, generowanie RFT, inhibicja kinaz, termoforeza mikroskalowa, dokowanie molekularne, indukcja apoptozy, analiza ekspresji białek, test przenikalności przez BBB
BC2 (BC)	5,1 μM, 10,2 μM, 16,8 μM	zatrzymanie cyklu komórkowego, indukcja apoptozy, generowanie RFT, analiza ekspresji genów, analiza ekspresji białek
ES2B, ES20B, ES25A, ES25B, ES26B, ES28B, ES29B, ES45A, ES45B, ES58 (SQ)	1 μM	inhibicja kinaz, dokowanie molekularne

1.5.5. Zatrzymanie cyklu komórkowego

Komórki wysiano na płytkach 6-dołkowych (Nunc) w ilości 2×10^5 na dołek w objętości 1 mL, które następnie inkubowano przez 24 godziny w standardowych warunkach. Po tym czasie podano świeżo przygotowane roztwory wybranych związków w tej samej objętości i inkubowano przez 24 godziny. Określenie zatrzymania cyklu komórkowego przeprowadzono z wykorzystaniem komercyjnego zestawu Muse Cell Cycle Kit (Millipore) zgodnie z protokołem producenta. Komórki zebrano przy użyciu 0,05% roztworu trypsyny-EDTA, zneutralizowano i zwirowano (300 × g, 5 min.). Następnie pellet komórkowy przemyto buforem PBS, ponownie zwirowano, zawieszono w 1 mL zmrożonego 70% etanolu i umieszczono w temperaturze -20°C na 24 godziny. Następnego dnia utrwalone komórki zwirowano, pellet przemyto PBS, ponownie zwirowano i zawieszono w 200 μL odczynnika Muse Cell Cycle Reagent. Próbki

inkubowano w temperaturze 25°C w ciemności przez 30 minut, po zakończeniu których wykonano pomiary z użyciem cytometru przepływowego Muse Cell Analyzer (Millipore). Eksperymenty wykonano przynajmniej w czterokrotnym powtórzeniu.

1.5.6. Pomiar indukcji apoptozy

Komórki wykorzystane w publikacji [P1] wysiano na płytkach 6-dołkowych (Nunc) zgodnie z protokołem stosowanym podczas badania zatrzymania cyklu komórkowego, a następnie inkubowano przez 24 godziny w standardowych warunkach. W publikacji [P2] komórki wysiano na nieadherentnych płytkach 96-dołkowych o U-kształtnym dnie (Sarstedt) w ilości 4×10^3 na dołek w objętości 200 µL, a następnie inkubowano je przez 96 godzin w standardowych warunkach. Świeżo przygotowane roztwory wybranych związków podano, a płytki inkubowano przez 48 godzin. Do sprawdzenia żywotności populacji traktowanych komórek wykorzystano komercyjny zestaw Muse Annexin V & Dead Cell Kit (Millipore) zgodnie z dostarczonym protokołem. Komórki hodowane na płytkach 6-dołkowych zebrano przy użyciu 0,05% roztworu trypsyny-EDTA, który następnie zneutralizowano i zwirowano (300 × g, 5 min.), natomiast sferoidy hodowane na płytkach 96-dołkowych dysocjowano do pojedynczych komórek z wykorzystaniem roztworu akutazy. Otrzymany pellet przemyto buforem PBS, ponownie zwirowano oraz zawieszono w mieszaninie składającej się z 100 µL odczynnika Annexin V Binding Buffer oraz po 5 µL roztworów barwników: aneksyny V oraz 7-AAD. Po łagodnym wymieszaniu probówki inkubowano w temperaturze 25°C w ciemności przez 15 minut. Próbki bezpośrednio przed pomiarem rozcieńczono 200 µL odczynnika Annexin V Binding Buffer, a następnie przeanalizowano z użyciem cytometru przepływowego Muse Cell Analyzer (Millipore). Eksperymenty wykonano przynajmniej w czterokrotnym powtórzeniu.

1.5.7. Analiza profilu ekspresji genów

Komórki wysiano na płytkach 6-dołkowych (Nunc) w ilości 5×10^5 na dołek w objętości 1 mL, po czym płytki inkubowano przez 24 godziny w standardowych warunkach. Następnego dnia podano świeżo przygotowane roztwory i kontynuowano inkubację w tych samych warunkach przez kolejne 24 godziny. RNA zostało wyizolowane z komórek metodą Chomczyńskiego przy użyciu odczynnika TRIzol

(Ambion). Lizaty komórkowe przeniesiono do probówek zawierających 200 µL chloroformu, a następnie inkubowano w temperaturze 25°C przez 3 minuty i odwirowano (12 000 × g, 20 min, 4 °C). Do nowych probówek przeniesiono fazę wodną i dodano 500 µL izopropanolu, po wymieszaniu probówki inkubowano w temperaturze 25°C przez 10 minut i ponownie odwirowano (12 000 × g, 10 min, 4 °C). Otrzymany osad RNA przemyto trzykrotnie 1 mL 75% etanolu, po każdym płukaniu wirując (7 500 × g, 5 min, 4 °C). Na końcu pellet RNA suszono do momentu odparowania etanolu w temperaturze 25 °C i zawieszono w 20 µL wody z dodatkiem dietylopirowęglanu (ddH_2O-DEPC). Stężenie otrzymanego RNA oraz jego czystość zmierzono spektrofotometrem NanoDrop 2000 (Thermo Scientific™), po czym przeprowadzono syntezę cDNA z wykorzystaniem zestawu ProtoScript II First Strand cDNA Synthesis Kit (New England BioLabs). Mieszanina reakcyjna składała się z 1 µg wyizolowanego RNA i 1 µL startera $d(T)_{23}VN$ uzupełnionych do objętości 8 µL wodą pozbawioną nukleaz, którą po przygotowaniu inkubowano w temperaturze 70 °C przez 5 minut i natychmiast schłodzono na lodzie przez kolejne 5 minut. Do przygotowanych probówek dodano 10 µL gotowych mieszanin M-MuLV Reaction Mix oraz 2 µL M-MuLV Enzyme Mix. Reakcję odwrotnej transkrypcji prowadzono w termocyklerze SimpliAmp™ Thermal Cycler (Thermo Scientific™) w temperaturze 42 °C przez 1 godzinę, po czym probówki umieszczono na 5 minut w temperaturze 80 °C celem inaktywacji enzymu. Mieszaninę reakcyjną rozcieńczono ddH_2O-DEPC do objętości 50 µL i przechowywano w temperaturze -80 °C.

Ilościowa reakcja PCR w czasie rzeczywistym (RT-qPCR) wykonywana była z użyciem termocyklera CTX96 Touch™ Real-Time PCR Detection System (Bio-Rad). W skład mieszaniny reakcyjnej wchodziły: cDNA, 1 µL mieszaniny starterów specyficznych dla poszczególnych genów oraz 10 µL Luna® Universal qPCR Master Mix (New England BioLabs), którą uzupełniono do objętości 20 µL wodą pozbawioną nukleaz. Reakcja przebiegała następująco: wstępna denaturacja (95 °C, 60 s), następnie 40 cykli: denaturacja (95 °C, 15 s), przyłączanie starterów (60 °C, 30 s), wydłużanie (72 °C, 30 s), odczyt płytki. Po zakończeniu wszystkich cykli przeprowadzana była trzystopniowa ocena temperatury topnienia produktów (95 °C, 15 s; 60 °C, 60 s; 95 °C, 15 s). Otrzymane wyniki znormalizowano do genu referencyjnego GAPDH z użyciem metody Livaka i Schmittgena (metoda $2^{-\Delta\Delta CT}$). Każdy eksperyment wykonano w tryplikacie w trzech niezależnych powtórzeniach. Analizę ekspresji genów przeprowadzono z użyciem oprogramowania Bio-Rad CFX Manager 3.1.

Sekwencje mRNA badanych genów pozyskano z bazy National Center for Biotechnology Information (NCBI). Startery dla poszczególnych sekwencji zostały zaprojektowane z użyciem narzędzia Primer-BLAST (NCBI). Syntezę starterów oraz ich oczyszczanie zlecono firmie Sigma-Aldrich.

1.5.8. Analiza profilu ekspresji białek

Podczas badań użyto komórek hodowanych w dwóch modelach: dwuwymiarowej hodowli jednowarstwowej oraz trójwymiarowej hodowli sferoidowej. Komórki wysiano odpowiednio na płytki 6-dołkowe (Nunc) w ilości 5×10^5 na dołek lub na nieadherentne szalki Petriego o średnicy 3 cm (Nunc) w ilości 2×10^5 komórek w objętości 2 mL, po czym płytki inkubowano przez odpowiednio 24 godziny lub 10 dni w standardowych warunkach. W przypadku hodowli sferoidów po upływie 5 dni dolano do szalek dodatkowy 1 mL świeżej pożywki. Po zakończonej inkubacji wymieniono pożywkę na roztwory badanych związków, po czym wznowiono inkubację przez kolejne 24 godziny. Traktowane komórki następnie zebrano, zwirowano (2 000 × rpm, 5 min.) i zawieszono w 300 μL świeżo przygotowanego buforu do radioimmunoprecypitacji (RIPA), zawierającego mieszaniny inhibitorów proteaz i fosfataz oraz kwas wersenowy (EDTA). Probówki umieszczono w łaźni lodowej, następnie inkubowano na kołysce przez 20 minut, zawartość sonikowano przez 15 sekund, po czym uzyskane lizaty ponownie wirowano (10 000 × rpm, 10 min., 4 °C). Otrzymany supernatant przeniesiono do nowych probówek i przechowywano w temperaturze -80 °C. Przed każdą analizą wykonywano pomiar stężenia białka metodą Smitha, z wykorzystaniem komercyjnego zestawu Micro BCA™ Protein Assay Kit (Thermo Scientific™). Test Western Blot, w wyniku którego wykrywano obecność specyficznych białek składa się z następujących etapów: elektroforeza poliakrylamidowa (125 V, 90 min.), transfer białek z żelu na membranę nitrocelulozową (15 V, 90 min.), blokowanie membrany przy użyciu 5% roztworu odtłuszczonego mleka w buforze soli fizjologicznej buforowanej Tris z dodatkiem Tween 20 (TTBS) (60 min.), inkubacja fragmentów membran w roztworach przeciwciał pierwszorzędowych do następnego dnia, płukanie w buforze TTBS (3 razy po 5 min.), inkubacja w roztworach przeciwciał drugorzędowych (60 min.), ponowne płukanie w buforze TTBS (3 razy po 5 min.), inkubacja w substracie chemiluminescencyjnym SuperSignal™ West Pico Chemiluminescent Substrate (Thermo Scientific™) oraz

detekcja sygnału przy użyciu transiluminatora ChemiDoc™ XRS + System (Biorad). Przeciwciała wykorzystane podczas badań zebrano w **Tabeli 2**.

Tabela 2. Zestawienie przeciwciał wykrywanych podczas analizy ekspresji białek oraz publikacji, w których je wykorzystano

Wykrywane białko	Numer katalogowy przeciwciała	Lista publikacji
4F2hc	#47213	[P2]
Akt	#9272	[P1], [P2]
phospho-Akt (Ser473)	#4060	[P1]
BID	#2002	[P1]
cdc2	#9116	[P1]
cdc25c	#4688	[P1]
cyclin A2	#4656	[P1]
cyclin B1	#4138	[P1]
FECH	sc-377377	[P1], [P2]
FXN	STJ113368	[P2]
GPX4	#52455	[P2]
HIF-1α	#14179	[P1]
HO-1	#5853	[P1], [P2]
IDH1	#8137	[P1]
IRP1	#20272	[P2]
IRP2	#37135	[P2]
Mitoferrin 1	26469-1-AP	[P1]
Nrf2	#12721	[P1]
$p21^{Waf1/Cip1}$	#2947	[P1]
$p27^{Kip1}$	#3688	[P1], [P2]
p44/42 MAPK	#9102	[P2]
phospho-p44/42 MAPK	#9101	[P2]
p70 S6 Kinase	#2708	[P1], [P2]
RAS	ab52939	[P2]

1.5.9. Wykrywanie reaktywnych form tlenu (RFT)

Podczas badań użyto komórek hodowanych w dwóch modelach: dwuwymiarowej hodowli jednowarstwowej oraz trójwymiarowej hodowli sferoidowej. Komórki wysiano odpowiednio na płytki 96-dołkowe (Nunc) w ilości 9×10^3 na dołek w objętości 100 µL lub na nieadherentne płytki 96-dołkowe o U-kształtnym dnie (Sarstedt) w ilości 4×10^3

na dołek, po czym płytki inkubowano przez kolejno 24 godziny lub 96 godzin w standardowych warunkach. Po tym czasie podawano badane związki kilkuetapowo, tak aby w momencie odczytu czasy inkubacji wynosiły kolejno 3, 6, 9, 12 oraz 24 godziny, a następnie do wszystkich dołków dodano barwnik fluorescencyjny reagujący z RFT (CellROX® Green Reagent, Molecular Probes) w stężeniu 5 μM. Tak przygotowaną płytkę inkubowano przez 30 minut w standardowych warunkach. Wszystkie dołki następnie płukano trzykrotnie buforem PBS, dodano 100 μL pozbawionej czerwieni fenolowej pożywki DMEM i zmierzono fluorescencję przy długości fali ekscytacji λ = 485 nm.

W celu normalizacji wyników pomiarów fluorescencji barwnika CellROX® Green Reagent, podczas pomiarów na modelu dwuwymiarowym dodano barwnik wiążący się z DNA (Hoechst 33342, Molecular Probes) w stężeniu 4 μg/mL 10 min. przed końcem inkubacji, natomiast po zakończeniu pomiarów na modelu trójwymiarowym wykonano pomiar stężenia białka metodą Smitha opisaną w sekcji 1.4.7.

Wszystkie eksperymenty mierzono w duplikacie, pomiary powtórzono trzykrotnie, a ich wyniki przedstawiono jako poziom RFT w odniesieniu do kontroli negatywnej wyrażony w procentach.

1.5.10. Pomiar stopnia inhibicji kinaz tyrozynowych

Stopień inhibicji wybranych kinaz tyrozynowych przez wyselekcjonowane związki określono z wykorzystaniem dwóch komercyjnie dostępnych zestawów: Kinase Selectivity Profiling System oraz ADP-Glo Kinase Assay (Promega) zgodnie z protokołem dostarczonym przez producenta. Roztwory wyjściowe związków przygotowano w DMSO w stężeniu 100 μM, które następnie rozcieńczono do stężenia 1 μM. Testy przeprowadzano w 384-dołkowej białej płytce przystosowanej do pomiarów luminescencji (Corning). Eksperymenty powtórzono trzykrotnie, a uzyskane wyniki przedstawiono jako procent inhibicji kinazy tyrozynowej po inkubacji ze związkiem.

1.5.11. Termoforeza mikroskalowa

Wszystkie pomiary termoforezy mikroskalowej wykonano przy użyciu sprzętu Monolith NT.115 Blue/Red (NanoTemper Technologies). Technika ta wykorzystuje zmiany w fluorescencji wyznakowanych cząsteczek wynikające z interakcji z ligandem

oraz ze zjawiska termoforezy, czyli ukierunkowanego ruchu cząsteczek w środowisku o zmiennej temperaturze. W wyniku kontaktu kinazy tyrozynowej z badanym związkiem dochodzi do zmiany otoczki solwatacyjnej wokół białka, która wpływa na jego szybkość ruchu w gradiencie temperatury. Różnice w intensywności fluorescencji wynikające z szybkości przemieszczania się białka inkubowanego w różnych stężeniach ligandu są mierzone i analizowane, w efekcie czego określona zostaje stała powinowactwa (K_D).

1.5.12. Pomiary chelatacji jonów żelaza

Zdolność badanych związków do chelatowania jonów żelaza (III) oceniano poprzez analizę spektroskopową UV-Vis. Przygotowano roztwory wyjściowe w DMSO o stężeniu 8,358 mM, następnie roztwory rozcieńczano wodą do stężenia 100 µM. Do dołków płytki 96-dołkowej z przezroczystym dnem (Nunc) wprowadzano 100 µL przygotowanego roztworu oraz 100 µL roztworów o stopniowo zwiększanym stężeniu jonów żelaza (III) w zakresie 0–100 µM, które po wymieszaniu dawały mieszaninę związku o stężeniu 50 µM i jonów żelaza o stężeniach 0-50 µM. Po 4 godzinach inkubacji w temperaturze pokojowej rejestrowano widma absorpcyjne przy użyciu czytnika mikropłytek Varioskan LUX (ThermoFisher) w przedziale 275–800 nm, z krokiem co 5 nm. Uzyskane dane przedstawiono graficznie oraz poddano analizie z wykorzystaniem programu OriginPro (OriginLab Corporation).

1.5.13. Analiza statystyczna

Wyniki przedstawiono w formie średniej arytmetycznej ± odchylenie standardowe (SD), obliczone na podstawie co najmniej trzech niezależnych eksperymentów. Analizy statystyczne wykonano z wykorzystaniem programu GraphPad Prism 9 (GraphPad Software), stosując analizę wariancji (ANOVA) oraz test post-hoc Tukeya. Za istotne statystycznie uznawano różnice przy poziomie $p < 0,05$.

2. WYNIKI I DYSKUSJA

2.1. Cytotoksyczność analizowanych związków

Badania rozpoczęto od oceny aktywności przeciwnowotworowej wszystkich zaprojektowanych chelatorów w celu znalezienia związków najsilniej spowalniających proliferację komórek GBM, prowadząc do ich śmierci komórkowej. Selekcja substancji o najsilniejszym efekcie cytotoksycznym do dalszych badań jest istotna, ponieważ związki nieaktywne w warunkach hodowli *in vitro* nie mogą stanowić podstawy skutecznego leczenia nowotworu występującego u pacjenta.

Badania cytotoksyczności wykonano kolejno na dwóch modelach badawczych: hodowli dwuwymiarowej oraz trójwymiarowej *in vitro*. Wyniki z modelu dwuwymiarowego opisane w publikacjach [P1-3] zestawiono w **Tabeli 3**, natomiast wyniki z modelu trójwymiarowego zastosowanego w publikacji [P2] przedstawiono w **Tabeli 4**. Na tej podstawie można zaobserwować, że aktywność antyproliferacyjna badanych pochodnych na modelu dwuwymiarowym jest bardzo zróżnicowana i zależna od rodzaju obecnych grup funkcyjnych lub skompleksowanych jonów. Oprócz tego każda z badanych linii komórkowych wykazywała się różnym stopniem wrażliwości na chelatory – największą opornością wykazała się linia T98G, natomiast najbardziej podatna zazwyczaj była linia U-251. Należy jednak zaznaczyć, że nie zaobserwowano takiej zależności dla związków referencyjnych: erlotinibu i osimertinibu, które wykazywały się brakiem albo słabym efektem cytotoksycznym na wszystkich badanych liniach. Badania cytotoksyczności wykonano także na prawidłowej linii fibroblastów NHDF, dzięki którym możliwe było określenie selektywności chelatorów wobec komórek zdrowych. Większość związków nie oddziaływała w żadnym lub wpływała w znikomym stopniu na zahamowanie proliferacji linii NHDF. W pojedynczych przypadkach obserwowano istotny efekt cytotoksyczny uniemożliwiający bezpieczne zastosowanie chelatora w terapii.

Kompleksy BC różniły się między sobą rodzajem skompleksowanego jonu metalu, który bierze aktywny udział w procesie transferu elektronów w reakcji rodnikowej. Spośród wszystkich badanych pochodnych terpirydyny najniższą wartość IC_{50} odnotowano dla pochodnej BC5 z jonami Cu^{2+} wynoszącą 0,36 μM w przypadku linii

komórkowej PC-9 (rak płuc). Związek ten wykazał najwyższą aktywność we wszystkich badanych liniach, gdzie wartość IC_{50} wynosiła poniżej 2 μM dla czterech badanych linii komórkowych (PC-9, U-251 (GBM), MCF-7).

W przypadku związków TSC, przedstawionych w publikacji [P2], kluczowy wpływ na hamowanie proliferacji komórek nowotworowych miała struktura wiodąca chinoliny (**Rysunek 1**, B) połączona z fragmentem tiosemikarbazonu. W pracy tej zebrano najbardziej aktywne pochodne syntezowane przez zespół na przestrzeni lat. Z wcześniej przeprowadzonej analizy struktura-aktywność wynika, iż podstawienie pierścienia chinoliny grupą hydroksylową wpływa pozytywnie na aktywność całej molekuły, prawdopodobnie wpływając na jej lipofilowość, Ponadto fragmenty piperazyny oraz morfoliny przyłączone do części tiosemikarbazonowej wytypowano jako potencjalne farmakofory wpływające pozytywnie na aktywność związku.

Dla grupy związków SQ, istotny wpływ na aktywność przeciwnowotworową miała obecność dwóch podstawników chlorowych w pozycjach 5 oraz 7 pierścienia chinolinowego - chelatory je posiadające wykazywały się większym efektem cytotoksycznym. W przypadku par związków różniących się podstawnikiem w pozycji 8, obecność grupy hydroksylowej również korelowała z większą aktywnością biologiczną. Kolejnym czynnikiem determinującym skuteczność badanych styrylochinolin była ilość oraz pozycja grup nitrowych na pierścieniu fenylowym. Najbardziej aktywne związki posiadały dwa takie podstawniki w pozycjach orto oraz para, podczas gdy obecność jednego podstawnika najczęściej skutkowała przeciętnym efektem cytotoksycznym.

Porównując wartości parametru IC_{50} pomiędzy modelem dwu- oraz trójwymiarowym przedstawione w publikacji [P2], zaobserwować można zwiększenie oporności komórek uformowanych w sferoidy na działanie badanych związków, co wynika z utrudnionego dostępu chelatorów do wnętrza sferoidu. Różnice te są skutkiem innej organizacji przestrzennej – w modelu dwuwymiarowym, wszystkie komórki mają identyczny dostęp do składników odżywczych oraz tlenu, podczas gdy w modelu trójwymiarowym pojawiają się gradienty tych czynników, będące efektem wydłużonego procesu dyfuzji substancji, w tym badanych związków, do wnętrza sferoidu. Model trójwymiarowy również wierniej odwzorowuje interakcje międzykomórkowe, takich jak występowanie efektu Warburga, tj. wykorzystywania procesu fermentacji mlekowej zamiast oddychania

tlenowego w celu pozyskiwania energii z glukozy pomimo obecności tlenu w mikrośrodowisku guza oraz zwiększona tolerancja na niedobór składników odżywczych (27). Wyjątkiem była linia T98G, gdzie w większości związków zauważono odwrotny trend zwiększonej wrażliwości na działanie TSC w sferoidach glejakowych. Pomiędzy poszczególnymi liniami komórkowymi GBM występują różnice w odpowiedzi na stres oksydacyjny. Spośród wybranych linii, T98G charakteryzuje się nadekspresją genów biorących udział w regulacji obrony antyoksydacyjnej, która z uwagi na prezentowane w dalszej części pracy znaczenie generowania RFT przez badane chelatory podczas traktowania, może tłumaczyć występowanie tych znaczących różnic w efekcie cytotoksycznym (28). Drugą niespodziewaną zależnością był znaczący spadek aktywności związków MS168 oraz MS181 w tym modelu. Obie badane pochodne posiadają grupę hydroksylową w pierścieniu chinolinowym. Obliczone współczynniki lipofilowości tych dwóch związków różnią się znacząco od pozostałych, co może wpływać na ich zdolność penetracji sferoidów.

Ostatnim etapem badań toksyczności związków było wykorzystanie w publikacji [P2] modelu badawczego *in vivo* w postaci ksenoprzeszczepów linii LN-229 i zarodków danio pręgowanego (*Danio rerio)*, których celem było potwierdzenie selektywności wybranych TSC wobec komórek nowotworowych oraz zachowanie aktywności antyproliferacyjnej w modelu lepiej odwzorowującym rzeczywiste warunki występujące w guzie. Otrzymane wartości stężenia śmiertelnego LC_{50} dla związków MS165, MS168 i MS181 (odpowiednio 6,221, 6,772 i 8,341 μM) były wielokrotnie wyższe w porównaniu z wartościami IC_{50} otrzymanymi na modelu dwuwymiarowym *in vitro*. W dalszych badaniach, sprawdzano zdolność TSC podawanych w bezpiecznych dla zarodków stężeniach od 0,5, 1 i 2,5 μM do zmniejszenia wielkości ksenoprzeszczepów. Stwierdzono zauważalne zmniejszenie guza, jednakże efekt terapeutyczny był ograniczony. Potencjalne przyczyny mogą wynikać z większej złożoności stosowanego modelu lub konieczności wydłużenia czasu terapii.

Otrzymane wyniki badań cytotoksyczności w modelach *in vitro*, zestawione w **Tabelach 3-4**, wykorzystano podczas selekcji najbardziej aktywnych związków, które poddano dalszym analizom, a także określenia wartości stężeń stosowanych podczas inkubacji w badaniach biologicznych.

Tabela 3. Zestawienie wyników cytotoksyczności na modelu dwuwymiarowym *in vitro* komórek wybranych linii GBM oraz linii prawidłowej NHDF z publikacji [P1-3], kursywą zaznaczono związki stanowiące kontrolę pozytywną

Lp.	Nazwa [publikacja]	Aktywność antyproliferacyjna IC_{50} [µM]					
		LN-18	LN-229	T98G	U-87 MG	U-251	NHDF
1.	BC1 [P1]	nb	nb	nb	18,22 ± 2,43	9,09 ± 0,56	>25
2.	BC2 [P1]	nb	nb	nb	1,57 ± 0,18	0,61 ± 0,07	>25
3.	BC3 [P1]	nb	nb	nb	2,35 ± 0,27	0,84 ± 0,05	>25
4.	BC4 [P1]	nb	nb	nb	3,27 ± 0,59	0,74 ± 0,19	>25
5.	BC5 [P1]	nb	nb	nb	2,16 ± 0,24	0,36 ± 0,10	6,27 ± 1,03
6.	BC6 [P1]	nb	nb	nb	>25	>25	>25
7.	MS2 [P2]	0,257 ± 0,043	0,035 ± 0,008	6,914 ± 1,179	nb	0,040 ± 0,004	10,58 ± 4,07
8.	MS139 [P2]	0,581 ± 0,070	0,328 ± 0,044	>25	nb	0,069 ± 0,007	14,49 ± 2,25
9.	MS165 [P2]	1,774 ± 0,556	0,160 ± 0,015	>25	nb	0,040 ± 0,014	0,033 ± 0,007
10.	MS179 [P2]	1,643 ± 0,243	0,395 ± 0,112	6,883 ± 0,881	nb	0,489 ± 0,186	9,440 ± 3,840
11.	MR5K3 [P2]	3,760 ± 0,579	0,096 ± 0,033	>25	nb	0,104 ± 0,019	0,143 ± 0,021
12.	MR96 [P2]	0,160 ± 0,062	0,073 ± 0,014	15,56 ± 1,46	nb	0,091 ± 0,004	16,66 ± 5,57
13.	MR12K [P2]	11,74 ± 1,42	0,250 ± 0,068	18,49 ± 0,52	nb	0,341 ± 0,098	22,34 ± 1,36
14.	MS168 [P2]	0,103 ± 0,016	0,021 ± 0,004	>25	nb	0,003 ± 0,001	10,64 ± 3,48
15.	MS181 [P2]	9,399 ± 0,957	0,087 ± 0,009	>25	nb	0,046 ± 0,018	12,14 ± 3,58
16.	ES5 [P3]	4,107 ± 0,568	>25	>25	7,700 ± 0,906	>25	nb
17.	ES2B [P3]	6,659 ± 0,564	10,64 ± 0,705	>25	10,68 ± 0,470	18,08 ± 0,755	nb
18.	ES17B [P3]	>25	>25	>25	16,04 ± 1,020	>25	nb
19.	ES18B [P3]	>25	>25	>25	>25	>25	nb
20.	ES58 [P3]	12,91 ± 1,505	12,76 ± 2,125	>25	2,800 ± 0,547	10,71 ± 0,805	nb
21.	ES20A [P3]	>25	>25	>25	16,10 ± 2,670	>25	nb
22.	ES20B [P3]	1,459 ± 0,458	>25	>25	6,983 ± 0,984	>25	nb
23.	ES24A [P3]	>25	>25	>25	10,31 ± 1,199	>25	nb
24.	ES24B [P3]	>25	>25	>25	3,293 ± 0,822	>25	nb
25.	ES29B [P3]	6,535 ± 1,094	11,43 ± 1,520	>25	1,713 ± 0,391	2,606 ± 0,815	nb
26.	ES28B [P3]	8,619 ± 1,038	>25	>25	3,925 ± 0,801	3,880 ± 0,639	nb
27.	ES25A [P3]	4,469 ± 0,566	9,102 ± 0,733	18,36 ± 1,850	1,210 ± 0,327	7,897 ± 0,726	nb
28.	ES25B [P3]	6,030 ± 0,786	>25	>25	2,931 ± 0,433	6,843 ± 0,820	nb
29.	ES26A [P3]	8,459 ± 0,474	9,818 ± 1,305	>25	8,768 ± 1,297	5,188 ± 0,732	nb
30.	ES26B [P3]	10,18 ± 1,567	10,82 ± 1,510	>25	11,66 ± 1,700	6,753 ± 1,224	nb
31.	ES27A [P3]	13,39 ± 2,380	13,82 ± 1,810	>25	14,65 ± 1,660	7,097 ± 0,331	nb
32.	ES27B [P3]	11,30 ± 0,455	9,327 ± 1,492	>25	7,972 ± 0,705	8,013 ± 1,807	nb
33.	ES45A [P3]	2,393 ± 0,645	13,42 ± 2,075	>25	2,444 ± 0,392	1,068 ± 0,472	nb
34.	ES45B [P3]	2,903 ± 0,860	7,526 ± 0,795	>25	1,130 ± 0,242	0,258 ± 0,065	nb
35.	ES55A [P3]	>25	19,36 ± 1,585	>25	11,92 ± 1,245	8,320 ± 1,222	nb
36.	*Erlotinib [P3]*	>25	>25	>25	>25	>25	nb
37.	*Osimertinib [P1-2]*	7,353 ± 0,268	8,986 ± 0,367	7,314 ± 2,187	11,24 ± 0,46	20,13 ± 0,34	6,269 ± 0,375

nb – nie badano

Tabela 4. Zestawienie wyników cytotoksyczności na modelu trójwymiarowym *in vitro* komórek wybranych linii GBM z publikacji [P2] oraz współczynnik lipofilowości badanych TSC, kursywą zaznaczono związek będący kontrolą pozytywną

Lp.	Nazwa	Aktywność antyproliferacyjna IC_{50} [μM]				Współczynnik lipofilowości (logP)
		LN-18	LN-229	T98G	U-251	
1.	**MS2**	0,908 ± 0,200	2,535 ± 0,965	31,33 ± 5,14	0,905 ± 0,215	2,02 ± 0,60
2.	**MS139**	5,162 ± 0,988	1,342 ± 0,405	4,355 ±0,883	0,738 ± 0,108	4,08 ± 0,60
3.	**MS165**	1,027 ± 0,235	2,974 ± 0,987	2,927 ± 0,221	2,472 ± 0,716	2,99 ± 0,66
4.	**MS179**	4,151 ± 0,539	22,49 ± 3,91	4,138 ± 1,236	4,175 ± 0,930	1,64 ± 0,69
5.	**MR5K3**	1,292 ± 0,316	2,927 ± 0,974	1,507 ± 0,610	0,691 ± 0,197	3,08 ± 0,98
6.	**MR96**	7,053 ± 1,091	0,790 ± 0,230	7,170 ± 1,217	0,333 ± 0,058	4,24 ± 0,68
7.	**MR12K**	7,664 ± 1,624	7,721 ± 1,794	0,855 ± 0,208	8,178 ± 1,270	5,12 ± 0,70
8.	**MS168**	177,4 ± 4,6	17,58 ± 3,01	>200	64,84 ± 8,98	1,03 ± 0,90
9.	**MS181**	28,76 ± 6,47	19,93 ± 2,76	65,13 ±11,13	45,07 ± 6,97	1,42 ± 0,97
10.	***Osimertinib***	45,06 ± 5,22	16,41 ± 4,31	29,75 ± 5,05	29,98 ± 6,53	3,30 ± 0,65

2.2. Chelatacja jonów żelaza

W celu wstępnej weryfikacji oddziaływania TSC na gospodarkę żelaza w komórce, w ramach publikacji [P2] przeprowadzono eksperymenty polegające na analizie widm absorpcji roztworów badanych związków oraz ich mieszanin w rosnącym stężeniu jonów Fe^{3+}. Pomiary wykonano bezpośrednio po przygotowaniu roztworów oraz po 4-godzinnej inkubacji, w trakcie której dochodziło do ustalenia równowagi pomiędzy wolnymi ligandami TSC a ich kompleksami z jonami żelaza. Dla większości chelatorów maksimum pasma absorpcji wolnego związku obserwowano przy długości fali około 340 nm, natomiast pasmo absorpcji kompleksu o rosnącej absorbancji wraz ze wzrostem stężenia jonów żelaza pojawiało się w okolicy 430 nm. Podobnie jak podczas badań cytotoksyczności, odmiennym zachowaniem wykazywały się związki MS168 oraz MS181, których pasmo absorpcji wykryto przy długości fali 305 nm. Pomiędzy pasmami formy wolnej oraz związanej z metalem zaobserwowano punkt izozbestyczny, natomiast wymienione wcześniej dwa związki posiadały dwa ukryte punkty izozbestyczne – zauważalne dopiero po normalizacji zmierzonych widm. Świadczy to o tym, że dla związków MS168 i MS181 mechanizm wiązania z jonami żelaza jest bardziej złożony, w trakcie którego mogą występować przejściowe stany równowagi oraz stopniowe tworzenie się kompleksów. Stechiometrię wiązania jonów metalu określono poprzez sporządzenie wykresów zależności absorbancji od stosunku molowego metal:ligand. Dla większości badanych TSC stwierdzono stechiometrię (L:M) 2:1, podczas gdy wyróżniające się MS168 i MS181 wykazują stechiometrię 1:1.

2.3. Inhibicja kinazy IGF1R

Drugim potencjalnym celem molekularnym w planowanej terapii było zaburzenie aktywności białek receptorowych modulujących aktywność ścieżek sygnałowych regulujących metabolizm, wzrost i proliferację komórki. W publikacjach [P2] i [P3] sprawdziliśmy zdolność chelatorów do inhibicji panelu ośmiu receptorowych kinaz tyrozynowych: IGF1R, receptora insuliny (ang. *insulin receptor*, InsR), receptora naskórkowego czynnika wzrostu (ang. *epidermal growth factor receptor*, EGFR), receptorów 2 i 4 ludzkiego naskórkowego czynnika wzrostu (ang. *human epidermal growth factor receptor 2*, HER2 oraz *human epidermal growth factor receptor 4*, HER4), receptora 2 naczyniowo-śródbłonkowego czynnika wzrostu (ang. *kinase insert domain receptor*, KDR) oraz receptorów alfa i beta płytkopochodnego czynnika wzrostu (ang. *platelet-derived growth factor receptor alpha*, PDGFRa oraz *platelet-derived growth factor receptor beta*, PDGFRb). Wyniki pomiarów nie potwierdziły powinowactwa badanych związków do nich, z wyjątkiem kinazy IGF1R. Wobec tego białka, obserwowano szeroki zakres inhibicji od jej całkowitego braku do około 66 % zmniejszenia aktywności enzymatycznej (**Tabela 5**). W przypadku styrylochinolin analizowanych w publikacji [P3], zauważono istotny wpływ grup nitrowych obecnych w grupie styrylowej na powinowactwo do kinazy IGF1R, mogący wynikać ze specyficznego rozkładu ładunku w tym fragmencie cząsteczki. Aby potwierdzić wstępną hipotezę, przeprowadzono badania dokowania molekularnego, które wykazały możliwość tworzenia licznych, zróżnicowanych wiązań pomiędzy ligandami SQ a miejscem aktywnym IGF1R. Najsilniejsze inhibitory tworzyły liczne wiązania z aminokwasami Met1082 oraz Lys1033, co było główną różnicą pomiędzy nimi a słabszymi inhibitorami. W przypadku publikacji [P2] najsilniejsze powinowactwo do białka IGF1R odnotowano dla związków MS168 i MR5K3, dla których zmierzono przy użyciu termoforezy mikroskalowej stałe powinowactwa K_D wynoszące kolejno 720 i 907 nM, potwierdzające ich wysoką selektywność wobec analizowanego receptora. Dodatkowe informacje dotyczące charakteru wiązania ligandów z miejscem aktywnym dostarczyło dokowanie molekularne. Okazało się, że charakter interakcji wybranych TSC różnił się od siebie – w przypadku MR5K3 obserwowano przede wszystkim konformację skierowaną na zewnątrz centrum aktywnego oraz obecność wiązań wodorowych w *kinase hinge region*, w tym aminokwasu Met1082. MS168 tworzył wiązania w konformacji

skierowanej do wnętrza kieszeni enzymu, co skutkowało brakiem wiązań z resztą Met1082. Prawdopodobną przyczyną odmiennego zachowania MS168 jest obecność grupy hydroksylowej w pierścieniu chinolinowym, która istotnie zmienia rozkład ładunku w cząsteczce, zaobserwowany wcześniej w ramach badań chelatacji jonów żelaza.

Tabela 5. Wartości stopnia inhibicji kinazy IGF1R przez związki (stężenie 1 μM) badane w publikacjach [P2] i [P3].

Lp.	Nazwa związku [publikacja]	Stopień inhibicji IGF1R [%]
1.	**ES2B [P3]**	62,95
2.	**ES20B [P3]**	18,66
3.	**ES25A [P3]**	8,25
4.	**ES25B [P3]**	6,35
5.	**ES26B [P3]**	9,31
6.	**ES28B [P3]**	11,17
7.	**ES29B [P3]**	18,08
8.	**ES45A [P3]**	61,56
9.	**ES45B [P3]**	51,59
10.	**ES58 [P3]**	58,00
11.	**MS2 [P2]**	9,00
12.	**MS139 [P2]**	29,77
13.	**MS165 [P2]**	0
14.	**MS179 [P2]**	8,50
15.	**MR5K3 [P2]**	61,90
16.	**MR96 [P2]**	39,00
17.	**MR12K [P2]**	18,56
18.	**MS168 [P2]**	65,85
19.	**MS181 [P2]**	1,20
20.	***Osimertinib [P2]***	57,11

2.4. Wpływ chelatorów na procesy zachodzące w komórkach

Określenie stopnia aktywności antyproliferacyjnej oraz interakcji pomiędzy chelatorami a jonami metali i receptorowymi kinazami tyrozynowymi nie pozwala na pełne poznanie molekularnego mechanizmu działania badanych związków. Aby lepiej zrozumieć wpływ chelatorów na komórki GBM, w ramach publikacji [P1] i [P2] konieczne było wykonanie szeregu analiz efektów ich działania.

W pierwszym etapie prac nad publikacją [P1] zdecydowaliśmy się na wykonanie badań cytometrii przepływowej w celu określenia, czy i na którym etapie dochodzi do zatrzymania cyklu komórkowego. Technika polegająca na oznakowaniu utrwalonych komórek barwnikiem fluorescencyjnym wiążącym się z DNA pozwala w łatwy sposób określić, na którym etapie cyklu komórkowego się one znajdowały. Badania prowadzone na komórkach linii U-251 traktowanych związkiem BC2 w różnych stężeniach wykazały zwiększenie procentowego udziału subpopulacji komórek w fazie G0/G1 z około 49% do około 56%, co wskazuje na zaburzenie przez ten związek procesów metabolicznych regulujących przejście komórki do fazy S. Wcześniejsze wyniki badań prowadzonych w ramach Zespołu Biofizyki Farmaceutycznej na związkach o podobnej budowie cząsteczkowej również wskazywały na występowanie zahamowania progresji cyklu komórkowego w tej fazie (29). Otrzymane wyniki następnie zweryfikowano podczas analizy ekspresji białek, opisanej w dalszej części pracy.

W obydwu publikacjach przeprowadzono również badania indukcji apoptozy z wykorzystaniem cytometrii przepływowej. Barwienie populacji traktowanych komórek fluorescencyjnie oznakowaną aneksyną V skutkuje obecnością sygnału jedynie w tych komórkach, w których doszło do utraty integralności błony komórkowej w wyniku rozpoczęcia procesu apoptozy. Dodatkowe zastosowanie barwnika 7-AAD, wykazującego silne powinowactwo do DNA, lecz niezdolnego do przeniknięcia przez błonę komórkową, pozwala na odróżnienie komórek martwych od żywych. Uzyskane wyniki wskazały na obecność dużej subpopulacji komórek apoptotycznych. W wyniku traktowania związkiem BC2, w zależności od stężenia, ilość żywych komórek linii U-251 spadła z około 91% do 41-64%, przy jednoczesnym zwiększeniu udziału komórek na wczesnym (około 7% w kontroli negatywnej, 21-54% w komórkach poddanych działaniu BC2) i późnym (około 2% w kontroli negatywnej, 9-15% w komórkach traktowanych BC2) etapie apoptozy. Podobny efekt wykazano podczas badania wpływu związków z grupy TSC na modelu sferoidowym, gdzie całkowita ilość komórek

apoptotycznych w kontroli negatywnej wynosiła około 35%, podczas gdy po zakończeniu traktowania wartości te wynosiły od około 55% dla związku MR5K3, do około 75% dla związku MS168. Zaobserwowano również korelację pomiędzy stężeniem stosowanym podczas inkubacji a wielkością wspomnianej subpopulacji. W publikacji [P1] zdecydowano się dokładniej zbadać ten aspekt działania związku BC2 poprzez analizę ekspresji genów oraz białek.

Ze względu na udział jonów żelaza w reakcjach redoks, których produktem są RFT oraz możliwość dalszego przebiegu tych reakcji po skompleksowaniu jonów przez badane chelatory, istotne było wykonanie pomiaru ilości RFT w traktowanych komórkach. Wykorzystano w tym celu barwnik CellROX® Green Reagent, który w wyniku utlenienia po kontakcie z RFT generuje silny sygnał zielonej fluorescencji. Barwnik ten może swobodnie przenikać błony biologiczne, dzięki czemu stanowi dobry wskaźnik ilościowy RFT w komórce. Wyniki pomiarów fluorescencji udowodniły zdolność związku BC2 oraz wybranych TSC do wywoływania stresu oksydacyjnego odpowiednio w modelu dwu- i trójwymiarowym *in vitro*. Wraz z wydłużeniem czasu inkubacji z chelatorami rosła też ilość generowanych RFT, najlepiej obserwowana podczas inkubacji sferoidów linii U-251 ze związkami TSC. Dla związku MS165 zaobserwowano najwyższy relatywny poziom RFT po upływie 24 godzin wynoszący około 126% względem kontroli negatywnej, podczas gdy pozostałe związki powodowały wzrost ilości RFT od 119 do 125%. Dodatkowo zdecydowano się wykonać obrazowanie przyżyciowe sferoidów linii U-251, które wykazało zwiększenie intensywności fluorescencji świadczące o wysokim stężeniu RFT będącym efektem działania chelatorów TSC, szczególnie w przypadku traktowania MS168, gdzie zanotowano najsilniejszy sygnał spośród wszystkich badanych związków. Wyniki obrazowania były zgodne z pomiarami ilościowymi i wskazują one na zdolność analizowanych chelatorów do zaburzania homeostazy redoks w komórkach GBM.

Obydwie serie eksperymentów pokazały zdolność badanych chelatorów do generowania stresu oksydacyjnego w komórkach GBM w wyniku zaburzenia homeostazy żelaza. Zwiększone stężenie RFT w komórce prowadzi do zaburzenia wielu procesów zachodzących w komórce, czego efekty następnie zweryfikowano poprzez analizę ekspresji genów oraz białek biorących udział w regulacji ich przebiegu.

2.5. Wpływ wybranych związków na ekspresję genów i białek (PCR, WB)

Wyniki przedstawione w poprzednich sekcjach pokazują, że wyselekcjonowane chelatory istotnie oddziałują na różne aspekty funkcjonowania komórek GBM. Pełne poznanie molekularnego mechanizmu ich działania wymaga jednak dokładniejszej analizy zmian zachodzących w komórkach. Dlatego ostatnim etapem badań było wybranie genów oraz białek biorących udział w przebiegu procesów metabolicznych zaburzanych przez badane związki, a następnie wykonanie analiz zmiany ich ekspresji przy użyciu technik qRT-PCR oraz Western Blot.

W publikacji [P1] najpierw podjęto się analizy ekspresji czterech genów należących do systemu obrony antyoksydacyjnej – dysmutazy ponadtlenkowej 1 i 2 (*SOD1* i *SOD2*), i katalazy (*CAT*), których funkcją jest neutralizacja anionów ponadtlenkowych i nadtlenku wodoru w celu zabezpieczenia struktur komórkowych przed uszkodzeniem, oraz tioredoksyny 2 (*TXN2*), będącej białkiem zdolnym do redukcji aminokwasów innych białek utlenionych w wyniku działania RFT. Zaobserwowano, że w wyniku traktowania związkiem BC2 następuje gwałtowny spadek ekspresji wszystkich wymienionych genów z wyjątkiem *SOD2*, który zwiększył ekspresję o około 250%. Sugeruje to, że działanie tego chelatora szczególnie silnie wpływa na działanie systemu opartego na działaniu tioredoksyn, którego pula dostępna w komórce zużywa się w wyniku kontaktu ze zwiększoną ilością RFT. System obrony antyoksydacyjnej został przeciążony w wyniku aktywności związku BC2, natomiast próbą odpowiedzi komórki na wzmożone działanie stresu oksydacyjnego jest nadekspresja *SOD2*, która ostatecznie nie jest w stanie go przezwyciężyć. Znaczące spadki ekspresji wykryto również dla genów *PIK3CA* i *MAPK1* odpowiadających za stymulację proliferacji oraz procesów wspierających przeżycie komórki, a także dla genu *mTOR* będącego regulatorem licznych procesów metabolicznych. Wyciszanie ścieżek sygnałowych związanych z tymi genami dobrze rokuje w kontekście potencjalnie skutecznej metody leczenia nowotworów. Dodatkową zaletą zmniejszenia ekspresji *mTOR* jest możliwość indukcji procesu autofagii komórki, którego zainicjowanie potwierdza nadekspresja genu *LC3*, jednego z ważniejszych markerów tego procesu. Rezultaty analizy ekspresji wszystkich opisanych powyżej genów są obiecujące i potwierdzają wcześniej zaobserwowane zmiany wywołane przez związek BC2.

Wyniki analizy ekspresji białek przeprowadzonej w publikacji [P1] potwierdziły przypuszczenia wynikające z wcześniejszych eksperymentów. Zaobserwowane

zatrzymanie cyklu w fazie G0/G1 znajduje odzwierciedlenie w niemal całkowitym zaniku ekspresji białek regulujących progresję cyklu komórkowego dla najwyższych stężeń związku BC2 – cdc25c, cdc2 oraz cyklin A2 i B1. Dalsze poszlaki wskazujące na załamanie systemu obrony antyoksydacyjnej to zanik ekspresji białka Nrf2, będącego jego głównym regulatorem. W efekcie braku skuteczności mechanizmów usuwających RFT z komórki wzrasta również ekspresja białek HO-1 oraz HIF-1α ukazująca reakcję na wysoki stres oksydacyjny. Zauważalny jest również wpływ badanych związków na metabolizm żelaza w postaci spadku ekspresji mitoferryny 1 i ferrochelatazy (FECH), czyli białek biorących udział w transporcie żelaza i biosyntezie hemu, a także stopniowego zaniku ekspresji białka IDH1 odpowiadającego za syntezę NADPH potrzebnego do prawidłowego funkcjonowania systemów obrony antyoksydacyjnej. W rezultacie długotrwałego działania wysokiego poziomu RFT, zaobserwowano również zablokowanie fosforylacji białka Akt oraz pojawienie się produktów cięcia kinazy p70 S6, które skutkowało inhibicją szlaku sygnałowego odpowiedzialnego za proliferację oraz inicjacją procesu apoptozy zależnego od kaspaz. Rozpoczęcie procesu programowanej śmierci komórki ostatecznie potwierdził wzrost ekspresji proapoptotycznego białka BID. Wyniki przedstawione w publikacji [P2] sugerują, że pomimo pewnych podobieństw, chelatory będące pochodnymi TSC oddziałują na komórki GBM w odmienny sposób. Nadekspresja HO-1 miała miejsce również dla tej grupy związków, lecz wzrost ekspresji tego białka był znacząco większy, sugerując wystąpienie silnego stresu oksydacyjnego. Spadki ekspresji białek regulujących mechanizmy obronne przed peroksydacją lipidów, GPX4 oraz 4F2hc, może wskazywać na zwiększone ryzyko utleniania cząsteczek lipidów budujących błony komórkowe przez RFT. Wzrost ekspresji HO-1 może również pośrednio wynikać z deficytu żelaza w komórce spowodowanego chelatacją przez badane TSC, na co wskazuje zwiększona zawartość białek IRP1 i IRP2, zazwyczaj aktywowanych w warunkach niedoboru jonów tego metalu. Kolejnym dowodem na istotne zaburzenie homeostazy żelaza jest spadek ekspresji FECH oraz frataksyny (FXN), czego efektem są zaburzenia biosyntezy hemu oraz centrów żelazowo-siarkowych mogące rzutować na poprawne funkcjonowanie mitochondriów. Oddziaływanie badanych TSC na receptorową kinazę IGF1R, do której powinowactwo wykazywała część z nich, można zauważyć w spadku poziomu białka Akt. Stanowi ono główny element jednego ze szlaków sygnałowych regulowanych przez IGF1R, co stanowi poszlakę w kwestii znaczenia inhibicji tej kinazy w terapii przeciwko komórkom GBM.

3. PODSUMOWANIE I WNIOSKI

W niniejszej pracy podjęto się identyfikacji molekularnego mechanizmu działania pięciu spośród ponad 30 chelatorów żelaza należących do trzech grup: kompleksów bis(terpirydyny), pochodnych tiosemikarbazonu oraz pochodnych styrylochinoliny. Zastosowanym kryterium selekcji była wielkość efektu cytotoksycznego wywoływanego podczas traktowania komórek pięciu linii glejaka wielopostaciowego przy jednoczesnym braku cytotoksyczności wobec komórek prawidłowych, które spełnił jeden kompleks bis(terpirydyny) – BC2 oraz cztery pochodne tiosemikarbazonu – MS165, MS168, MS179 oraz MR5K3.

Podstawowy mechanizm działania badanych związków oparty jest na zdolności do chelatowania jonów żelaza, w wyniku której biodostępna pula tego metalu w komórce ulega zmniejszeniu, wpływając na funkcjonowanie białek zależnych od żelaza. Obserwowany spadek ekspresji FECH wskazuje na zaburzenie mitochondrialnego metabolizmu żelaza oraz procesu syntezy hemu. Mechanizm działania chelatorów w mitochondriach różnił się: w przypadku związku BC2 odnotowano zanik mitoferryny 1 wskazujący na zaburzenie transportu jonów żelaza, natomiast w przypadku pochodnych TSC nadekspresja IRP1 i IRP2 sugeruje większe znaczenie sekwestracji żelaza przez te związki. Kolejną konsekwencją procesu chelatacji jest zwiększenie poziomu RFT, które prowadzi do powstania stresu oksydacyjnego inicjującego systemy obrony przed rodnikami tlenowymi. Intensywny wzrost ekspresji białka HIF-1α w wyniku traktowania związkiem BC2 oraz białka HO-1 dla wszystkich analizowanych pochodnych, przy jednoczesnym spadku ekspresji białek pełniących funkcje ochronne (Nrf2 w przypadku BC2, GPX4 oraz 4F2hc w niektórych TSC) sugeruje, że pomimo próby reakcji komórek linii U-251 na stres oksydacyjny, system obrony antyoksydacyjnej został przeciążony. Dla obydwu rodzajów chelatorów obserwowano również oddziaływanie na ścieżki sygnałowe, szczególnie w przypadku pochodnych TSC oraz zbliżonych do nich strukturalnie styrylochinolin. Dla tych dwóch grup związków widoczny był szeroki zakres interakcji z kinazą receptorową IGF1R, potwierdzony za pomocą testów interakcji ligand-białko oraz dokowania molekularnego. Funkcją IGF1R jest odbieranie oraz przekazywanie sygnałów zewnątrzkomórkowych poprzez ścieżki sygnałowe, które w wyniku traktowania badanymi związkami ulegały zmianom ekspresji. W przypadku związku BC2 wykryto zaburzenie fosforylacji białka Akt, natomiast pochodne TSC

powodowały spadek ekspresji samego białka, co pośrednio może wskazywać na efekt inhibicji IGF1R. Obydwie grupy związków wpływały ostatecznie na indukcję apoptozy poprzez generowanie wzmożonego stresu oksydacyjnego. Związek BC2, poprzez oddziaływanie na białko BID oraz cięcie p70 S6 może prowadzić do aktywowania kaspaz i związanego z nimi mitochondrialnego szlaku apoptozy. W przypadku traktowania pochodnymi TSC istnieją przesłanki wskazujące na możliwość występowania ferroptozy, rodzaju śmierci komórkowej wywoływanego przez nadmierną akumulację żelaza i wynikającą z niego peroksydację lipidów.

Wyniki przedstawione w niniejszej pracy pokazują, że chelatory żelaza są związkami zdolnymi do wielokierunkowego oddziaływania na komórki glejaka wielopostaciowego, dzięki czemu mogą stanowić podstawę wciąż intensywnie poszukiwanej, skutecznej terapii przeciwko temu rodzajowi nowotworów.

4. PUBLIKACJE WCHODZĄCE W SKŁAD PRACY

4.1. [P1]. Imbalance of redox homeostasis and altered cellular signaling induced by the metal complexes of terpyridine

Autorzy: Malarz K., Zioła P., Zych D., Rurka P., Mrozek-Wilczkiewicz A.

Referencja: *Scientific Reports*, 2024, **14**, 26951

Numer DOI: 10.1038/s41598-024-77575-4

Impact Factor czasopisma: 3.9 (2024)

Liczba punktów MNiSW czasopisma: 140 (2024)

Mój udział w pracy polegał na wykonaniu badań: cytotoksyczności z dodatkiem jonów metali, indukcji apoptozy oraz zmiany ekspresji białek.

scientific reports

Check for updates

OPEN

Imbalance of redox homeostasis and altered cellular signaling induced by the metal complexes of terpyridine

Katarzyna Malarz[1,2], Patryk Ziola[2], Dawid Zych[3], Patryk Rurka[2] & Anna Mrozek-Wilczkiewicz[1,2]✉

Compounds that can induce oxidative stress in cancer cells while remaining nontoxic to healthy cells are extremely promising for potential anticancer drugs. 2,2′:6′,2′′-terpyridine-metal complexes possess these properties. The high level of activity (IC_{50} = 0.605 μM) of 2,2′:6′,2′′-terpyridine-metal complexes on lung, breast, pancreatic, and glioblastoma multiforme cancer lines and their selectivity (SI > 41.32) on human normal fibroblasts were confirmed and presented in this paper. The mechanism of action of these compounds is associated with the generation of reactive oxygen species, which affects several cellular pathways and signals. The results demonstrate that 2,2′:6′,2′′-terpyridine-metal complexes affect cell cycle inhibition in the G0/G1 phase as well as the activation of apoptosis and autophagy cell death. These results were confirmed in several independent studies, including experiments measuring the fluorescence levels of reactive oxygen species, flow cytometry, and gene and protein analysis.

Keywords 2,2′:6′,2′′-terpyridine, Anticancer activity, Reactive oxygen species, Oxidative stress, Apoptosis, Autophagy, Cell cycle inhibition

According to a Lancet Oncology study and others, a correlation was found between the human development index (HDI) and the occurrence of higher rates of lung, pancreatic, and breast cancers[1,2]. HDI is a combined index of a country's level of human development, which is based on factors such as life expectancy, education, and income. That being said, studies have shown that there is a significant correlation between HDI, cancer incidence, cancer type, and mortality rates. In recent years, breast cancer has been the most frequently diagnosed cancer worldwide, overtaking lung cancer. In particular, this type of cancer is a common problem among women living in developing countries and causes 11.7 million new cases annually. Lung cancer, on the other hand, has the highest mortality rate, which is steadily rising. The percentage of lung cancer deaths without gender distribution is about 18% of all cancer deaths[3]. The aforementioned types of cancer, as well as colorectum and prostate cancers, accounted for 50% of all diagnosed cancer types. Glioblastoma (GBM), on the other hand, is not as common, but its course is often rapid and does not have a good prognosis. Statistical data show that 75% of GBM patients die within two years of diagnosis after undergoing intensive treatment regimens, and only about 5% survive five years. The median overall survival (mOS) for GBM patients remains at approximately 10.2 months[4,5]. Another very aggressive tumor type is pancreatic cancer, which owes its poor prognosis largely to a late diagnosis when an appropriate treatment regimen and resection cannot be implemented, as well as its high asymptomatic rates in the early stages[6]. Therefore, we chose to explore those four types of cancer, which are prevalent in Western societies, and which are on the rise in Asia.

Metal complexes are known for their use in anticancer therapy[7,8]. Most famously, cisplatin is one of the most commonly used drugs in the treatment of ovarian, testicular, bladder, and lung cancer patients[9,10]. In addition, cisplatin serves as a popular source of the derivatives that are used in treatment, such as carboplatin, which is used during ovarian cancer treatment[11,12], or oxaliplatin, which is used as a drug for metastatic colon cancer patients[13,14]. Currently, there are no anticancer drugs with a terpyridine core as a ligand, thus this privileged structure is particularly interesting from the point of view of basic research, especially because there

[1]Department of Systems Biology and Engineering, Silesian University of Technology, Akademicka 2A, Gliwice 44-100, Poland. [2]A. Chełkowski Institute of Physics, University of Silesia in Katowice, 75 Pułku Piechoty 1a, Chorzów 41- 500, Poland. [3]Faculty of Chemistry, University of Opole, Oleska 48, Opole 45-052, Poland. ✉email: anna.mrozek-wilczkiewicz@us.edu.pl; wilczkiewicz@polsl.pl

are numerous literature reports on the biological activity of these compounds in the context of anticancer[13,16], antibacterial[17], or antifungal activity[18] and also including different uses as photovoltaic[19] or optoelectronic[20] materials or in fluorescence cellular imaging[21]. However, in light of our long-standing research on the terpyridine derivatives, in this work, we focus on their anticancer properties. This paper explores the anticancer activity of the newly synthesized bis(terpyridine) complexes with metal ions. Based on our previous studies, we chose the ligand 2,2':6',2''-terpyridine that, unlike 2,2':6',3''-terpyridine or 2,2':6',4''-terpyridine, has an arrangement of N atoms that guarantees the best chelating properties and thus the best activity[22]. In the current work, we combined the aforementioned ligand with various metal ions to see how their redox activity affects the anticancer activity of the whole complex. Numerous preliminary studies were concerned with the basic cytotoxicity of terpyridine derivatives and tested on selected cancer cell lines[23]. One can also find slightly more advanced studies investigating cell cycle inhibition[24] or triggering apoptosis[25]. Much attention is being paid to the ability of these derivatives to intercalate with DNA[26–28]. However, due to the small number of studies that describe the detailed mechanism of the anticancer action of these compounds, including the key pathways that are responsible for the proliferation, signaling, and triggering of the cell death process, in our study, we focused on the most important cellular targets that are associated with the described phenomena. The resultant cytotoxic effect could be the result of many factors that occur at both the gene level and one step further – at the protein level. Therefore, we decided to do an extended study to verify the cytotoxic effect, taking into account these factors. In addition to conducting preliminary studies on several selected cell lines, we determined the effect of the tested compounds on the cell cycle and investigated which mechanism triggered cell death. Next, we investigated whether the tested derivatives generated reactive oxygen species (ROS), which occurred in our previous studies, conducted using terpyridine analogs in the form of complexes and a free ligand[28,30].

Cancer cells are known to have elevated ROS levels, thus making them vulnerable to an additional increase in ROS concentration[31]. Therefore, the use of ROS-generating compounds could be an interesting anticancer strategy[32]. The oxidative stress that persists in cancer cells is caused by both high levels of ROS itself and a reduction in the ROS-scavenging capacity[33]. In other words, the balance is shifted towards increased production of radicals and hydrogen peroxide (H_2O_2), which causes damage to the DNA, cellular proteins, and lipids, which consequently causes cell death. Complex antioxidant systems are responsible for maintaining an adequate level of ROS homeostasis. Among them, the most important antioxidant enzymes are superoxide dismutase (SOD), catalase (CAT), glutathione (GSH), and the glutathione-dependent enzymes (glutathione peroxidases, glutathione reductases, and glutathione S-transferases) as well as thioredoxin (TXN2) and thioredoxin reductase (TXN2R)[34]. Generally, we can divide intracellular antioxidants into first-line defensive systems (SOD, CAT, and glutathione peroxidases) that inactivate the strongest radicals such as superoxide ($O_2^{\cdot-}$) or H_2O_2 and second-line defensive systems (GSH and TXN2), whose purpose is to be an electron donor to the paired radical to inhibit a radical reaction[35]. It can be said that the GSH antioxidant pathways and TXN2 are the key gatekeepers for maintaining the proper redox balance[36]. When discussing the cellular antioxidant enzymes, it is impossible not to mention heme oxygenase-1 (HO-1), which is involved in the degradation of heme into carbon monoxide, biliverdin, bilirubin, and iron[37]. Determining the level of this protein is an important indicator of the occurrence of oxidative stress after cells have been treated with a substance with potential drug applications. A complex system that is designed to control radical reactions oversees the maintenance of the proper redox homeostasis. Therefore, it is no surprise that a disruption of this normal balance towards elevated ROS concentrations affects all of the key pathways in a cell.

Results and discussion

Chemistry

The terpyridine ligand (5) was synthesized following a previously published protocol (Scheme 1) using 4-bromobenzaldehyde and 2-acetylpyridine, which are available commercially, in a Kröhnke reaction to produce 4'-(4-bromophenyl)-2,2':6',2''-terpyridine (1). Subsequently, 4'-(4-bromophenyl)-2,2':6',2''-terpyridine (1) underwent Sonogashira coupling with trimethylsilylacetylene to yield 4'-(4-ethynylphenyl)-2,2':6',2''-terpyridine (2). The obtained 4'-(4-ethynylphenyl)-2,2':6',2''-terpyridine (2) was then used in another Sonogashira coupling reaction, this time with 9-octyl-3-iodocarbazole, which was prepared from commercially available carbazole through a process involving iodination (3) and alkylation (4)[38,39]. The synthesized terpyridine ligand (5) was subsequently used in complexation reactions with inorganic salts of various metals, namely Zn^{2+}, Y^{3+}, Hg^{2+}, Cd^{2+}, Cu^{2+}, and Fe^{3+}. These reactions led to the formation of bis(terpyridine) complexes, which were labeled as **BC1**, **BC2**, **BC3**, **BC4**, **BC5**, and **BC6**, respectively.

The spectroscopic data (^1H and ^{13}C NMR) of molecules 1–5 were in agreement with our previously published results[20,35,39]. The structures of **BC1-BC6** were confirmed using mass spectrometry and are presented in the Supporting Information (Fig. S1-S8). The ^1H NMR spectra, which were recorded in deuterium chloroform, exhibited no attribution of peaks due to the para- and ferromagnetic nature of the complexes. Additionally, we added photos of the light emission that were used in the solutions of the complexes under study and the reference ligand (Fig. S9).

Anticancer studies

The analysis of the effects of the tested complexes **BC1-BC6** on inhibiting the proliferation of the selected cell lines that currently represent the most dangerous and common types of cancer is presented below. The results, which are expressed in terms of the IC_{50} parameter, are summarized in Table 1. The reference compound for the cytotoxicity assay was the drug osimertinib (OSI), a well-known tyrosine kinase inhibitor that is used to treat GBM. Of all the complexes evaluated, the lowest IC_{50} value (highest activity) was recorded for the **BC5** derivative with Cu^{2+} at 0.358 µM for the PC-9 (lung cancer) cell line. This compound exhibited the highest activity on all of the tested lines, where the IC_{50} was below 2 µM for the four tested cell lines (PC-9, U-251 (GBM), MCF-7

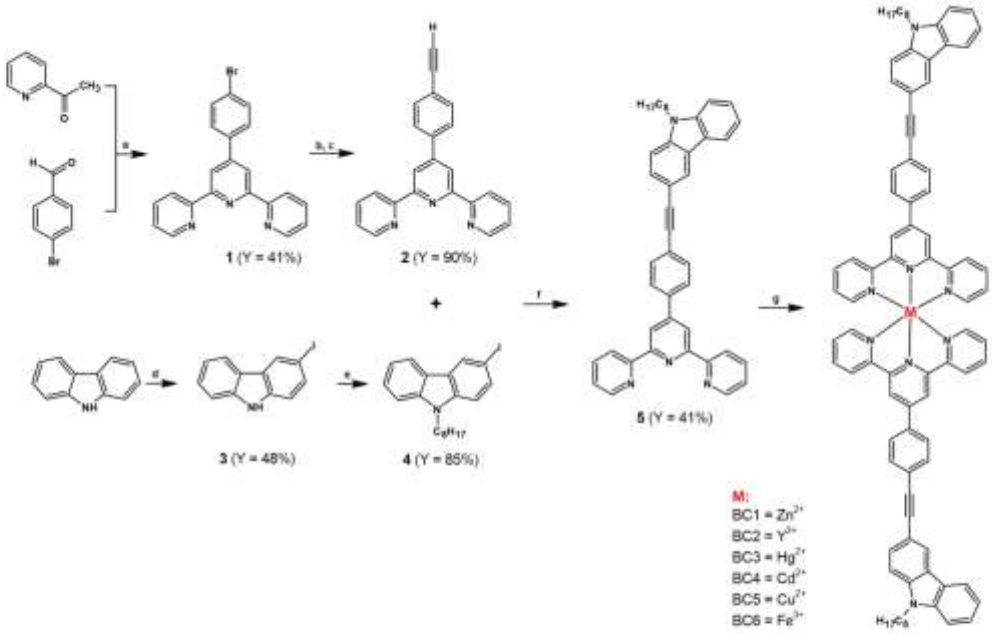

Scheme 1. Synthesis of the bis(terpyridine) complexes. Reagents and reaction conditions: (a) KOH, NH_{3aq}, EtOH, room temp., 24 h; (b) TMSA, $[Pd(PPh_3)_4]$, CuI, NEt_3, reflux, 16 h; (c) KF, THF, MeOH, room temp., 24 h; (d) KI, KIO_3, CH_3COOH, reflux, 0.5 h; (e) $C_8H_{17}Br$, TBAI, $NaOH_{aq}$, DMSO, room temp., 12 h; (f) $[Pd(PPh_3)_4]$, CuI, THF/NEt_3 (1:1), 78 °C for 48 h; (g) metal precursors: $CuCl_2$, $FeCl_3$, $Cd(NO_3)_2$, $HgCl_2$, YCl_3, $ZnCl_2$, ACN, DCM, 90 °C, 2 h.

Compound	activity - IC_{50} value [μM]					
	MCF-7	U-251	U-87 MG	PANC-1	PC-9	NHDF
BC1	21.62 ± 5.82	>25	18.22 ± 2.43	>25	9.09 ± 0.56	>25
BC2	2.92 ± 0.49	1.69 ± 0.14	1.57 ± 0.18	2.41 ± 0.51	0.61 ± 0.07	>25
BC3	4.95 ± 1.32	2.79 ± 0.64	2.35 ± 0.27	3.47 ± 0.65	0.84 ± 0.05	>25
BC4	2.52 ± 0.48	2.16 ± 0.12	3.27 ± 0.59	3.55 ± 0.63	0.74 ± 0.19	>25
BC5	1.33 ± 0.34	1.15 ± 0.06	2.16 ± 0.24	1.65 ± 0.18	0.36 ± 0.10	6.27 ± 1.03
BC6	18.52 ± 2.42	>25	>25	>25	>25	>25
Osimertinib (OSI)	8.34 ± 0.71	20.13 ± 0.34	11.24 ± 0.46	7.14 ± 0.71	1.44 ± 0.33	6.27 ± 0.38

Table 1. The antiproliferative activity of the tested bis(terpyridine) complexes on a panel of cancer cell lines and normal fibroblasts. Colour map legend: red – $IC_{50} < 2$ μM; yellow – $IC_{50} = 2$ μM-6.5 μM; grey – $IC_{50} > 6.5$ μM.

(breast cancer), PANC-1 (pancreatic cancer)) and slightly above 2 µM for U-87 MG (GBM). However, **BC5** also exhibited toxicity towards normal human dermal fibroblasts (NHDF). Therefore, **BC5** was eliminated in the context of a broader analysis of the mechanism of action. For this study, the second-ranked compound, **BC2** with Y^{3+}, was selected. Low IC_{50} values were also registered for this compound; the lowest equaled 0.605 µM for PC-9 cells and was below 2 µM for two cell lines (U-87 MG and U-251) and slightly above 2 µM for the other two cell lines (PANC-1 and MCF-7). However, for **BC2**, no toxicity to healthy cells was recorded. Therefore, this complex was subjected to a further in-depth analysis.

In Table S1, the selectivity indexes (SIs) of all of the tested complexes were collected. The SIs were calculated by dividing the IC_{50} values for normal cells by the IC_{50} that was calculated for the cancer cells. This parameter enabled the safety of the tested derivative to be estimated. The SI (calculated for the PC-9 line, for which **BC2** exhibited the highest activity) was more than 41.32, which indicates a good prognosis in the context of the later toxicity studies of this compound. The therapeutic indexes (co-factor the same as the SI but deducted based on clinical studies) of the currently used cytostatic do not exceed a value of 0.3. For example, the SI for OSI for all of the tested cell lines was in the range of 0.31–0.88 for U-251, U-87 MG, MCF-7, and PANC-1 cells and was 4.34 for PC-9 cells. For **BC2**, the SIs were the highest of all the complexes evaluated and were in the range of > 8.58–>15.97 for MCF-7, PANC-1, U-251, and U-87 MG, with the highest SI being previously mentioned for PC-9. The **BC3** and **BC4** derivatives containing Hg^{2+} and Cd^{2+} ions, respectively, exhibited a similar activity, i.e., their IC_{50}s for PC-9 equaled 0.839 µM and 0.741 µM, respectively, and were in the range of 2.161–4.947 µM for the rest of the cancer cell lines. All of the **BC2**–**BC5** derivatives exhibited higher activity against the tested cancer cell lines than the reference compound (OSI) and had higher SI values. This result is promising for further research as the tested derivatives are selective against healthy cells. The greatest sensitivity to the tested derivatives was exhibited by the PC-9 line. The second most sensitive were U-251 cells. Therefore, these lines were selected for more detailed studies on the mechanism of action of the bis(terpyridine) complexes.

Interestingly, the **BC1** and **BC6** derivatives with Zn^{2+} and Fe^{3+} ions, respectively, exhibited no significant activity against the cell lines being evaluated. These results show how important the influence of the central metal ion is on the activity of the whole complex. A number of our previous works[29,30] and those of other teams[40,41] confirmed the effect of ROS generation on the biological activity of the bis(terpyridine) complexes. The behavior of the radical reactions is associated with the involvement of the ligand coordination sphere in electron transfer. Therefore, it is influenced by the type of central ion of the complex that is formed. To confirm this theory, we experimented by adding Cu^{2+}, Fe^{2+}, Fe^{3+}, and Zn^{2+} ions to evaluate their effect on cell survival. As shown in Fig. S10, in most cases, the addition of the ions either did not change cell survival or caused it to increase. The highest increase in cell survival, in other words, the deterioration of antiproliferative properties was observed in the case of the PC-9 cell line, for which as much as a three-fold increase in cell survival was observed. These data indicate a key contribution of the central ion to the redox activity of the entire complex. To verify this theory, we conducted an experiment in which we measured the level of ROS in cells that had been incubated with the tested compounds.

Cell cycle assay

The antiproliferative effects of the tested 2,2′:6′,2″-terpyridine derivatives on cells derived from different types of tumors were analyzed to select the most interesting compound that exhibited cytotoxicity towards cancer cells, while not harming healthy cells. A **BC2** derivative with Y^{3+} as a central ion was selected for further analysis of the mechanism of action. First, flow cytometry was used to verify at which phase the cell cycle was blocked. For this purpose, the fluorescent dye propidium iodide was used to determine the amount of DNA. Different phases of the cell cycle differ in DNA content. Therefore, this method makes it easy to determine at which phase the cell cycle is inhibited. Graphs showing the percentage of cells in each phase of the cell cycle after the incubation of PC-9 and U-251 cell lines with the **BC2** derivative are presented in Fig. 1. The negative reference was untreated control cells with a positive control OSI. Detailed histograms with the percentages are presented in Fig. S11 (PC-9) and Fig. S12 (U-251).

For both of the evaluated cell lines, a clear increase in cells in the G0/G1 phase was observed at all of the **BC-2** concentrations that were evaluated, with the effect being more pronounced for the PC-9 line, which showed a greater sensitivity to the tested derivative. These results are consistent with our previous studies of terpyridine derivatives[29,30] and were also confirmed by western blot experiments at the protein level.

Annexin V binding assay

Flow cytometry was used to study the type of cell death that is induced by the tested compound. Annexin V staining is a simple method for measuring apoptotic cells. One of the hallmarks of apoptosis is the shuffling of the phosphatidylserine outward from the cell membrane after it has lost its integrity. The fluorescent conjugate of annexin V has a high affinity for this anionic phospholipid. The emitted green signal, which is the apoptosis indicator, enables the number of cells in which apoptosis has been triggered to be quantified. Figure 2 shows the percentage of cell subpopulations (live, late and early apoptotic, and dead) after **BC2** derivative incubation at different concentrations compared to the untreated control cells and the positive control (OSI). Detailed histograms with percentages are presented in Fig. S13 (PC-9) and Fig. S14 (U-251).

The above graphs clearly show the presence of apoptotic fractions in both of the tested cell lines. The fraction of living cells decreased significantly after incubation with the tested compound **BC2**. The obtained results prove that the tested terpyridine complex triggered the process of apoptosis in the cells, which is consistent with the previously obtained results of both our group[29,30] and many others[23,28].

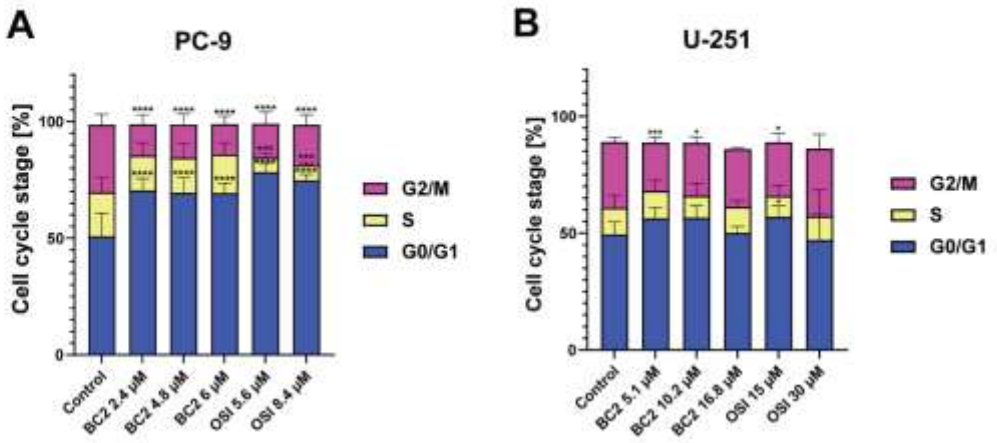

Fig. 1. The influence on the progression of the cell cycle in the PC-9 (A) and U-251 (B) cell lines by **BC2** and OSI. The results that are shown in the form of a bar graph consist of the mean ± standard deviation (SD) of at least four independent measurements. Statistical significance was evaluated using a one-way ANOVA ($^{*}p < 0.05$, $^{**}p < 0.01$, $^{***}p < 0.001$, $^{****}p < 0.0001$ compared to the control).

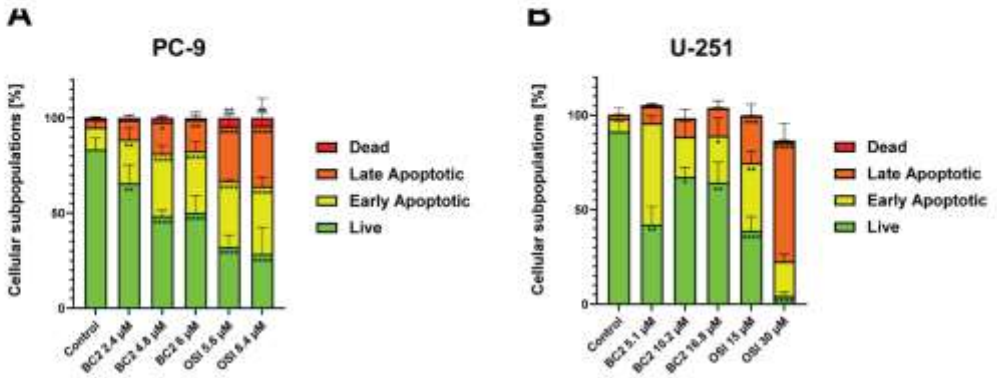

Fig. 2. The effect of **BC2** and OSI on apoptosis induction in the PC-9 (A) and U-251 (B) cell lines. The results that are shown in the form of a bar graph consist of the mean ± SD of at least four independent measurements. Statistical significance was evaluated using a one-way ANOVA ($^{*}p < 0.05$, $^{**}p < 0.01$, $^{***}p < 0.001$, $^{****}p < 0.0001$ compared to the control).

Reactive oxygen species generation

The intracellular reactive oxygen species levels after treatment (3–24 h) with the tested compounds were evaluated by fluorescence measurements using the CellROX dye. As shown in Fig. 3, the highest increase in the ROS level was observed in both cell lines after 24 h of incubation. In addition, our analysis indicated that the ROS level increased with the time-dependent incubation of **BC2** at 5.1 and 10.2 μM in the U-251 cells. In turn, some fluctuations in the concentration of ROS in the PC-9 cells were observed during the treatment with **BC2** and OSI. These observations might be related to the different susceptibility and response of the tested cell lines to the destabilization of redox homeostasis. Additional cytotoxicity experiments with ascorbic acid confirmed our assumptions. Namely, the antiproliferative activity of **BC2** against U-251 and PC-9 cells was levelled when ascorbic acid was added at a concentration of 100 μM (Fig. S15).

As was mentioned above, cancer cells maintain higher levels of ROS than normal cells[33]. Consequently, their antioxidant defense system is also modified and downregulated through a network of gene and protein interactions to maintain specific levels of cellular ROS. Although cancer cells are adapted to elevated ROS levels,

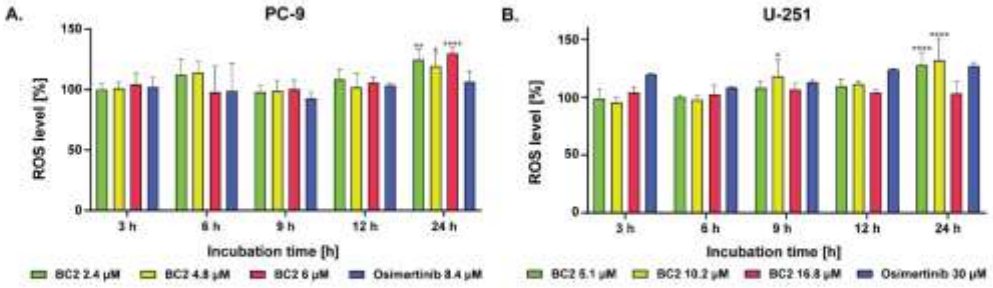

Fig. 3. ROS levels after a 3–24 h kinetic incubation with **BC2** and OSI on PC-9 (A) and U-251 (B) cells. The results are shown as the mean ± SD from at least three independent measurements. Statistical significance was evaluated using a one-way ANOVA (*$p < 0.05$, **$p < 0.01$, ***$p < 0.001$, ****$p < 0.0001$ compared to the control).

even a slight ongoing stimulation of ROS production can trigger the desired therapeutic effects by depleting the antioxidant defense resources. The breakdown of antioxidant defenses begins the process that leads to the destruction of cells[42]. Usually, mitochondria play the central role, where the first signs of induced cell death are the loss of the permeability of the inner mitochondrial membrane and control of the mitochondrial permeability transition pore complex, disruption of the membrane potential, and release of cytochrome c as well as the activation of the caspase-dependent pathway[43]. In the context of the therapeutic approach, ROS can be considered to be a double-edged sword[13,44]. On the one hand, the cancer cells achieve a state in which unbalanced levels of ROS promote enhanced metabolism, uncontrolled cell growth, and tumor progression. On the other hand, an excessively elevated ROS concentration can ultimately induce the effects of oxidative stress, which focuses on the activation of programmed cell death[42]. Thus, ROS-based therapy, which modulates the redox balance in cells, can be effective and selective for cancer cells and also has a low toxicity to normal cells[44].

Analysis of gene expression

To elucidate the mechanism of action of the **BC2** bis(terpyridine) complex in the GBM and lung cancer cells in more detail, studies at the transcript level were performed. The selected genes were associated with the elements of the antioxidant defense system, such as *SOD1*, *SOD2*, *CAT*, and *TXN2*, as well as the genes associated with the oxidative stress activation, survival, and autophagy induction pathways, such as *MAPK1*, *PIK3CA*, *mTOR*, and *LC3*. The alterations in gene expression were determined in the PC-9 and U-251 cells after exposure to **BC2** at two different concentrations (6 and 10.2 μM), which caused the highest increase in the ROS levels that had been observed in the previous experiment (Fig. 3). The positive control was OSI, which can generate ROS, which are critical for triggering autophagy and apoptosis death in non-small cell lung cancer (NSCLC) cells[45].

The subsequent analyses revealed several changes in the expression of the key elements of a cell's antioxidant system, which is activated to nullify ROS after their exposure to the tested compound. The results are presented in Fig. 4. A significant, approximately two-fold increase in the *SOD1* and *SOD2* expression was registered in the PC-9 cells after exposure to **BC2**. The *SOD1* gene encodes the Cu/Zn superoxide dismutase, which is responsible for regulating the O_2^- levels in the mitochondrial intermembrane space, cytoplasmatic area, and peroxisomes. In turn, the activation of *SOD2* protects cells from mitochondrial-derived ROS[46]. Moreover, the *TXN2* gene expression increased more than three-fold after the **BC2** treatment compared to the control cells. More than a three-fold reduction in the expression level of the catalase (*CAT*) gene was registered after incubation with **BC2**. A similar decrease in the amount of *CAT* mRNA was registered in the U-251 cells. The decrease in the *CAT* expression, which is categorized as a so-called second line of defense against ROS, might be the result of the depletion of the available pool of the catalase protein as a result of the ROS scavenging, which would then be renewed at another time point. Indeed, it should be noted that radical reactions occur much faster than the cellular processes. In the case of GBM cells, this downtrend was also registered for the *SOD1* and *TXN2* genes.

Namely, **BC2** caused a significant, more than two-fold downregulation in the *SOD1* expression and a more than a 14-fold reduction in the *TXN2* mRNA levels. We suppose that the thioredoxin-based defense system might be particularly vulnerable to the terpyridine derivatives. Our assumption may be supported by the results for 2,2′:6′,2″-terpyridine platinum (II) complexes, which had a high affinity and decreased the thioredoxin reductase activity in GBM cells[47]. Moreover, others determined that the anticancer effects of these terpyridine complexes on a rat model of GBM might be based precisely on the inhibition of TXN2R and intercalation into DNA, thereby resulting in cell cycle arrest[48]. Meanwhile, an almost 2.5-fold increase in the *SOD2* levels was also observed. The different behavior of **BC2** in the PC-9 and U-251 cells could be related to the significantly lower antioxidant capacity in brain cancer than in other tissue areas[49]. In contrast, OSI increased the expression of almost all of the antioxidative defense genes in the tested cell lines except for *SOD2* in the U-251 cells (no change in the level of its expression). The variations in the response to the terpyridine derivative between the cell lines might offer insight into the diversity of the regulation mechanisms and behavior of the cell defense system. In addition, a more in-depth elucidation of the effect of metal complexes on the pathways that induce oxidative stress could expand the existing knowledge and improve the potential for precise treatment.

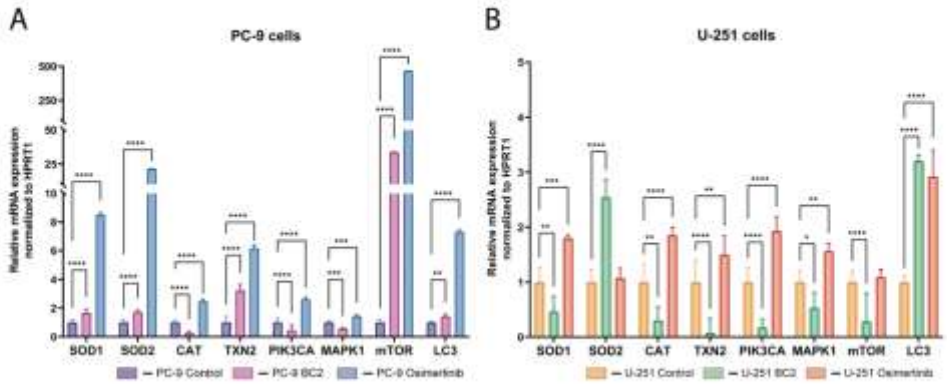

Fig. 4. mRNA expression of the selected genes after a 24 h incubation with **BC2** and OSI for the PC-9 (A) and U-251 (B) cell lines. Results are shown as the mean and ± SD from at least three independent measurements. Statistical significance was evaluated using a two-way ANOVA (*$p < 0.05$, **$p < 0.01$, ***$p < 0.001$, ****$p < 0.0001$ compared to the control).

In the *PIK3CA* and *MAPK1* gene levels, we observed similar correlations between the tested cell lines after exposure to the terpyridine derivative and OSI. Namely, **BC2** caused a significant decrease in *PIK3CA* expression, more than a two-fold and five-fold decrease for PC-9 and U-251 cells, respectively. Both cell lines also registered a nearly two-fold reduction in the *MAPK1* levels. Considering the role of the PI3K and MAPK proteins in stimulating cellular proliferation and triggering pro-survival processes[50], the results observed at the transcript level are promising. Particularly in the context of OSI, which induced the opposite effect – the expression decreased approximately 1.5-fold for both of the tested genes. Our previous data indicated that 4′-phenyl-2,2′:6′,2″-terpyridine might activate a dual mode of cell death through apoptosis and autophagy[30]. Moreover, autophagy and the enhanced ability to form autophagosomes have been found for platinum, copper, and gold terpyridine complexes[51,52]. With this in mind, the levels of the two genes that are associated with the activation of autophagy and cell survival processes were determined. As shown in Fig. 4, an increased level of the *LC3* gene was observed in both of the tested cell lines. For **BC2**, the highest increase in the expression was detected for the U-251 cells. A similar approximately three-fold increase in *LC3* was observed in the GBM cells after incubation with OSI. However, this compound caused a higher upregulation in the PC-9 cells (more than seven-fold). It is worth noting that OSI is known for its pro-autophagic behavior as a result of oxidative stress[45,53]. An interesting landscape of the *mTOR* expression in tested cell lines was observed after treatment with **BC2** and OSI. Extremely strong stimulation of the *mTOR* mRNA levels was observed for the PC-9 cells. The terpyridine derivative that was evaluated caused about a 33-fold increase, and OSI caused an approximately 466-fold increase in the expression of this gene. An enhancement of the *mTOR* transcript production might be associated with the activation of the Nrf2 protein, as was observed in a protein study (Fig. 5). Thus, the cross-talk between mTOR and Nrf2 might be due to the involvement of these molecules in protecting cells from oxidative stress and regulating the protein metabolism[54]. In the U-251 cell line, **BC2** reduced the *mTOR* levels (more than three-fold), which may indicate the involvement of another mechanism of signaling that leads to the induction of oxidative stress and cell death.

Analysis of the protein expression

To confirm and expand our earlier results, the influence of the tested **BC2** derivative on several proteins responsible for cell cycle progression, antioxidant response, cell metabolism behavior, and apoptosis induction was also evaluated. The results from western blot analyses are presented in Fig. 5. The densitometric analyses are presented in Figs. S16 and S17 in the Supporting Information. Continuing our team's recent studies on 4′-phenyl-2,2′:6′,2″-terpyridine ligands[29,30], we decided to investigate the interaction of **BC2** with critical proteins regulating the transition between cell cycle phases more broadly, considering cyclins, cyclin-dependent kinases, $p21^{Waf1/Cip1}$, and $p27^{Kip1}$. Notably, **BC2** affected the cell cycle arrest in the G0/G1 phase in both of the tested cell lines. A decrease in the cdc25c and cyclin A2 expression was observed in the PC-9 cells after treatment with **BC2** and OSI, as expected. A similar situation was observed in the U-251 cells, except for an increase in cyclin A2 levels for the lowest **BC2** concentration (5.1 µM). Additionally, the cdc2 and cyclin B1 expression was downregulated in the U-251 cells. These proteins enable a complete transition from the G2 phase to the M phase. Both cyclins A2 and B1 bind to the cdc2 protein, thereby causing its activation, which promotes the transition between the phases and then drives the exit from mitosis[55,56]. The cdc25a protein undergoes reciprocal activation with the cyclin B1/cdc2 complex[57].

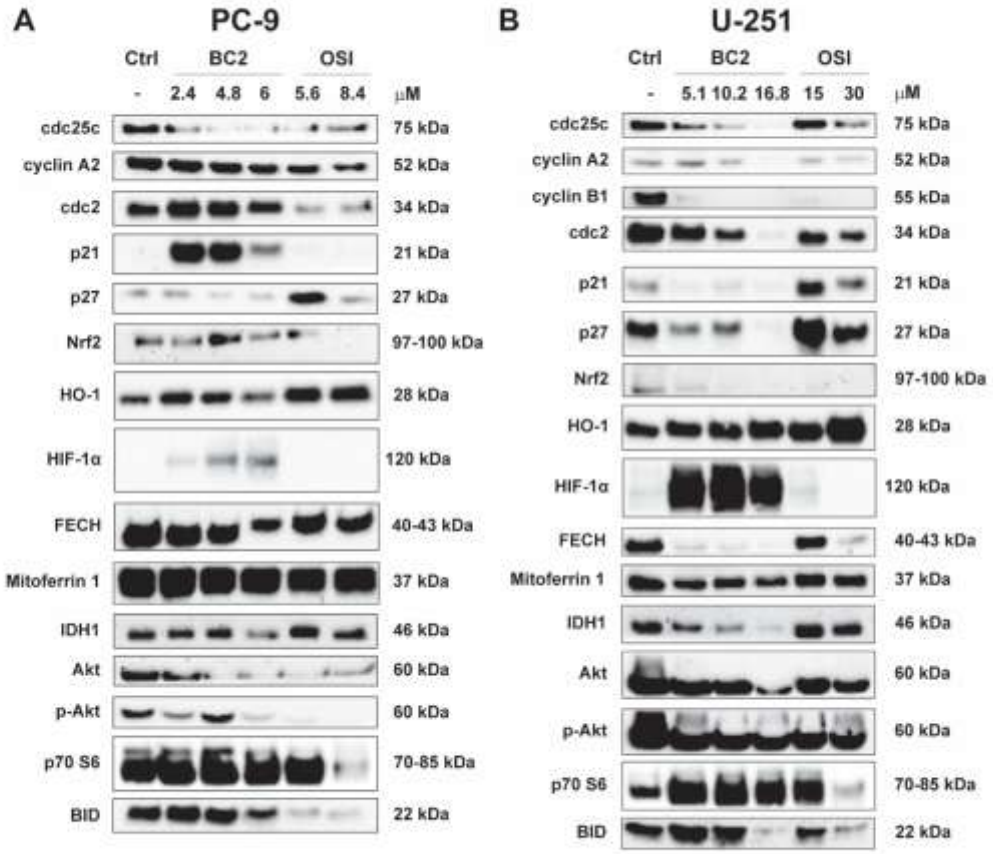

Fig. 5. Expression of selected proteins in the PC-9 (A) and U-251 (B) cancer cell lines. The cells were treated with **BC2** and OSI. The densitometric analyses of the target proteins were normalized to a reference protein, and compared to the control (Fig. S15 and S16). The results consist of the mean ± SD from at least four independent measurements. Immunoblots shown are representatives from these independent experiments. The displayed blots were cropped, and the full-length blots are shown in **S18**.

Hence, its expression is relatively low due to the inhibition of the cycle in the earlier phases. Another studied protein was $p27^{Kip1}$. $p27^{Kip1}$ is a negative regulator of the cell cycle through binding to the cyclin E1/cdk2 complex, thus causing its inactivation and G0/G1 arrest. Via feedback, the complex induces p27 phosphorylation and its degradation[58]. Our analyses indicated that the $p27^{Kip1}$ expression decreased in a concentration-dependent manner after exposure to **BC2**. This tendency was apparent in both of the tested cells. Our findings are surprising because p27 should increase during the G0/G1 cell arrest. Additionally, Radisavljević et al.. showed that the Au (III) terpyridine complex caused an increase in the level of the p27 transcript, which is associated with cell arrest in the G1 phase[59]. However, it cannot be ruled out that the lack of increased levels of the p27 protein in our assays was because it had been degraded in the proteasome. Notably, in our earlier research, there was a decrease in the cyclin E1 expression after treatment with 4′-phenyl-2,2′:6′,2″-terpyridine with a pyridine ring that induced G0/G1 arrest[59]. Similar findings were reported for the terpyridine Cu (II) complexes[15]. Another cyclin E1/cdk2 complex activity inhibitor and blocker of cell cycle progression is the $p21^{Waf1/Cip1}$ protein, which also plays a key role in oxidative stress response and apoptosis induction.

Interestingly, the expression of the p21 protein in the PC-9 and U-251 cells differed after incubation with **BC2**. Namely, a downregulation of the p21 expression in lung cancer cells was observed. Conversely, an increase in the p21 levels was registered in the U-251 cells. Our experience with the behavior of p21 in cells demonstrates that the molecule is an important driving force that responds to and stimulates various cellular responses to the destabilization of cellular redox homeostasis[29,30,60]. Additionally, the regulation of p21 might be associated

with the differential vulnerability and specificity of cells to fluctuations in ROS levels and metal chelation[61]. The enhancement of the p21 levels might be associated with the early signs that drive the launch of apoptosis[62–64]. It is also worth noting that the activation of p21 causes an interaction with antioxidant pathways, such as Nrf2, to protect cells from oxidative damage[65]. A greater than 1.5-fold increase in the Nrf2 protein expression was only observed in the PC-9 cells after treatment with **BC2** at a concentration of 4.8 µM. In the other cases, we observed a slight decrease in protein levels in PC-9 and a clear decrease in its expression in the U-251 cells. Moreover, the expression of this antioxidant protein almost vanished in GBM cells after exposure to 10.2 and 16.8 µM of **BC2**. Changes in the Nrf2 expression could suggest the activation of the antioxidant defenses, as was also indicated by the expression results of the *SOD1*, *SOD2*, and *TXN2* genes, and then the collapse of the system's capacity due to its inability to nullify ROS. In addition, the Nrf2 expression can be rapidly suppressed at high levels of oxidative stress; however, the mechanism of this has not yet been fully elucidated[66]. Moreover, a significant increase in the heme oxygenase-1 (HO-1) levels was observed in both of the tested cell lines. The HO-1 protein plays a key role in many cellular processes, including cellular defense and heme degradation in mammalian cells, thereby conserving its anti- and pro-apoptotic activity[67]. Usually, the upregulation of heme oxygenase is a crucial response to the induction of oxidative stress through its participation in heme degradation into ferrous iron (then ferritin), carbon monoxide, and biliverdin (further to bilirubin), which can act as antioxidants[68]. On the other hand, an increase in the oxygen concentration as a result of a disturbance in redox homeostasis could also induce HO-1 activity as well as HIF-1α. In this study, a significant, more than five-fold, increase in the expression HIF-1α was observed in the PC-9 cells after exposure to **BC2** (2.4 µM). The observed upregulation effect intensified in a concentration-dependent manner. In the case of the U-251 cells, **BC2** at all of the doses that were administered caused a significant, more than ten-fold increase in the HIF-1α protein expression. These results may suggest that HIF-1α is involved in oxidative stress activation, which has also been demonstrated elsewhere[69]. In contrast, OSI caused an increase in HO-1 levels but without activating the hypoxia factor in either of the tested cell lines.

The induction of oxidative stress in cells causes impaired mitochondrial function, reduced ATP production, proton leakage, and the disruption of overall cellular metabolism. Therefore, we decided to examine the effects of the tested compounds on several proteins (mitoferrin-1, ferrochelatase (FECH), and IDH1) that are associated with the mitochondria and the regulation of cellular functions, including metabolism, growth, and proliferation. Activation of the heme degradation pathway *via* an increased HO-1 expression might enhance the iron availability in the mitochondrial pool. Thus, overloading mitochondria with iron might block its uptake and transport *via* the mitoferrin-1 transporter[70]. In addition, mitoferrin-1 may bind to FECH and the ABCB10 transporter, thus creating an oligomeric complex that collaborates to import iron. On the other hand, the disintegration of mitochondria could affect the degradation of the Fe-S cluster assembly machinery, thereby leading to the demise of the mature pool of FECH[71]. Our analysis showed that the FECH levels were lower after **BC2** was administered in both of the tested cell lines. Moreover, a significant decrease in the mitoferrin-1 transporter activity was observed in the GBM cells. In contrast, a negligible decrease in the level of this protein was observed in the PC-9 cell line. IDH1 is one of the key enzymes in the tricarboxylic acid cycle (TCA), which is involved in the oxidative decarboxylation of isocitrate into α-ketoglutarate *via* the transformation of NADP+ into NADPH. Moreover, the role of IDH1 in maintaining the NADPH pool for the two antioxidant systems in the context of the redox balance has also been described, as well as the association of IDH1 with the induction of oxidative stress[72,73]. The downregulation of IDH1 was detected in the PC-9 cells after exposure to **BC2** at the highest concentration (6 µM). In addition, a decrease in the IDH1 expression in the GBM cells in a concentration-dependent manner was also observed. Notably, a similar decrease in the IDH1 activity level (almost two-fold) was registered for **BC2** at 6 µM and 10.2 µM in the PC-9 and U-251 cells, respectively. These results appeared to correlate with the decreased *CAT* mRNA expression in both cell lines. Interestingly, the literature data showed that higher IDH1 levels are associated with catalase activation, thus leading to the suppression of oxidative stress induction and cell survival[74]. Thus, our findings might have revealed the multilayered destabilization of redox homeostasis by terpyridine derivatives in the tested cells.

Lastly, the activation of the Akt signaling pathway and the proteins that participate in triggering cell death *via* apoptosis (p70 S6 and BID) were assessed. Generally, the **BC2** compound caused an inhibition of Akt phosphorylation at serine 473 in both of the tested cell lines. One exception was observed in lung cells after incubation with **BC2** at 4.8 µM, which may be associated with an unexpected increase in the Nrf2 level. However, it is worth emphasizing that **BC2** can block the pro-survival signaling that is mediated by the Akt protein. One downstream target of the Akt pathway is p70 S6, which is involved in cell growth and proliferation. However, p70 S6 also has a significant effect on the induction of apoptosis, which is mediated by a caspase-dependent pathway. Indeed, the p70 S6 kinase may be a substrate for caspase-3, which cleaves it[75]. The cleavage of p70 S6 was observed in both the PC-9 and U-251 cell lines after incubation with the tested compound. Hence, the results might suggest that the induction of apoptosis, the cell death that is regulated by caspase activation, was observed. Our assumption was confirmed by the BID expression, which had a pro-apoptotic role in cells. We detected the upregulation of BID after treatment with the **BC2** derivative. Interestingly, BID might also provide a molecular switch between apoptosis and autophagy[76]. This, in turn, may explain the different responses to OSI in the cells and the downregulation of the BID expression.

Conclusion

In this paper, the anticancer properties of newly synthesized and well characterized 2,2′:6′,2″-terpyridine complexes with Zn^{2+}, Y^{3+}, Hg^{2+}, Cd^{2+}, Cu^{2+}, and Fe^{3+} (compounds **BC1**-**BC6**) are discussed. To evaluate the inhibitory properties of cell proliferation, cell lines representing different types of cancer, from the most common to the most difficult to treat, were selected. The highest antiproliferative activity was registered for the PC-9 cell line. However, the tested compounds also exhibited an interesting activity profile against other lines as well. For

a more thorough analysis of the mechanism of action, a **BC2** derivative that exhibited high activity (IC_{50} = 0.605 μM), but also selectivity (SI > 41.32) against normal cells was used. However, it is worth mentioning that in most cases, the presented library of terpyridine derivatives exhibited a higher activity (IC_{50} below 2 μM) and better selectivity than the well-known drug OSI, which served as a positive reference in further studies.

The cell cycle analysis that was conducted on the PC-9 and U-251 cell lines showed that the **BC2** derivative affected the cell cycle inhibition at the G0/G1 stage. This result was confirmed using the western blot technique, where an expressed decrease in the protein levels of p27, cdc25c, cyclin A1 (both cell lines), and additionally cyclin B1 and cdc2 (for U-251 cells) was observed. The inhibition of the cell cycle was confirmed using flow cytometry, which was also used to evaluate the cell death pathway. The cells of both of the tested lines exhibited clear apoptotic features after incubation with the **BC2** derivative, which was also confirmed at the protein level and was manifested as an effect at the p21 levels (increase in PC-9, decrease in U-251). The differences in the cellular response might be due to differences in the cellular response to the ROS activation and metal chelation, depending on the cell line that was evaluated. Further evidence of apoptosis was a decrease in the Akt levels, including the inhibition of Akt phosphorylation, the direct result of which is the cleavage of p70 S6 and the activation of the BID protein.

However, BID is also an activator of autophagy. Therefore, we confirmed this result at the transcript level, where the upregulation of *LC3* was observed. This evidence proved that autophagy also plays an important role in the mechanism of action of the studied derivative. As a direct result, there was also a dramatic increase in the level of *mTOR* for the PC-9 line. Interestingly, a decrease in *mTOR* was observed for the U-251 line, which might indicate the involvement of other pathways that are associated with the occurrence of oxidative stress.

The experiments in which the intracellular reactive oxygen species level was measured in the U-251 and PC-9 cells after treatment with **BC2** indicated a higher level after 24 h of incubation. An increase in the concentration of ROS is always associated with the activation of the antioxidant systems that protect cells from their harmful effects. Therefore, in a further step, the expression level of the genes associated with the defense against the induction of oxidative stress, such as *SOD1*, *SOD2*, *CAT*, and *TXN2*, was determined. The results indicated the induction of a cellular response in the form of an increase in their expression (*SOD1*, *SOD2*, and *TXN2* in PC-9 cells; *SOD2* in U-251 cells) or a decrease in their expression (*CAT* both cell lines; *SOD1* and *TXN2* in U-251 cells). However, as was previously mentioned, the change in the level of genes that are involved in the oxidative processes relative to the control indicated that the final cytotoxic effect of the bis(terpyridine) complexes is associated with the generation of ROS, and thus, the induction of changes in the ROS defense system. The pronounced effect on the entire antioxidant cellular system by the tested compounds was also confirmed by a decrease in the antioxidant protein Nrf2 and an increase in the HO-1 and HIF-1α levels.

Other analyzed genes connected with cellular proliferation and the pro-survival processes, whose expression decreased, were *PIK3CA* and *MAPK1*. In addition, a decrease in the mitoferrin-1, FECH, and IDH1 protein levels was also registered. This is evidence of the effects of the tested compounds on multiple cellular pathways that are connected with metabolism, growth, and proliferation that are more or less interrelated.

Experimental section

Synthesis

All chemicals and starting materials used in this study were commercially available and were utilized without additional purification. Solvents were distilled following standard methods and purged with nitrogen before use to ensure an oxygen-free environment. Throughout the reactions, an argon atmosphere was maintained. Column chromatography was conducted using Merck silica gel as the stationary phase. Thin-layer chromatography (TLC) was performed on silica gel plates (Merck TLCSilicaGel60) to monitor the reactions' progress and assess the products' purity. Nuclear magnetic resonance (NMR) spectra were acquired in deuterated chloroform utilizing a Bruker Advance 400 MHz spectrometer, which was capable of recording both ^{1}H and ^{13}C NMR spectra. For high-resolution electrospray ionization mass spectrometry (HR-ESI-MS) measurements, a quadrupole time-of-flight (QTOF) mass spectrometer QTOF (Impact HD, Bruker Daltonics) was employed. This instrument allowed for high-resolution and accurate mass determinations of the analyzed compounds.

General synthesis procedure of bis(terpyridine) complexes

In a 50 mL round-bottom flask, a total of 0.146 mmol (0.089 g) of terpyridine ligand and 0.073 mmol of an appropriate inorganic salt (as metal precursors) were combined with 20 mL of acetonitrile (ACN). The mixture was subjected to a temperature of 90 °C and maintained at this temperature for 1.5 h. Subsequently, the mixture was allowed to cool down to 40 °C, and 10 mL of methylene chloride (DCM) was introduced through a condenser. The resulting mixture was stirred for an additional 30 min. To isolate the desired product, the volatile components were removed using a vacuum rotary evaporator. The resulting residue was dissolved in a small amount of ACN. Then, diethyl ether was added to the solution. The mixture was then filtrated through a fritted funnel, and the resulting precipitate was washed successively with water, methanol, and diethyl ether. The pure product obtained after the washing steps was dried under vacuum conditions. The resulting product was obtained as a yellow-orange solid.

BC1: Yield: 72%, HR-ESI-MS: *m/z* calcd. for $C_{86}H_{76}ZnN_8$ $[M]^{2+}$ 642.2737; found 642.2767.

BC2: Yield: 44%, HR-ESI-MS: *m/z* calcd. for $C_{86}H_{78}N_8$ $[M+2\,H]^{2+}$ 611.3169; found 611.4000.

BC3: Yield: 40%, HR-ESI-MS: *m/z* calcd. for $C_{86}H_{76}HgN_8$ $[M]^{2+}$ 711.2953; found 711.2978.

BC4: Yield: 52%, HR-ESI-MS: *m/z* calcd. for $C_{86}H_{76}CdN_8$ $[M]^{2+}$ 667.2621; found 667.2612.

BC5: Yield: 38%, HR-ESI-MS: *m/z* calcd. for $C_{86}H_{76}CuN_8$ $[M]^{2+}$ 641.7739; found 641.7767.

BC6: Yield: 42%, HR-ESI-MS: *m/z* calcd. for $C_{86}H_{76}FeN_8$ $[M]^{2+}$ 638.2767; found 638.2780; *m/z* calcd. for $C_{87}H_{77}FeN_8O_2$ $[M+HCOOH]^{2+}$ 1321.5517; found 1321.5510.

Cell culture

All experiments were performed on two human cancer cell lines: the lung adenocarcinoma PC-9 (purchased from Sigma Aldrich) and the GBM U-251 (provided by Prof. G. Kramer-Marek from the Institute of Cancer Research in London, England). Additionally, during cytotoxicity studies, the activity of tested compounds was measured on the MCF-7 human breast carcinoma cell line (obtained from ATCC), the human U-87 MG GBM cell line (obtained from ATCC), the human pancreatic cancer cell line PANC-1 (acquired from Sigma Aldrich) and the NHDF normal human fibroblast cell line (purchased from PromoCell). All cells were cultured in 75 cm^2 flasks (Nunc) at 37 °C in a humid atmosphere with 5% CO_2. The medium chosen for MCF-7, PANC-1, U-251, and U-87 MG cell lines was Dulbecco's Modified Eagle's Medium (DMEM) with 10% heat-inactivated fetal bovine serum (FBS, Sigma Aldrich), the same medium was used for cultivation of NHDF cells but with 15% non-inactivated FBS instead. The PC-9 cell line was cultivated in the RPMI-1640 medium with 10% heat-inactivated FBS. To prevent contamination of cell cultures, 1% v/v addition of penicillin/streptomycin (Gibco) was added to each medium, and all cell lines were examined for the presence of *Mycoplasma* strains using the polymerase chain reaction (PCR) technique with specific primers.

Cytotoxicity studies

All the cells were seeded in 96-well clear plates (Nunc) at a density of 5,000 cells suspended in 100 µL of appropriate culture medium per well for all cell lines except for NHDF, which was seeded in the same volume but at a density of 4,000 cells per well. The day after seeding, the solutions of tested compounds dissolved in medium were freshly prepared. Next, the old medium was discarded from plates and exchanged with 200 µL of the compound solutions, then left in an incubator for 72 h. After the incubation, the contents of the wells were again removed. 100 µL of the medium lacking phenol red and 20 µL of CellTiter 96®AQ_{ueous} One Solution-MTS (Promega) were added into the wells, and plates were incubated in the darkness. After waiting for ~ 1 h, depending on the cell line, plates were read using a multi-plate reader (Varioskan LUX, Thermo Scientific) at a wavelength of 490 nm. Each plate contained 2–4 wells of untreated cells, used as a control sample. Values of inhibitory concentration (IC_{50}) were determined with GraphPad Prism 9 as a concentration at which a 50% decrease in proliferation is expected. All experiments were incubated at 37 °C in a humidified atmosphere of 5% CO_2. Each tested concentration of a compound was measured in duplicate, and experiments were performed four to five times depending on the cell line.

Cytotoxicity with metal ions

For the evaluation of the influence of the metal ions on compounds' cytotoxicity U-251 and PC-9 cell lines were selected based on the results of the regular cytotoxicity assays. Solutions of compounds were prepared for both used cell lines in their four times IC_{50} concentration and mixed in 1:1 ratio with 40 µM solutions of Cu^{2+}, Fe^{2+}, Fe^{3+} and Zn^{2+} ions. Final obtained solutions consisted of two times IC_{50} solutions of tested compounds mixed with 20 µM solutions of respective ions. Addition of 20 µM solutions of these ions does not influence the cell viability. Cytotoxicity was determined using the procedure described in Sect. 4.3. All experiments were incubated at 37 °C in a humidified atmosphere of 5% CO_2. Each tested concentration of a compound was measured in duplicate, and experiments were performed three times on both cell lines.

Cell cycle assay

The U-251 and PC-9 cells were seeded in clear 6-well plates (Nunc) at a density of 200,000 cells in 1 mL of culture medium per well and then incubated at 37 °C for 24 h. Following the incubation, the medium was discarded, and freshly prepared solutions of compounds in appropriate culture medium were mixed: 5.1 µM, 10.2 µM, and 16.8 µM solutions of BC2 and 15 µM or 30 µM solutions of OSI for U-251 cells; 2.4 µM, 4.8 µM, and 6 µM solutions of BC2 and 5.6 µM or 8.4 µM solutions of OSI for PC-9 cells. After 24 h of treatment with the compounds, assays were performed using a Muse Cell Cycle Kit (Millipore) according to the manufacturer's protocol. The cells were collected using 0.05% trypsin-EDTA and centrifuged (5 min, 300g). Then, the supernatant was removed. Next, the pellet was washed with 1 mL of cold phosphate-buffered saline (PBS) and centrifuged again. The obtained pellet was dissolved in 1 mL of ice-cold 70% ethanol and kept in the freezer overnight. The next day, the cells were centrifuged, washed with PBS, centrifuged again, and then suspended in 200 µL of Muse Cell Cycle Reagent. After 30 min of incubation in the dark, a flow cytometry assay was performed using a Muse Cell Analyzer (Millipore). The experiments were performed at least four times.

Annexin V binding assay

The U-251 and PC-9 cells were seeded in the same quantity and identical conditions as for cell cycle assay (Sect. 4.5). The next day, the same solutions of both tested compounds as the cell cycle assay were mixed and added to the wells. After 48 h of incubation, the apoptosis assay was measured using a FITC Annexin V Apoptosis Detection Kit with 7-AAD (Biolegend) following the manufacturer's protocol. The collection of cells was performed the same way as the cell cycle assay until the second centrifugation. The pellet obtained this way was suspended in 100 µL of Muse Annexin V Binding Buffer mixed with 5 µL each of FITC Annexin V and 7-AAD. Samples were vortexed and kept in the dark for 15 min. The number of live cells and cells in various apoptotic stages were measured using a Muse Cell Analyzer. The experiments were performed at least four times.

Immunoblotting

The U-251 and PC-9 cells were seeded in 3 cm plastic Petri dishes (Nunc) at a density of 500,000 cells in 1 mL of culture medium per dish and then incubated at 37 °C for 24 h. Afterward, cells were treated with the same concentrations of both compounds as Sect. 4.5 and 4.5. After 24 h of incubation, the cells were removed from the dishes using 0.05% trypsin-EDTA, centrifuged (5 min, 2000 rpm), and then the obtained pellets

were resuspended in 300 µL of a RIPA buffer consisting of Halt Phosphatase Inhibitor Cocktail, Halt Protease Inhibitor Cocktail, and 0.5 M EDTA (all from Thermo Scientific). Cell suspensions were kept on ice for the entirety of the following process. After a 20 min incubation on a rocker, cells were lysed with 15 s sonication. Lysates were then centrifuged (10 min, 10,000 rpm) to remove the debris. The supernatant was collected and stored at -80 °C. The protein content of the lysates was assessed using the western blot technique. The amount of protein present in samples was measured the day before each experiment using a Micro BCA Protein Assay Kit (Thermo Scientific) according to the manufacturer's protocol. 16 µg of protein mixed with NuPAGE LDS Sample Buffer (Thermo Scientific) were prepared and separated using the SDS-PAGE. After electrophoresis, proteins were wet-transferred from the gel to the nitrocellulose membrane. Then, the obtained membranes were blocked for 1 h in TBS buffer with 5% non-fat milk powder and 0.1% Tween-20 (TBST) and cut into strips according to the molecular weight of the proteins. Overnight, the strips were incubated with following primary antibodies: HIF-1α (#14179, Cell Signalling Technology - CST); IDH1 (#8137, CST); Nrf2 (#12721, CST); BID (#2002, CST); cdc2 (#9116, CST); cdc25c (#4688, CST); cyclin A2 (#4656, CST); cyclin B1 (#4138, CST); $p21^{Waf1/Cip1}$ (#2947, CST); $p27^{Kip1}$ (#3688, CST); FECH (sc-377377, Santa Cruz Biotechnology); HO-1 (#5853, CST); mitoferrin 1 (26469-1-AP, Proteintech); Akt (#9272, CST); phospho-Akt (Ser473) (#4060, CST); p70 S6 kinase (#2708, CST). All antibodies were diluted 1:1000 in TBST buffer, and the reference proteins: vinculin (#13901, CST); GAPDH (#2118, CST); β-actin (#3700, CST) were diluted 1:2000 in the same buffer. Incubated strips were washed three times with TBST buffer, followed by 1 h of incubation in horseradish peroxidase (HRP)-conjugated secondary antibodies (CST) solutions at room temperature. After three more washes in the TBST buffer, all strips were incubated for 5 min in SuperSignal West Pico Chemiluminescent Substrate (Thermo Scientific). The chemiluminescence of the proteins on the nitrocellulose membrane strips was assessed using a ChemiDoc XRS + System (Biorad). The experiments were repeated four to five times. Densitometric analysis was performed using ImageJ software (Wayne Rasband, National Institutes of Health, USA).

Detection of reactive oxygen species

The U-251 and PC-9 cells were seeded in black 96-well plates with a clear bottom (Corning) at a density of 9,000 cells in 100 µL of culture medium per well and then incubated at 37 °C for 24 h. Solutions of the compounds in concentrations described in Sect. 4.5–4.7 were prepared and added to the wells in several timestamps that allowed one to check the ROS levels after 3, 6, 9, 12, and 24 h of incubation at the same time. The experiments' results were measured using a CellROX® Green Reagent (Molecular Probes). Results were normalized by comparing the levels of ROS to the number of cells present in a well. The population of cells was estimated by staining with Hoechst 33,342 (Molecular Probes). Fluorescent signal was read using a multi-plate reader (Varioskan LUX) at a wavelength of 520 nm for CellROX® Green Reagent and 486 nm for Hoechst 33,342. The experiment was repeated at least three times, and the obtained results were presented in the form of percentages of the ROS levels in relation to untreated cells.

Cytotoxicity with an antioxidant

U-251 and PC-9 cells were seeded into clear 96-well plates (Nunc) at a density of 9,000 cells per well in 100 µL of culture medium and incubated at 37 °C for 24 h. The **BC2** compound was then added at concentrations of 5.1 µM and 10.2 µM for U-251 cells, and 4.8 µM and 6 µM for PC-9 cells. Ascorbic acid, serving as an antioxidant, was added at a concentration of 100 µM either alone or in combination with the **BC2** compound to assess its effect. Following an additional 24 h of incubation, cytotoxicity was determined using the procedure described in Sect. 4.3. The experiment was repeated three times, and the results were presented as percentages of living cells relative to untreated controls.

Analysis of mRNA expression

On 3 cm Petri dishes (Nunc), two cell lines (U-251 and PC-9) were seeded at a density of 500,000 cells per well. After the 24 h incubation period at 37 °C, the solutions of compounds were prepared and added to the petri dish (OSI at a concentration of 30 µM and 8 µM for U-251 and PC-9 cells, respectively; **BC2** at a concentration of 10.2 µM and 6 µM for U-251 and PC-9 cells, respectively). RNA was isolated after 24 h using TRIzol Reagent (Ambion) in accordance with manufacturer's instructions. cDNA was synthesized using ProtoScript II First Strand cDNA Synthesis Kit (New England BioLabs) from 1 µg of total RNA, which was measured using a NanoDrop 2000/2000c spectrophotometer (Thermo Scientific™). Real-time (RT) quantitative PCR (qPCR) was performed using a QuantStudio 5 RT PCR system for human identification (Applied Biosystems) and CTX96 Touch™ RT PCR detection system (Biorad) in a 10 µL reaction volume. The qRT-PCR reactions were performed with Luna® Universal qPCR Master Mix (New England BioLabs), a primer pair mix (0.5 µM each), and 1 µL of cDNA. Each reaction was performed under the same conditions, which were as follows: initial denaturation at 95 °C for 60 s; followed by 40 denaturation cycles at 95 °C for 15 s; extension at 60 °C for 30 s with plate read and after all the programmed cycles melt curve stages with step one at 95 °C for 15 s, step two at 60 °C for 60 s, and step 3 at 95 °C for 15 s. The gathered data was analyzed with the comparison to the reference gene (HPRT1) using the $2^{-\Delta\Delta CT}$ method. Each experiment was done at a minimum of three times. The primer sequences are given in Table S2.

Statistical analysis

All statistical analyses executed during this research used GraphPad Prism 9 software. Results obtained during the cell cycle assay, Annexin V binding assay, and ROS level measurements were analyzed using one-way ANOVA multi-comparisons analysis with Dunnett's test as a result correction. Analysis of mRNA expression was carried out using a two-way ANOVA multiple comparison test followed by Dunnett's test correction.

Data availability

Raw data are available upon request from the reviewer. Contact person - Anna Mrozek-Wilczkiewicz (anna.mrozek-wilczkiewicz@us.edu.pl).

Received: 13 August 2024; Accepted: 23 October 2024
Published online: 06 November 2024

References

1. Bray, F. et al. Global cancer transitions according to the Human Development Index (2008–2030): a population-based study. *Lancet Oncol.* **13** (8), 790–801 (2012).
2. Wong, M. C. S. et al. Global temporal patterns of pancreatic cancer and association with socioeconomic development. *Sci. Rep.* **7** (1), 3165 (2017).
3. Sung, H. et al. Global Cancer statistics 2020: GLOBOCAN estimates of incidence and Mortality Worldwide for 36 cancers in 185 countries. *Cancer J. Clin.* **71** (3), 209–249 (2021).
4. Ostrom, Q. T. et al. CBTRUS Statistical Report: primary brain and other central nervous system tumors diagnosed in the United States in 2010–2014. *Neuro Oncol.* **19** (suppl_5), v1–v88 (2017).
5. Niedbala, M. et al. Glioblastoma: pitfalls and opportunities of immunotherapeutic combinations. *Onco Targets Ther.* **15**, 437–468 (2022).
6. Mizrahi, J. D. et al. Pancreatic cancer. *Lancet.* **395** (10242), 2008–2020 (2020).
7. Ndagi, U., Mhlongo, N. & Soliman, M. E. Metal complexes in cancer therapy - an update from drug design perspective. *Drug Des. Dev. Therapy.* **11**, 599–616 (2017).
8. Gasser, G. Metal complexes and medicine: a successful combination. *Chimia.* **69** (7–8), 442–446 (2015).
9. Dasari, S. & Tchounwou, P. B. Cisplatin in cancer therapy: molecular mechanisms of action. *Eur. J. Pharmacol.* **740**, 364–378 (2014).
10. Ghosh, S. Cisplatin: the first metal based anticancer drug. *Bioorg. Chem.* **88**, 102925 (2019).
11. Pignata, S. et al. A phase II study of weekly carboplatin and paclitaxel as first-line treatment of elderly patients with advanced ovarian cancer. A Multicentre Italian Trial in ovarian cancer (MITO-5) study. *Crit. Rev. Oncol. Hematol.* **66** (3), 229–236 (2008).
12. Pujade-Lauraine, E. et al. Pegylated liposomal doxorubicin and carboplatin compared with Paclitaxel and Carboplatin for patients with platinum-sensitive ovarian cancer in late relapse. *J. Clin. Oncol.* **28** (20), 3323–3329 (2010).
13. Dewdney, A. et al. Multicenter randomized phase II clinical trial comparing neoadjuvant oxaliplatin, capecitabine, and preoperative radiotherapy with or without cetuximab followed by total mesorectal excision in patients with high-risk rectal cancer (EXPERT-C). *J. Clin. Oncol.* **30** (14), 1620–1627 (2012).
14. Song, N. et al. Clinical outcome from oxaliplatin treatment in stage II/III Colon cancer according to intrinsic subtypes: secondary analysis of NSABP C-07/NRG oncology Randomized Clinical Trial. *JAMA Oncol.* **2** (9), 1162–1169 (2016).
15. Zych, D. et al. 4'-Phenyl-2,2':6',2''-terpyridine derivatives containing 1-Substituted-2,3-Triazole Ring: synthesis, characterization and anticancer activity. *Chemistryselect.* **3** (24), 7009–7017 (2018).
16. Li, C. et al. Platinum(II) Terpyridine Anticancer complexes possessing multiple Mode of DNA Interaction and EGFR inhibiting activity. *Front. Chem.* **8**, 210 (2020).
17. Behera, S. et al. Protein interactions, molecular docking, antimicrobial and antifungal studies of terpyridine ligands. *J. Biomol. Struct. Dyn.* **41**(20), 11274–11285 (2023).
18. Anthonysamy, A. et al. Synthesis, characterization and electrochemistry of 4'-functionalized 2,2':6',2''-terpyridine ruthenium(II) complexes and their biological activity. *Dalton Trans.* **16**, 2136–2143 (2008).
19. Saccone, D. et al. Terpyridine and Quaterpyridine Complexes as sensitizers for photovoltaic applications. *Mater. (Basel).* **9**(3), 137 (2016).
20. Winter, A. et al. Self-assembly of π-conjugated bis(terpyridine) ligands with zinc(II) ions: New metallosupramolecular materials for optoelectronic applications. *J. Polym. Sci., Part A: Polym. Chem.* **47** (16), 4083–4098 (2009).
21. Wang, S. et al. Fine tuning of Multiphoton AIE Emission Behavior, Organelle Targeting, and fluorescence lifetime imaging of terpyridine derivatives by Alkyl Chain Engineering. *Anal. Chem.* **94** (10), 4335–4342 (2022).
22. Zhao, L. X. et al. Synthesis, topoisomerase I inhibition and antitumor cytotoxicity of 2,2':6',2-, 2,2':6',3- and 2,2':6',4-terpyridine derivatives. *Bioorg. Med. Chem. Lett.* **11**(19), 2659–62 (2001).
23. Kargos, J. et al. Highly cytotoxic copper(II) terpyridine complexes as anticancer drug candidates. *Inorg. Chim. Acta.* **516**, 120137 (2021).
24. Gu, Y. Q. et al. Terpyridine copper(II) complexes as potential anticancer agents by inhibiting cell proliferation, blocking the cell cycle and inducing apoptosis in BEL-7402 cells. *Dalton Trans.* **51** (5), 1968–1978 (2022).
25. Mendo, A. S. et al. Characterization of antiproliferative potential and biological targets of a copper compound containing 4'-phenyl terpyridine. *J. Biol. Inorg. Chem.* **20** (6), 935–948 (2015).
26. Gliišić, B. Đ. et al. Synthesis, cytotoxic activity and DNA-binding properties of copper(II) complexes with terpyridine. *Polyhedron.* **139**, 313–322 (2018).
27. Grau, J. et al. The effect of potential supramolecular-bond promoters on the DNA-interacting abilities of copper-terpyridine compounds. *Dalton Trans.* **44** (36), 16061–16072 (2015).
28. Liang, J. W. et al. Synthesis, DNA interactinn and anticancer activity of copper(II) complexes with 4'-phenyl-2,2':6',2''-terpyridine derivatives. *J. Inorg. Biochem.* **141**, 17–27 (2014).
29. Malarz, K. et al. New derivatives of 4'-phenyl-2,2':6',2''-terpyridine as promising anticancer agents. *Eur. J. Med. Chem.* **212**, 113032 (2021).
30. Malarz, K. et al. Anticancer activity of 4'-phenyl-2,2':6',2''-terpyridines - behind the metal complexation. *Eur. J. Med. Chem.* **189**, 112039 (2020).
31. Szatrowski, T. P. & Nathan, C. F. Production of large amounts of hydrogen-peroxide by human tumor-cells. *Cancer Res.* **51** (3), 794–798 (1991).
32. Pelicano, H., Carney, D. & Huang, P. ROS stress in cancer cells and therapeutic implications. *Drug Resist. Updates.* **7** (2), 97–110 (2004).
33. Trachootham, D., Alexandre, J. & Huang, P. Targeting cancer cells by ROS-mediated mechanisms: a radical therapeutic approach? *Nat. Rev. Drug Discov.* **8** (7), 579–591 (2009).
34. Wang, J. & Yi, J. Cancer cell killing via ROS: to increase or decrease, that is the question. *Cancer Biol. Ther.* **7** (12), 1875–1884 (2008).
35. George, S. & Abrahamse, H. Redox potential of antioxidants in cancer progression and prevention. *Antioxid. (Basel).* **9**(11), 1156 (2020).
36. Harris, I. S. et al. Glutathione and thioredoxin antioxidant pathways synergize to drive cancer initiation and progression. *Cancer Cell.* **27** (2), 211–222 (2015).
37. Ryter, S. W. & Choi, A. M. Heme oxygenase-1: redox regulation of a stress protein in lung and cell culture models. *Antioxid. Redox Signal.* **7** (1–2), 80–91 (2005).

38. Zych, D. et al. Highly luminescent 4 ′-(4-ethynylphenyl)-2,2 ′:6,2 ″-Terpyridine derivatives as materials for potential applications in Organic Light Emitting diodes. *Chemistryselect.* **2** (27), 8221–8233 (2017).
39. Zych, D. et al. 4 ′-Phenyl-2,2 ′:6 ′,2 ″-terpyridine derivatives-synthesis, potential application and the influence of acetylene linker on their properties. *Dyes Pigm.* **146**, 331–343 (2017).
40. Lu, C. et al. In Vitro Photodynamic Therapy of Monomuclear and Dinuclear Iridium(III) Bis(terpyridine) complexes. *ACS Appl. Bio Mater.* **3** (10), 6865–6875 (2020).
41. Paul, S. et al. BODIPY-Ruthenium(II) Bis-Terpyridine complexes for Cellular Imaging and Type-I/-II photodynamic therapy. *Inorg. Chem.* **60** (21), 16178–16193 (2021).
42. Perillo, B. et al. ROS in cancer therapy: the bright side of the moon. *Exp. Mol. Med.* **52** (2), 192–203 (2020).
43. Hayes, J. D., Dinkova-Kostova, A. T. & Tew, K. D. Oxidative stress cancer. *Cancer Cell.* **38**(2), 167–197 (2020).
44. Zou, Z. et al. Induction of reactive oxygen species: an emerging approach for cancer therapy. *Apoptosis.* **22** (11), 1321–1335 (2017).
45. Tang, Z. H. et al. Osimertinib induces autophagy and apoptosis via reactive oxygen species generation in non-small cell lung cancer cells. *Toxicol. Appl. Pharmacol.* **321**, 18–26 (2017).
46. Fukai, T. & Ushio-Fukai, M. Superoxide dismutases role in redox signaling, vascular function, and diseases. *Antioxid. Redox Signal.* **15**(6), 1583–1606 (2011).
47. Becker, K. et al. Human thioredoxin reductase is efficiently inhibited by (2,2′:6′,2″ ′-Terpyridine)platinum(II) complexes. Possible implications for a Novel Antitumor Strategy. *J. Med. Chem.* **44** (17), 2784–2792 (2001).
48. Ahmadi, R. et al. Antiglioma activity of 2,2′:6′,2-terpyridineplatinum(II) complexes in a rat model–effects on cellular redox metabolism. *Free Radic Biol. Med.* **40** (5), 763–778 (2006).
49. Qi, X. et al. Antioxidants in brain tumors: current therapeutic significance and future prospects. *Mol. Cancer.* **21**, 204 (2022).
50. Zhang, W. & Liu, H. T. MAPK signal pathways in the regulation of cell proliferation in mammalian cells. *Cell Res.* **12** (1), 9–18 (2002).
51. Choroba, K. et al. Square planar au(III), pt(II) and Cu(II) complexes with quinoline-substituted 2,2′:6′,2″-terpyridine ligands: from in vitro to in vivo biological properties. *Eur. J. Med. Chem.* **218**, 113404 (2021).
52. Zhang, J. J. et al. Elucidating the Multimodal Anticancer mechanism of an Organometallic Terpyridine Platinum(II) N-Heterocyclic Carbene Complex against Triple-negative breast Cancer in Vitro and in vivo. *J. Med. Chem.* **66** (6), 3995–4008 (2023).
53. Kucrak, M. et al. Anticancer potential and through study of the cytotoxicity mechanism of ionic liquids that are based on the trifluoromethanesulfonate and bis(trifluoromethylsulfonyl)imide anions. *J. Hazard. Mater.* **427**, 128160 (2022).
54. Bendavit, G. et al. Nrf2 transcription factor can directly regulate mTOR. *J. Biol. Chem.* **291** (49), 25476–25488 (2016).
55. Sanchez, I. & Dynlacht, B. D. New insights into cyclins, CDKs, and cell cycle control. *Semin Cell. Dev. Biol.* **16** (3), 311–321 (2005).
56. Yam, C. H., Fung, T. K. & Poon, R. Y. C. Cyclin A in cell cycle control and cancer. *Cell. Mol. Life Sci. (CMLS).* **59** (8), 1317–1326 (2002).
57. Liu, K. et al. The role of CDC25C in cell cycle regulation and clinical cancer therapy: a systematic review. *Cancer Cell Int.* **20**, 213 (2020).
58. Xu, X. et al. Mechanism of Cdk2/Cyclin E inhibition by p27 and p27 phosphorylation. *Biochemistry.* **38** (27), 8713–8722 (1999).
59. Radisavljević, S. et al. New gold(III) chlorophenyl terpyridine complex: biomolecular interactions and anticancer activity against human oral squamous cell carcinoma. *Appl. Organomet. Chem.* **37** (1), e6922 (2023).
60. Mrozek-Wilczkiewicz, A. et al. The synthesis and anticancer activity of 2-styrylquinoline derivatives. A p53 independent mechanism of action. *Eur. J. Med. Chem.* **177**, 338–349 (2019).
61. Moussa, R. S. et al. Ironing out the role of the cyclin-dependent kinase inhibitor, p21 in cancer: novel iron chelating agents to target p21 expression and activity. *Free Radic Biol. Med.* **133**, 276–294 (2019).
62. Malarz, K. et al. The role of oxidative stress in activity of anticancer thiosemicarbazones. *Oncotarget.* **9** (25), 17689–17710 (2018).
63. Malarz, K. et al. Novel benzenesulfonate scaffolds with a high anticancer activity and G2/M cell cycle arrest. *Cancers (Basel).* **13** (8), 1790 (2021).
64. Mrozek-Wilczkiewicz, A. et al. Anticancer activity of the thiosemicarbazones that are based on di-2-pyridine ketone and quinoline moiety. *Eur. J. Med. Chem.* **171**, 180–194 (2019).
65. Chen, W. et al. Direct Interaction between Nrf2 and p21Cip1/WAF1 upregulates the Nrf2-Mediated antioxidant response. *Mol. Cell.* **34** (6), 663–673 (2009).
66. Villeneuve, N. F. et al. Nrf2 and p21 regulate the fine balance between life and death by controlling ROS levels. *Cell. Cycle.* **8** (20), 3255–3256 (2009).
67. Ryter, S. W. & Tyrrell, R. M. The heme synthesis and degradation pathways: role in oxidant sensitivity. Heme oxygenase has both pro- and antioxidant properties. *Free Radic Biol. Med.* **28** (2), 289–309 (2000).
68. Ryter, S. W., Alam, J. & Choi, A. M. Heme oxygenase-1/carbon monoxide: from basic science to therapeutic applications. *Physiol. Rev.* **86** (2), 583–650 (2006).
69. Smith, K. A., Waypa, G. B. & Schumacker, P. T. Redox signaling during hypoxia in mammalian cells. *Redox Biol.* **13**, 228–234 (2017).
70. Paradkar, P. N. et al. Regulation of mitochondrial Iron import through Differential turnover of Mitoferrin 1 and Mitoferrin 2. *Mol. Cell. Biol.* **29** (4), 1007–1016 (2009).
71. Crooks, D. R. et al. Posttranslational stability of the heme biosynthetic enzyme ferrochelatase is dependent on iron availability and intact iron-sulfur cluster assembly machinery. *Blood.* **115** (4), 860–869 (2010).
72. Malarz, K. et al. The Landscape of the Anti-kinase activity of the IDH1 inhibitors. *Cancers (Basel).* **12** (3), 536 (2020).
73. Lee, S. M. et al. Cytosolic NADP+-dependent isocitrate dehydrogenase status modulates oxidative damage to cells. *Free Radic. Biol. Med.* **32** (11), 1185–1196 (2002).
74. Kim, S. Y. et al. Regulation of singlet oxygen-induced apoptosis by cytosolic NADP+-dependent isocitrate dehydrogenase. *Mol. Cell. Biochem.* **302** (1–2), 27–34 (2007).
75. Dhar, R. et al. Proteolytic cleavage of p70 ribosomal S6 kinase by Caspase-3 during DNA damage-Induced apoptosis. *Biochemistry.* **48** (7), 1474–1480 (2009).
76. Lamparska-Przybysz, M., Gajkowska, B. & Motyl, T. BID-Deficient breast Cancer MCF-7 cells as a model for the study of Autophagy in Cancer Therapy. *Autophagy.* **2** (1), 47–48 (2006).

Acknowledgements

The study was supported by National Science Centre grants 2019/35/B/NZ5/04208 (KM) and 2020/39/O/NZ5/02342 (AMW, PZ). We thank our colleague Dr. Maciej Serda for his help in analyzing the MS spectra.

Author contributions

KM designed experiments, performed cytotoxicity, cell cycle, analysed data and wrote the manuscript; PZ performed cytotoxicity with metal ions, apoptosis, and immunoblotting assays; DZ planned and performed the chemical syntheses; PR conducted ROS, cytotoxicity with the antioxidant and qRT-PCR assays; AMW created research hypothesis, discussed the results and wrote the manuscript. All of the authors read and approved the

final version of the manuscript.

Declarations

Competing interests
The authors declare no competing interests.

Additional information
Supplementary Information The online version contains supplementary material available at https://doi.org/10.1038/s41598-024-77575-4.

Correspondence and requests for materials should be addressed to A.M.-W.

Reprints and permissions information is available at www.nature.com/reprints.

Publisher's note Springer Nature remains neutral with regard to jurisdictional claims in published maps and institutional affiliations.

Open Access This article is licensed under a Creative Commons Attribution-NonCommercial-NoDerivatives 4.0 International License, which permits any non-commercial use, sharing, distribution and reproduction in any medium or format, as long as you give appropriate credit to the original author(s) and the source, provide a link to the Creative Commons licence, and indicate if you modified the licensed material. You do not have permission under this licence to share adapted material derived from this article or parts of it. The images or other third party material in this article are included in the article's Creative Commons licence, unless indicated otherwise in a credit line to the material. If material is not included in the article's Creative Commons licence and your intended use is not permitted by statutory regulation or exceeds the permitted use, you will need to obtain permission directly from the copyright holder. To view a copy of this licence, visit http://creativecommons.org/licenses/by-nc-nd/4.0/.

© The Author(s) 2024

4.2. [P2]. The multifaceted mechanism of action of quinoline thiosemicarbazone based on disruption of iron homeostasis and selective IGF1R inhibition leading to oxidative stress induction

Autorzy: Zioła P., Malarz K., Rawicka P., Korzec M., Serda M., Boguszewska-Czubara A., Pacholczyk M., Książek M., Mrozek-Wilczkiewicz A.

Referencja: *Biomedicine & Pharmacotherapy*, 2025, **192**, 118692

Numer DOI: 10.1016/j.biopha.2025.118692

Impact Factor czasopisma: 7.5 (2024)

Liczba punktów MNiSW czasopisma: 100 (2026)

Mój udział w pracy polegał na wykonaniu wszystkich badań biologicznych oraz badań chelatacji, analizie wyników badań oraz pisaniu manuskryptu.

Biomedicine & Pharmacotherapy 192 (2025) 118692

Contents lists available at ScienceDirect

Biomedicine & Pharmacotherapy

journal homepage: www.elsevier.com/locate/biopha

The multifaceted mechanism of action of quinoline thiosemicarbazone based on disruption of iron homeostasis and selective IGF1R inhibition leading to oxidative stress induction

Patryk Zioła [a], Katarzyna Malarz [a], Patrycja Rawicka [a], Mateusz Korzec [c], Maciej Serda [c], Anna Boguszewska-Czubara [d], Marcin Pacholczyk [b], Maria Książek [a], Anna Mrozek-Wilczkiewicz [a,b,*]

[a] A. Chełkowski Institute of Physics, University of Silesia in Katowice, 75 Pułku Piechoty 1a, Chorzów 41-500, Poland
[b] Department of Systems Biology and Engineering, Silesian University of Technology, Akademicka 16, Gliwice 44-100, Poland
[c] Institute of Chemistry, University of Silesia in Katowice, 75 Pułku Piechoty 1a, Chorzów 41-500, Poland
[d] Department of Medical Chemistry, Medical University of Lublin, Chodźki 4a, Lublin 20-093, Poland

ARTICLE INFO

Keywords:
Iron metabolism
Oxidative stress
Metal chelators
IGF1R inhibition

ABSTRACT

In the present study, we introduce thiosemicarbazone derivatives with high antiproliferative activity against glioblastoma cells and high selectivity against healthy cells. The cellular studies were performed on a 3D spheroid model, which more closely reflects the conditions of an actual tumor. The tested thiosemicarbazone derivatives form complexes with iron ions, triggering the generation of reactive oxygen species, leading to cell death. The multitarget mechanism of action manifests through inhibition of the insulin receptor and the impact on iron metabolism and the disruption in redox homeostasis inducing oxidative stress in the cell. An additional advantage of the tested thiosemicarbazone derivatives is their ability to pass through the blood-brain barrier, which is crucial in the case of brain tumors. The effectiveness of the therapy was confirmed in a fish *in vivo* model, in which a reduction in tumor size in xerographs was recorded while maintaining minimal toxicity on a Zebrafish model. These results render the studied compounds attractive as potential drugs for therapy against glioblastoma.

1. Introduction

Thiosemicarbazones (TSCs) are a group of compounds known for their various medicinal applications. Among others, TSC derivatives exhibit antimicrobial [1,2], anticancer [3,4], and antifungal [5,6] activities through specific molecular mechanisms. One of the first well-understood mechanisms of action of TSCs was their inhibition of ribonucleotide reductase (RR) [7,8], an iron-dependent enzyme providing deoxynucleotide triphosphates for DNA synthesis and repair. The most fundamental property of the aforementioned compounds is through transition metal ion chelation, notably iron, copper, and zinc. In biological systems, an ion bound to a ligand becomes less bioavailable to cells than a free ion, which can lead to microelemental deficiencies resulting in the inhibition of proliferation [9]. This phenomenon contributes to a degree of selectivity during treatment, since transformed cells possess higher metabolic rates compared to their healthy counterparts. The relation of TSCs with iron is exceptionally interesting due to its ability to generate reactive oxygen species (ROS) in redox reactions, such as Fenton and Haber-Weiss reactions [10]. Iron ions cycle between Fe^{2+} and Fe^{3+} states with the side product in the form of a hydroxyl radical – the strongest known ROS. During chelation by a ligand, the iron atom may lose its redox activity depending on the type of ligand [11,12]. However, TSC complexes often allow iron to maintain its ability to participate in enzymatically promoted redox reactions [13]. A mechanism of action connected with the phenomenon of metal chelation relies on overloading cancer cells with metal ions, disrupting homeostasis and causing cytotoxic effects, such as excess generation of ROS leading to oxidative stress. Compounds possessing such ability are called ionophores. Recent experiments have shown a significant increase in cytotoxicity during treatment with specific TSCs after the addition of copper and iron ions, which indicates that this group of ligands can also participate in ion transport inside cells [14,15],

* Corresponding author at: A. Chełkowski Institute of Physics, University of Silesia in Katowice, 75 Pułku Piechoty 1a, Chorzów 41-500, Poland.
E-mail address: anna.mrozek-wilczkiewicz@us.edu.pl (A. Mrozek-Wilczkiewicz).

https://doi.org/10.1016/j.biopha.2025.118692
Received 9 June 2025; Received in revised form 13 October 2025; Accepted 21 October 2025
Available online 28 October 2025
0753-3322/© 2025 The Authors. Published by Elsevier Masson SAS. This is an open access article under the CC BY license (http://creativecommons.org/licenses/by/4.0/).

Therefore, TSC derivatives have the unique property of forming complexes with iron, disrupting its cellular homeostasis while simultaneously affecting the antioxidant systems in the cell. Increased levels of ROS can affect antioxidative defense mechanisms, including glutathione peroxidase 4 (GPX4), which uses glutathione (GSH). GPX4 expression and activity are regulated by selenium and GSH, and its function declines without these substrates. GSH synthesis relies on the cystine/glutamate transporter SLC7A11 (xCT system). Disruption of cystine and glutamate levels causes a depletion of GSH. The SLC7A11 antiporter consists of a light subunit xCT and a heavy subunit 4F2hc, the latter being an important protein in other regulatory pathways [16].

The impact of TSCs on the metal ions metabolism, in particular iron, is important because of their involvement in many key cellular processes. Iron is located in the catalytic functional domain of many enzymes, participating in multiple metabolic reactions. Changes in the labile iron pool (LIP) caused by small-molecule iron chelators trigger multiple cellular pathways aimed at restoring normal homeostasis [17, 18]. Due to the hypermetabolic requirements of glioblastoma multiforme (GBM), a particularly aggressive and deadly brain tumor, this type of tumor is strongly dependent on iron [19]. Patients suffering from GBM have a poor prognosis mainly due to the heterogeneity of the tumor, the presence of glioblastoma stem cells, the occurrence of mutations in the epidermal growth factor receptor (EGFR), the most prevalent being *EGFRvIII* [20], difficulty in drug delivery caused by the presence of the blood-brain barrier (BBB), and its immunosuppressive microenvironment [21]. The heterogenic nature of GBM and neoplasms, in general, is one of the main reasons resulting in difficulties during treatment. One of the cell subpopulations especially responsible for their resistance is glioblastoma stem cells (GSCs), possessing high self-renewal capacity and increased growth rate comparable to embryonic stem cells present naturally in the human body [22]. GSCs are regulated by many signaling pathways, with the IGF/IGF1R pathway being considered particularly important in various types of cancer. Therefore, in the current study, we present the use of TSC derivatives in GBM therapy, with a particular focus on their ability to inhibit tyrosine kinases and pass through the BBB.

2. Results and discussion

2.1. Cytotoxicity studies

In the present study, we have collated the most active derivatives synthesized over the years in our team (Fig. 1). In an earlier work, the structure-activity relationship was performed to select the molecular fragments responsible for the antiproliferative activity [14,23–25]. Besides the quinoline fragment, the key pharmacophore is the TSC moiety manages the chelating properties. The formation of complexes with metals generates ROS, which disrupts the cellular redox balance. In our study, we focused on the GBM model represented by two systems - 2D and 3D. We selected four GBM cell lines for the study; U-251, T98G, LN-18, and LN-229. The

results presented in Tables 1 and 2 show a high activity for all the derivatives tested. To determine the selectivity of the derivatives tested, we compared the calculated IC_{50} values for the cancer cell lines with the IC_{50} values for normal fibroblast-type NHDF cell line. For the 2D model (Table 1), the cell lines most sensitive to inhibition of their proliferation by the tested compounds were U-251 and LN-229. The IC_{50} values determined for the U-251 cell line ranged from 0.003 μM (MS168) to 0.489 μM (MS179), while for the LN-229 cell line, from 0.021 μM (MS168) to 0.395 μM (MS179). In the case of the LN-18 cell line, IC_{50} values ranged from 0.103 μM (MS168) to 3.76 μM (MR5K3). The T98G cell line was the most resistant, in the 2D model, to TSC derivatives, namely the lowest IC_{50} was recorded for derivative MS179, which was 6.88 μM, while the highest was above 25 μM for MS139, MS165, MR5K3, MS168, and MS181. As the most active compound, the MS168 derivative was, therefore, selected for further study, as the derivative

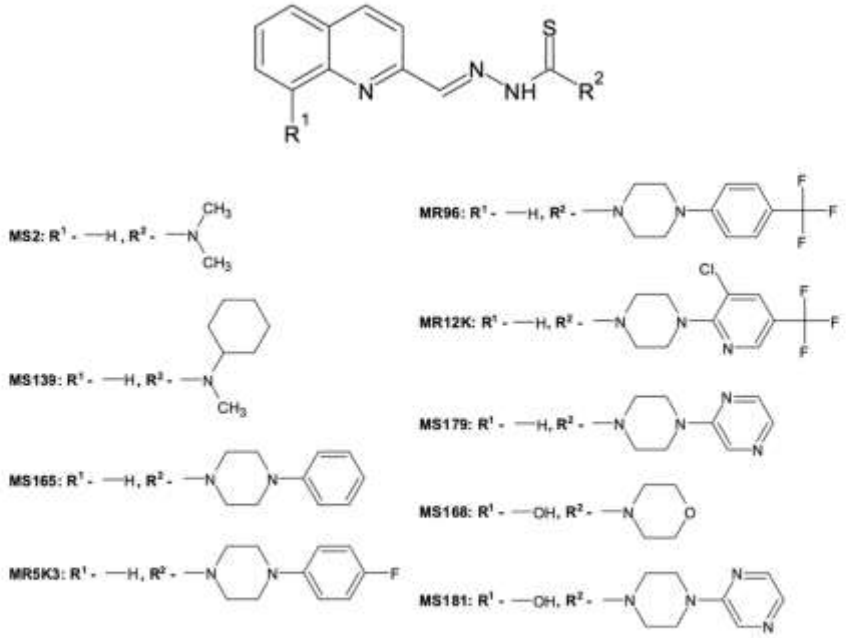

Fig. 1. Chemical structures of the studied compounds.

Table 1
Antiproliferative ability of tested TSCs on 2D model after 72-hour incubation.

Compound	IC_{50} values [μM]				
	U-251	T98G	LN-18	LN-229	NHDF*
MS2	0.040 ± 0.004	6.914 ± 1.179	0.257 ± 0.043	0.035 ± 0.008	10.58 ± 4.07
MS139	0.069 ± 0.007	> 25	0.581 ± 0.070	0.328 ± 0.044	14.49 ± 2.25
MS165	0.040 ± 0.014	> 25	1.774 ± 0.556	0.160 ± 0.015	0.033 ± 0.007
MS179	0.489 ± 0.186	6.883 ± 0.881	1.643 ± 0.243	0.395 ± 0.112	9.440 ± 3.840
MR5K3	0.104 ± 0.019	> 25	3.760 ± 0.579	0.096 ± 0.033	0.143 ± 0.021
MR96	0.091 ± 0.004	15.56 ± 1.46	0.160 ± 0.062	0.073 ± 0.014	16.66 ± 5.57
MR12K	0.341 ± 0.098	18.49 ± 0.52	11.74 ± 1.42	0.250 ± 0.068	22.34 ± 1.36
MS168	0.003 ± 0.001	> 25	0.103 ± 0.036	0.021 ± 0.004	10.64 ± 3.48
MS181	0.046 ± 0.018	> 25	9.399 ± 0.957	0.087 ± 0.009	12.14 ± 3.58
osimertinib	20.13 ± 0.34	7.314 ± 2.187	7.353 ± 0.268	8.986 ± 0.367	6.269 ± 0.375

* - data previously published in [14, 23–25]

showing the greatest versatility in inhibiting the growth of the GBM cell lines tested, and as the compound with good resistance to normal cells. In addition, we performed a crystallographic structure for this compound (Figure S1) with the calculated crystal data and hydrogen bonds (Tables S1 and S2). The tests performed on the 3D model (Table 2), in some cases, yielded interesting, unexpected results. Formed from cells, a spherical spheroid suspended in a medium more closely mirrors the conditions of a real tumor. In this 3D model, hypoxic conditions occurring under clinical conditions may even occur, so penetration

of the compound into a single cell may proceed differently, than in the adherent 2D monolayer model, where the cell surface is more easily accessible. Therefore, it is expected that the activity of the TSCs tested would be reduced, which was indeed found for all cell lines, except the T98G cell line. The susceptibility of this line to the TSCs tested increased significantly, where the IC_{50} parameters ranged from 0.855 μM for MR12K to > 200 μM for MS168. For the other cell lines, the trend was maintained, when comparing the 2D to 3D model, namely the lowest IC_{50} values were recorded for cell line U-251; from 0.333 μM for MR96 to 64.840 μM for MS168 and for LN-229; from 0.790 μM for MR96 to 19.93 μM for MS181. Interestingly, MS168 and MS181 derivatives containing a hydroxyl group as a substituent in the quinoline ring in the 3D model lost their activity. This may be linked to a change in lipophilicity, mediated by the hydroxyl group, which in turn affects cellular transport mechanisms. Furthermore, the analysis of the chelating properties of the tested TSCs, presented below, may explain this loss of activity. The derivatives containing the hydroxyl group are the only ones in the selected group to form a complex with Fe^{3+} in a 1:1 ratio.

2.2. Spectroscopic studies

To determine whether the studied compounds form complexes with Fe^{3+} ions, spectroscopic measurements were conducted. Initially, the absorption spectra of TSC alone, dissolved in DMSO at a concentration of 50 μM, were recorded (Fig. 2). Subsequently, increasing concentrations of metal ions were gradually added, and after an incubation period, the absorption spectra were recorded again. The graphs show that most tested TSCs exhibit an absorption band maximum of around 340 nm (Fig. 2**A–G**). Exceptions include MS168 and MS181 (Fig. 2**H** and **I**), which display a maximum absorption at 305 nm. With the addition of increasing concentrations of iron ions, a gradual decrease in absorbance is observed at the wavelength corresponding to the absorption maximum of TSCs (blue arrow). Additionally, after adding iron ions to the TSC solution, a new band appears at around 430 nm, with its absorbance increasing as the concentration of added ions rises (red arrow). In the recorded spectra, an isosbestic point is visible around 375 nm, indicating that the studied TSCs exist in at least two forms: free and metal-bound. In the case of MS168 and MS181, two isosbestic points were observed. The point located at shorter wavelengths may be related to the transition from the ground electronic level to the excited electronic state of the TSC in the presence of the metal, whereas the point at longer wavelengths indicates a charge transfer mechanism between the ligand and the metal ion [26]. It is also worth mentioning that for both of these compounds, hidden isosbestic points (HIP) were observed, meaning that the isosbestic points became visible only after normalizing the obtained spectra. HIP indicates a more complex binding mechanism involving multiple equilibrium states, gradual complex formation, and charge transfer interactions rather than a simple, one-step coordination of the ligand with the metal ion [27].

To determine the stoichiometry of metal ion binding for a given TSC, a curve was plotted to illustrate the change in absorbance at the complex band as a function of the molar ratio of metal to ligand. The resulting curves are presented in Fig. 3, highlighting the molar ratio at which the threshold concentration of iron ions is sufficient to bind the ligand at the given concentration. Most tested compounds exhibit a 2:1 (L:M) stoichiometry, except for MS168 and MS181, which have a 1:1 stoichiometry. Similar studies confirming the ability of the tested compounds to bind iron ions were presented in our recent work on the impact of iron chelators on the effectiveness of photodynamic therapy [28]. Using absorption spectroscopy measurements, it was demonstrated that in the presence of iron ions, the band corresponding to the free compound disappears, while a new band appears, corresponding to the formed iron-ligand complex. The presence of the compound in two forms (metal-bound and free) is also evidenced by the isosbestic point visible in the spectra.

2.3. Generation of reactive oxygen species

The formation of complexes with iron allows TSC derivatives to participate in ROS formation. The ability of TSC derivatives to generate ROS was proven more than once, not only by our team [14,25] but by many others [29–31]. It is well known that metal ions such as iron or copper are involved in the Fenton and Haber-Weiss reactions, in which free radicals are formed [32,33]. One of these is the hydroxyl radical – the most powerful oxidant. The participation of metal ions in radical reactions involves electron transfer, which is made possible by the existence of different oxidation states (Fe^{2+}/Fe^{3+}) that are structurally very similar. The binding of the metal ion in the form of a complex by the TSCs still allows participation in redox reactions due to the lack of involvement of the coordination sphere in this process [18]. The potential to participate in redox reactions determines the biological activity of TSC complexes. A direct consequence is the inhibition of RR activity [34]. After performing kinetic experiments using a fluorescent ROS detection sonde, it is concluded that the four selected TSC representatives increased their levels in the 3D cellular model. As can be seen in Fig. 4**A**, the longer the incubation time, the higher the ROS concentration, reaching up to 126 % after 24 h. In addition, imaging of the tested spheroids was performed. As shown in Fig. 4**B**, a strong green CellROX signal indicates a high concentration of ROS in cells exposed to the tested TSCs. Brighter spots are visible in the outer layer of the

Table 2
Antiproliferative ability of tested TSCs on 3D model after 72-hour incubation and their lipophilicity index.

Compound	IC_{50} values [μM]				Lipophilicity index (logP)
	U-251	T98G	LN-18	LN-229	
MS2	0.905 ± 0.215	31.33 ± 5.14	0.908 ± 0.200		2.535 ± 0.965
MS139	0.738 ± 0.108	4.355 ± 0.883	5.162 ± 0.988		1.542 ± 0.405
MS165	2.472 ± 0.716	2.922 ± 0.221	1.027 ± 0.235		2.974 ± 0.987
MS179	4.175 ± 0.930	4.138 ± 1.236	4.151 ± 0.539		22.49 ± 3.91
MR5K3	0.691 ± 0.197	1.507 ± 0.610	1.292 ± 0.316		2.927 ± 0.974
MR96	0.133 ± 0.058	7.170 ± 1.217	7.053 ± 1.091		0.790 ± 0.210
MR12K	8.178 ± 1.270	0.855 ± 0.208	7.664 ± 1.624		7.721 ± 1.794
MS168	64.84 ± 8.98	> 200	177.4 ± 4.6		17.58 ± 3.01
MS181	45.07 ± 6.97	65.13 ± 11.13	28.76 ± 6.47		19.93 ± 2.76
osimertinib	29.98 ± 6.53	29.75 ± 5.05	45.06 ± 5.22		41. ± 4.31

spheroids, further supporting the pro-ROS-inducing properties of all the compounds, with MS168 generating the strongest signal. An increase in signal strength seen in a spheroid treated with the studied TSCs correlates with the increased ROS levels, resulting in the disruption of cellular redox homeostasis. The cellular imbalance affects a number of key processes, so in the following studies, we focused on elucidating the detailed mechanism of action of the TSCs studied.

2.4. Effect on kinase activity inhibition

After initial screening of the cytotoxicity of the investigated TSCs on a panel of glioblastoma cell lines, in a further step, we proceeded to further analysis to verify whether selected tyrosine kinase inhibition has a significant effect on high antiproliferative activity of TSCs. In glioblastoma, many important signaling pathways regulating cell metabolism, growth, proliferation, and metastasis are initiated by a signal received by receptor tyrosine kinases such as EGFR and IGF1R. Therefore, the effect of all tested compounds at a concentration of 1 μM on the receptor tyrosine kinase activity was examined. Profiling was performed using the available Kinase Selectivity TK-1 systems containing eight tyrosine kinases such as IGF1R, InsR, EGFR, HER2, HER4, KDR, PDGFRa, and PDGFRb. As presented in Fig. 5, the TSCs had a rather weak interaction with the tested receptors, with the exception of the insulin-like receptor (IGF1R). In fact, two of them, MS168 and MR5K3, exhibited a strong ability to inhibit IGF1R activity. The MS168 derivative inhibited insulin kinase activity by more than 65 %, while MR5K3 reduced its activity by almost 62 %. A slightly lower level of IGF1R kinase inhibition was recorded for the reference compound osimertinib (57 %) however, no statistical significance was demonstrated. In the case of EGFR kinase, only osimertinib, a 3rd generation inhibitor, was confirmed to have a high inhibitory capacity. In contrast, for most of the tested TSCs, the inhibition potential did not exceed 25 %. Only the MS139 and MR96 derivatives inhibited EGFR kinase activity by almost 38 %. Similar results were obtained for the other receptor kinases, for which the observed inhibition potency did not exceed 40 % after the administration of the tested TSCs. As part of screening through the most popular kinases the effect of TSCs on non-receptor kinase activities was also investigated, and the results are shown in Figure S2. Unfortunately, none of the compounds showed significant inhibitory potential therefore results have been omitted. These results indicate that the high activity of the compounds studied is the result of their multifaceted mechanism of action not only inhibition of tyrosine kinases. Compounds for which the inhibition percentage exceeded 50 % were subject to further experiments focused on determining the dissociation constant (K_D) that specifies the exact affinity and binding strength between the ligands MS168 and MR5K3 and the IGF1R protein.

2.5. Binding affinity to the IGF1R receptor

The experiments determining the binding affinity of MS168 and MR5K3 to the IGF1R protein were conducted using the microscale thermophoresis technique (MST). Serial dilutions of the TSC concentrations made it possible to detect the fraction bound and unbound to the fluorescently labeled IGF1R protein. Moreover, the analysis of binding curves generated in MST experiments provided information about the potency of the interaction of TSCs with the insulin receptor. As depicted in Fig. 6, the calculated K_D values based on MST traces were 720 nM for MS168 and 907 nM for MR5K3. Thus, the obtained results confirmed the high and selective ability of the two TSCs based on a quinoline scaffold to inhibit the insulin receptor.

2.6. Molecular docking

To evaluate the structural details of the inhibitory activity of MS168 and MR5K3 against IGF1R kinase, docking studies were performed. We targeted the compounds for an orthosteric kinase ATP binding pocket

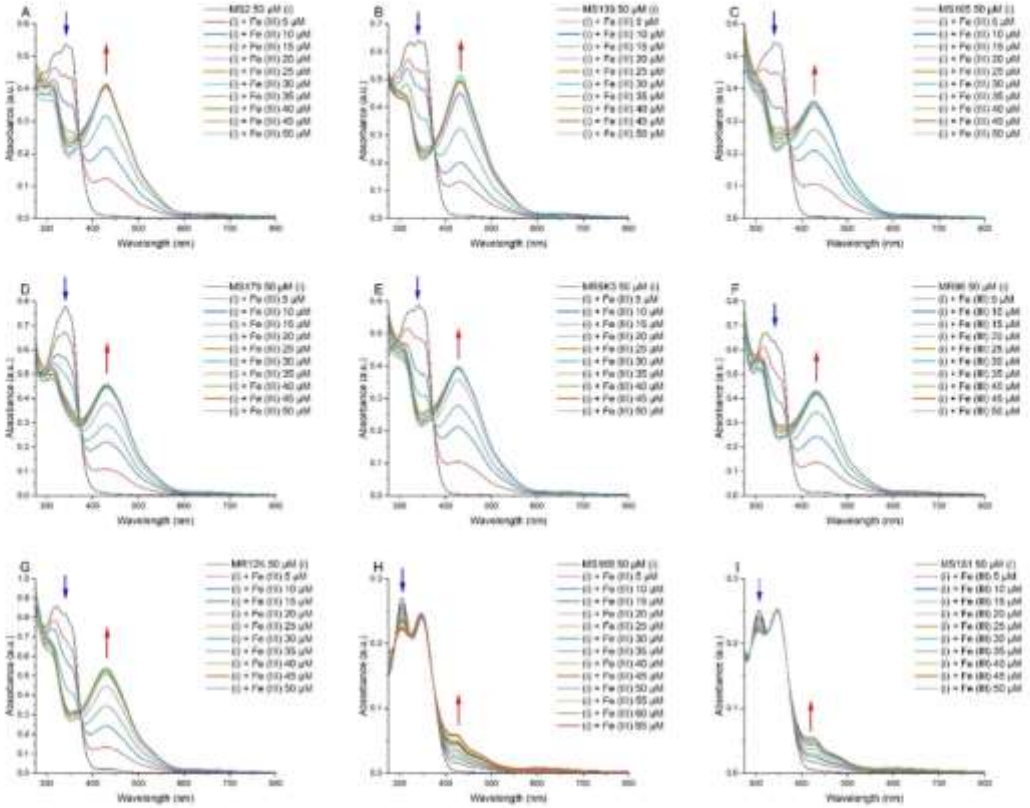

Fig. 2. Absorption spectra of the studied TSCs (50 μM) in DMSO, with and without titration of Fe^{3+} ions. The blue arrow signifies a decrease in absorbance in the compound band, while the red arrow represents an increase in the complex band.

given the quinoline scaffold. From several available structures crystalized with small molecule inhibitors, we selected a structure in IGF1R active phosphorylated conformation with activation loop extended (PDB ID: 2ZM3) originally co-crystalized with an isoquinolinedione inhibitor. Schrodinger's Induced Fit Docking (IFD) protocol, which allows for a certain extent of amino acid sidechain and protein backbone adaptations upon docking, resulted in the molecule configurations depicted in Fig. 7.

MR5K3 binds in a U-shaped conformation with fluorobenzene extended to solvent. Its quinoline forms typical hydrogen bonds with the kinase hinge region (connecting N and C lobes) previously reported, e.g., for pyrimidine inhibitors [35]. Met1082 donates backbone Cα-H to pyridine nitrogen and carbonyl of the Glu1080 and accepts TSC N-H. In contrast, MS168, most likely due to hydroxy substituent in position 8 of quinoline, binds in extended conformation with its core shifted towards the back of the active site and TSC moiety flipped to the front of the pocket, which results in a lack of interaction with Met1082. This arrangement results in three hydrogen bonds. Arg1003 (β1) donates the sidechain N-H to morpholine oxygen, carbonyl of the Leu1005 (β1) accepts TSC N-H, and carbonyl of the Glu1080 accepts hydroxyquinoline O-H.

The results of these studies confirm that the presence of a hydroxyl group in the quinoline ring significantly affects the activity of TSC derivatives. This is relevant both in the context of forming complexes with metal ions but also in the context of direct interaction with proteins.

2.7. Induction of apoptosis

Annexin V staining is one of the simplest and the most widely used methods for detecting apoptosis. The Annexin V dye specifically binds to phosphatidylserine, a structural phospholipid of the cell membrane. In healthy cells, phosphatidylserine is primarily localized to the inner leaflet of the membrane, making it inaccessible to Annexin V. During the early stages of apoptosis, the cell membrane undergoes structural changes. One of the key features of this process is the translocation of phosphatidylserine to the outer leaflet of the membrane, allowing Annexin V to bind. To distinguish early apoptotic cells from late apoptotic and necrotic cells, a secondary staining step is often included in the procedure, typically using propidium iodide or 7-AAD. These dyes bind to DNA but cannot permeate intact cell membranes. As a result, healthy and early apoptotic cells remain unstained, whereas late apoptotic and necrotic cells, which have compromised membranes, permit dye entry and become fluorescently labeled.

The data presented in Fig. 8 illustrate the proportions of live, early apoptotic, late apoptotic, and dead cell subpopulations in samples incubated with the tested compounds at up to two different concentrations: MS168, MS179, MR5K3, MS165, and osimertinib, which serves as a positive control. The analysis reveals a clear and significant increase in the apoptotic fraction in response to each compound. Notably, the proportion of live cells in the treated samples decreased from 65 % in the

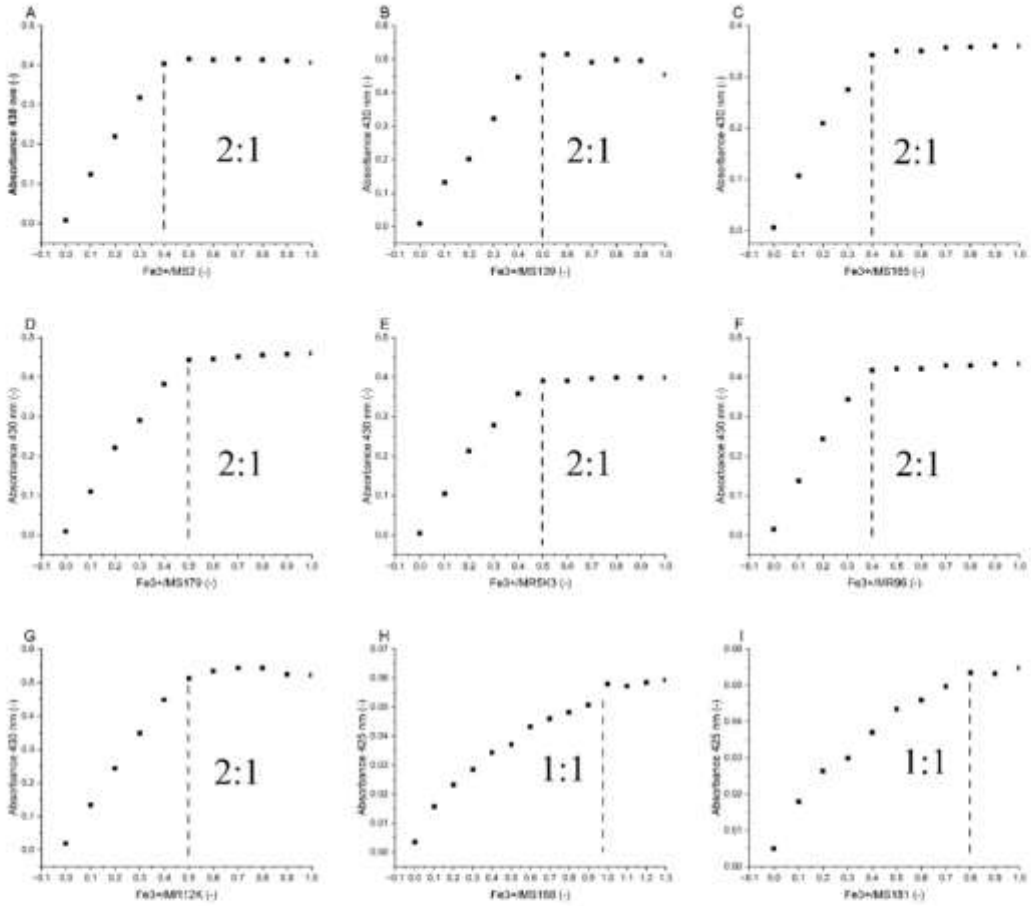

Fig. 3. The molar ratio of Fe^{3+} metal ions to the studied compounds at a concentration of 50 μM dissolved in DMSO. The inflection point marked on the graphs determines the stoichiometry of iron ion binding with the given TSC.

control group to between 8 % and 43 %, depending on the specific compound and its dosage. This reduction in viable cells was accompanied by a corresponding rise in the apoptotic subpopulation, supporting the compound's ability to induce cell death. The proportion of total apoptotic cells after incubation with TSCs increased significantly in all samples compared to the control group (35 %). The most modest effect was observed with MR5K3, where apoptosis was detected in 55 % of cells at 1 μM and 62 % at 2 μM. Notably, the increase was primarily in the early apoptotic subpopulation, while late apoptotic cell counts remained comparable between doses. Similar results were obtained for MS179, with apoptosis rates of 59 % at 5 μM and 64 % at 10 μM. However, in this case, the higher concentration resulted in a greater presence of late apoptotic cells. MS165 was the second most effective compound, inducing apoptosis in 69 % of cells at 2.5 μM and 64 % at 5 μM, with a consistent proportion of early and late apoptotic subpopulations across both doses. The most potent TSC was MS168, which induced apoptosis in 75 % of cells. This effect was most comparable to osimertinib, which caused apoptosis in 86 % and 92 % of cells at the tested concentrations. These results highlight the potent apoptotic effects of all the selected compounds on U-251 cells, demonstrating their capacity to significantly promote apoptosis at various concentrations.

2.8. Immunoblotting

The results presented here, based on previous research, are indicative of a direct connection between the complexing properties of the TSCs tested and the generation of oxidative stress in the cell [14,36]. Additionally, for the selected TSC derivatives IGF1R inhibition contributes to the suppression of proliferation in the cell lines studied and explaining the potential mechanism of action. The purpose of further studies was to suggests a potential association between the formation of metal complexes, by influencing iron metabolism and inhibition of IGF1R. However, even at this stage of research, it can be concluded that it is impossible to establish a clear connection for all compounds, as they exhibit diverse behavior. Previous data on the impact of other TSC derivatives on iron metabolism prompted us to investigate the effect of the compounds studied in this work on iron-dependent proteins. Proteins involved in the antioxidant defence of cells and in processes related to

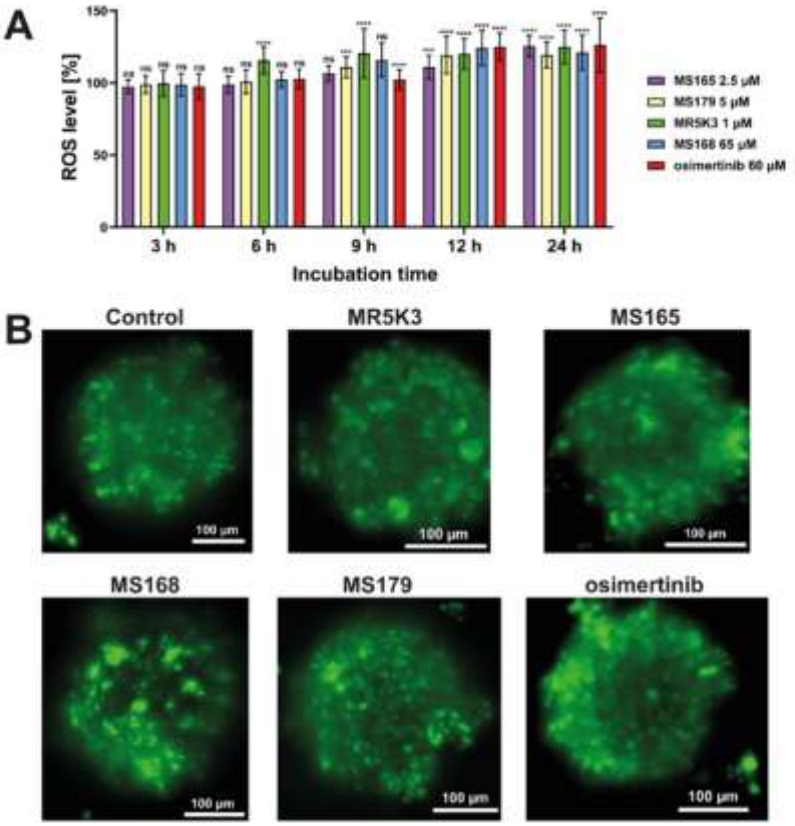

Fig. 4. **(A)** Changes in ROS levels in the U-251 cell line after 3–24 h of exposure to tested TSCs, measured by a CellROX® Green Reagent assay. Data were normalized to the untreated control group and are presented as the mean ± SD (n = 3). Statistical analysis was performed using a one-way ANOVA followed by Bonferroni's post hoc test. Results were shown in the form of asterisks: *p < 0.05, **p < 0.01, ***p < 0.001, ****p < 0.0001 compared to control (untreated cells). Three independent experiments were performed, with each measurement carried out in duplicate. **(B)** Representative images of the CellROX® Green Reagent fluorescence staining of U-251 spheroids after 24 h of incubation with tested TSCs in their respective IC_{50} concentrations. Scale bars represent a length of 100 μm.

the induction of oxidative stress were also examined. In addition, we examined targets associated with IGF1R receptor pathway to confirm whether its inhibition, demonstrated for some derivatives, affects cellular mechanisms. For this purpose, the WB technique was used (Fig. 9). Densitometric analysis for the presented membranes is shown in Figure S3.

The first target tested was a popular indicator of disruption of the redox equilibrium toward oxidation processes. The occurrence of heme oxygenase 1 (HO-1) overexpression can undoubtedly be linked to elevated ROS concentrations [37]. HO-1 overexpression was present for all compounds tested, including the reference, with the greatest increase observed for MS168 (more than 12-fold). An increase of more than 7-fold was observed for MS179. The lowest, but still significant increase (more than 2-fold) was registered for MR5K3. The results correlate with those obtained for the antioxidant molecule GPX4, where the greatest decrease in its expression was recorded for MS168 (0.3 relative to control) and the least for MR5K3 (no inhibition). The differences in the antioxidant cellular response of these two derivatives prove that subtle changes in chemical structure, not only in the thiosemicarbazone group but also in the quinoline ring substitution, have a significant impact on their mechanism of action. GPX4 participates in protecting cells from lipid peroxidation and is one of the main indicators of ferroptosis [38]. For the other compounds, MS179 and MS165, the decrease in GPX4 was at a level of about 0.6. The explanation for these results may be that an increase in ROS levels activates the cell's antioxidant systems, and therefore, the level of antioxidants consumed to deactivate ROS decreases [39]. Oxidative stress can also be caused by a disruption in the transport of substrates for the synthesis of the most important antioxidant, glutathione. Glutamate and cystine are transported across the cell membrane via xCT system, an essential part of which is a heavy subunit 4F2hc. The largest decrease in 4F2hc was recorded for MS165 (0.5). For compounds MS168 and MR5K3, the decrease in 4F2hc was at a similar level (0.8). MS179 did not cause inhibition of this protein.

TSC derivatives, by forming chelates with iron, affect iron metabolism, as demonstrated in our earlier work [40]. Iron-regulatory proteins (IRPs) are the first responders to iron deficiency [41]. In this study, we measured the levels of IRP1 and IRP2 and concluded that the tested compounds significantly affect the activation of both proteins. In the case of IRP1, the largest (almost 2-fold) increase was registered for MS179. The other compounds increased IRP1 by about 1.5. Whereas

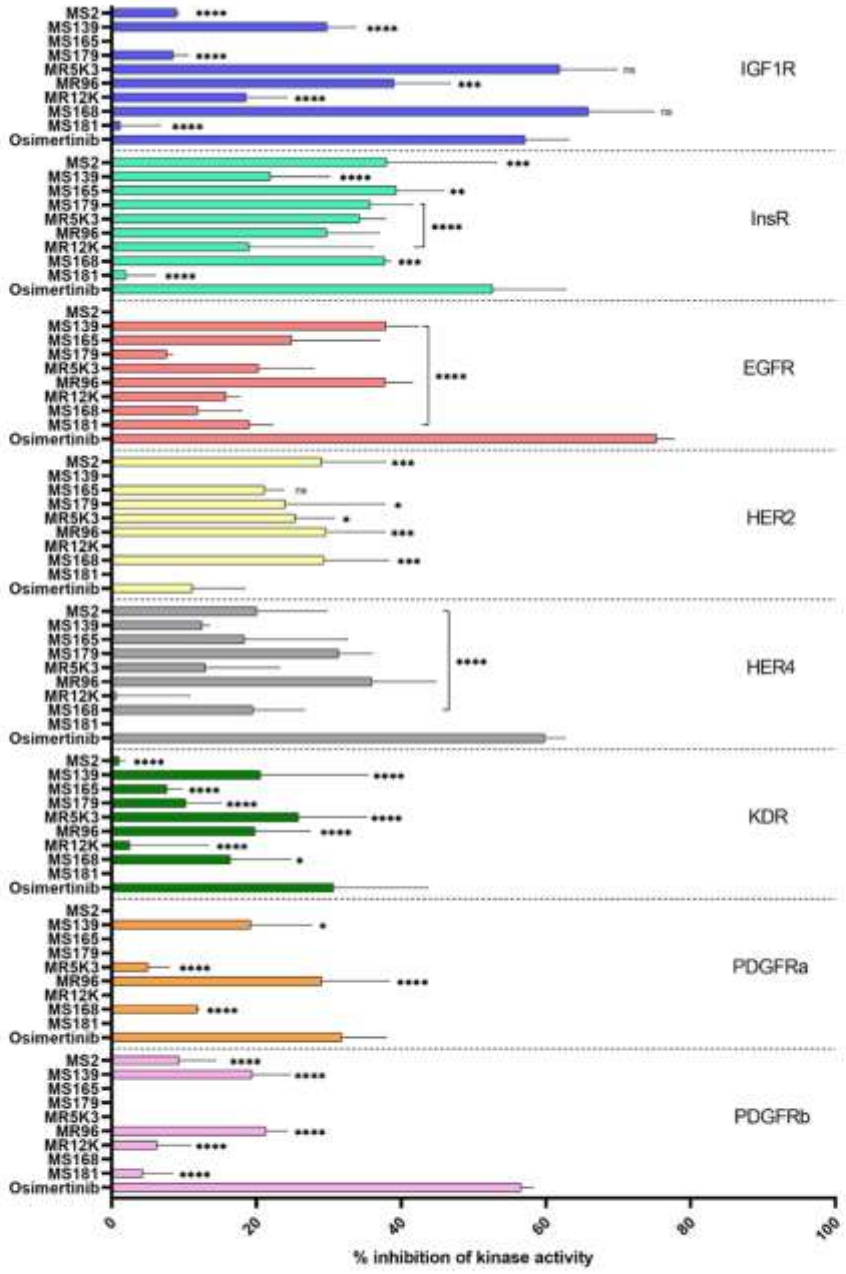

Fig. 5. Profile of receptor kinase activities after treatment with tested TSCs and osimertinib at a concentration of 1 μM. The results are presented as % inhibition of selected kinase activity from three independent experiments (mean ± SD; n = 4). Statistical analysis was performed using a two-way ANOVA followed by Dunnett's post hoc test (*p < 0.05, **p < 0.01, ***p < 0.001, ****p < 0.0001 vs. positive control – Osimertinib).

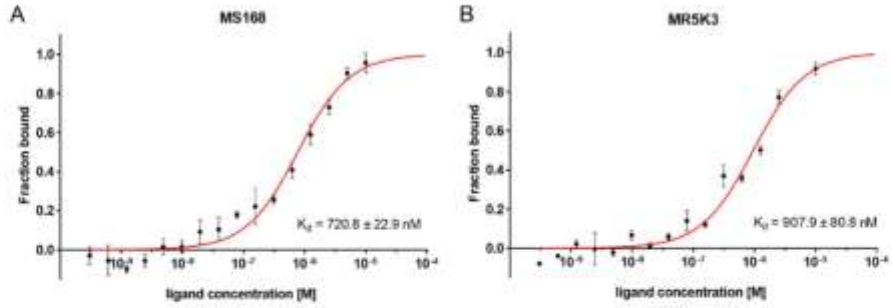

Fig. 6. Binding affinity of MS168 (A) and MR5K3 (B) derivatives to the IGF1R protein. The interactions were detected by the microscale thermophoresis technique (MST) and qualified by the value of K_D. Data are shown as the mean ± SD of three independent measurements ($n = 3$).

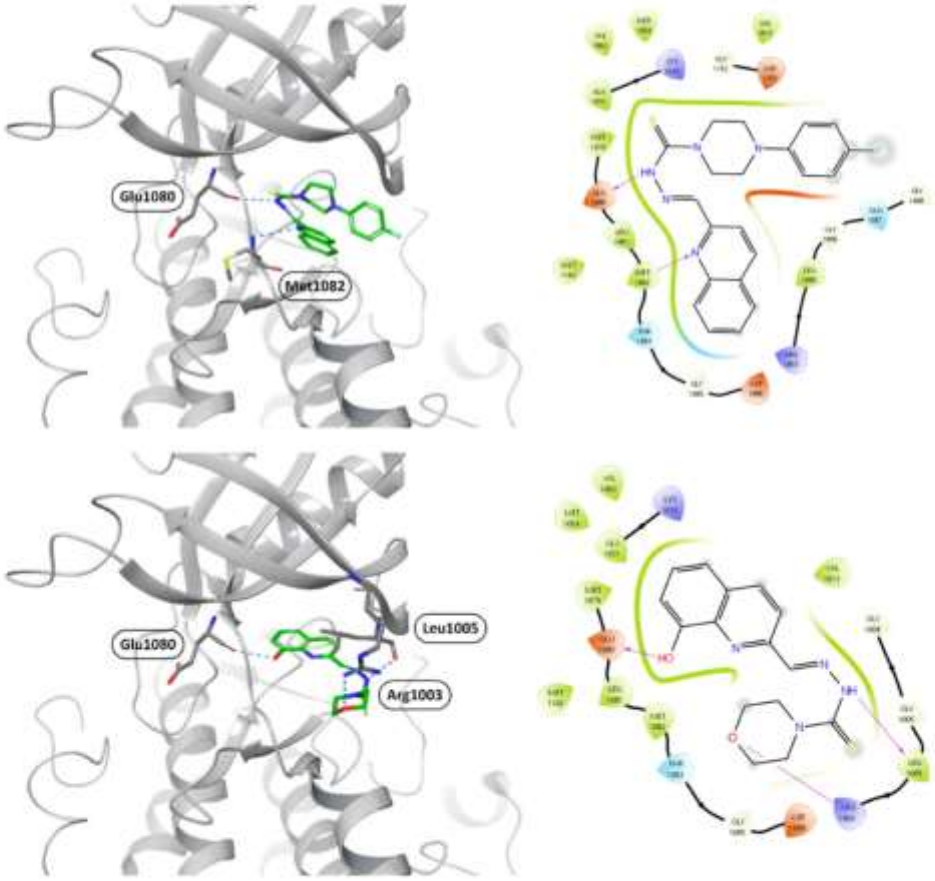

Fig. 7. The best-scored IFD docking poses of MS168 and MR5K3. Hydrogen bonds are represented by dashed cyan lines (3D) or solid magenta arrows (2D).

much greater increases were recorded for IRP2, where compound MS168 increased its concentration by as much as almost 9-fold. Subsequently, MS179 caused an increase of more than 7-fold, MS165 about 5-fold, and MR5K3 4-fold. The results indicate that the formation of complexes with iron activates systems that compensate for the deficiency of this important micronutrient aimed at maintaining proper

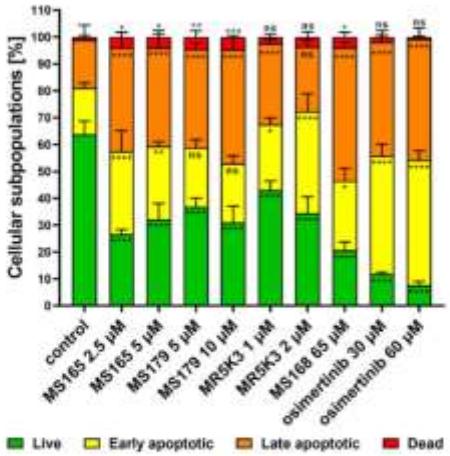

Fig. 8. Assessment of apoptosis induction in the U-251 cell line following a 48-hour treatment with the tested TSCs at IC_{50} and 2 × IC_{50} concentrations, as determined by flow cytometry. Colored bar graphs represent the proportions of live, early apoptotic, late apoptotic, and dead cells from a representative experiment. Statistical analysis was performed using a one-way ANOVA followed by Bonferroni's post hoc test (*p < 0.05, **p < 0.01, ***p < 0.001, ****p < 0.0001 vs. control – untreated cells). Three independent experiments were performed, with each measurement carried out in duplicate (n = 3).

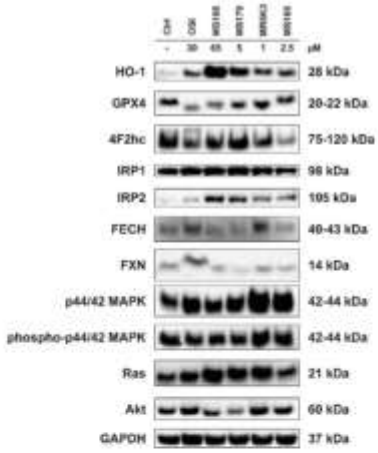

Fig. 9. Expression of selected proteins in the U-251 cancer cell line following treatment with TSCs (MS168, MS179, MR5K3, and MS165) and the reference drug osimertinib. Densitometric analysis of target proteins was normalized to the reference protein and compared to the control (Fig. S3). Data represent the mean ± SD from at least four independent experiments. The presented immunoblots were cropped from full membranes and served as representative images for the respective proteins.

homeostasis. The effect of TSCs on iron homeostasis, related to complex formation, is also manifested by effects on the expression of iron-dependent proteins such as ferrochelatase (FECH) [42]. A significant decrease in the expression of this protein was registered for compounds MS165 (0.25) and MS168 (0.7). For the MR5K3 derivative, the situation was the opposite; namely, a 1.5-fold increase in FECH expression was recorded. These results indicate that despite similarities, minor structural differences have a significant impact on the different mechanisms of action. Another analyzed iron-dependent and storage protein was frataxin (FXN) involved in the assembly of iron-sulfur clusters. The greatest decrease (0.65) in FXN expression was recorded for MS179 and MS168 (almost 0.8). The results obtained provide an interesting justification for the importance of conducting further research.

The negligible effect on EGFR receptor inhibition may be related to a lack of inhibition of the RAS/MAPK/ERK pathway-related protein cascade. It is worth mentioning that both of these proteins play key roles in the proliferation, survival, and responses to stress stimuli [43]. The WB analysis did not register a decrease in the levels of kinases that belong to the MAPK family, such as p42/44 (ERK) and RAS. This indicates that, despite the continuity of these pathways, TSC derivatives exhibit antiproliferative activity against the studied U-251 cell line, indicating their multitargeted action. In addition, the inhibition of IGF1R that was demonstrated earlier was indirectly confirmed by a decrease in Akt concentration in cases of MS168 and MS179 compounds. There are reports in the literature demonstrating a link between IGF1R inhibition and the induction of oxidative stress in cells [44,45].

2.9. Blood-brain barrier permeability assay

The ability of TSCs to generate ROS may influence the regulation of transport across the BBB [46]. As our research model is the GBM in the next step, we decided to test the passage of the selected compound across the BBB. Additionally, GBM etiology is largely related to iron disorders [47]. We, therefore, claim that our compounds are good candidates for further research into their use in GBM therapy. The BBB permeability studies indicate that a TSC derivative; MS168, has the ability to pass through the BBB better than the commercial drug temozolomide (Fig. 10). These studies were performed in a transwell model, in which the survival of cells seeded under BBB-mimicking inserts was measured. The compound MS168, which exhibits high antiproliferative activity, passed through the BBB and then influenced GBM spheroids. BBB viability was measured to confirm membrane integrity. In addition, we verified the integrity of the BBB by immunofluorescence staining for two tight junction proteins, ZO-1 and occludin, that play a crucial role in its formation. Example images can be found in Figure S4. Both tight junction proteins are clearly visible in the outer regions of connected cells. ZO-1 was localized exclusively in the cytoplasm, while occludin

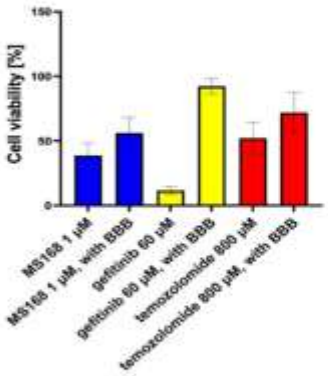

Fig. 10. Verification of blood-brain barrier permeability of tested compounds: MS168, gefitinib (negative control), and temozolomide (positive control) on transwell co-culture of hCMEC/D3 and U-251 cell lines. The results are presented as the mean ± SD from at three independent experiments (n = 3).

was also detected in the extracellular domains, confirming the expected result [48]. The results for compound MS168 are particularly interesting in that this derivative showed an effect superior to the commercially used temozolomide given at a concentration 800 times higher. The integrity of the BBB and the effectiveness of the transwell model were further confirmed by results from wells treated with gefitinib - a potent tyrosine kinase inhibitor, that is known to be incapable of crossing the BBB [49]. The presence of the barrier drastically increased the cell viability of U-251 cells, despite the high concentration (60 μM) of gefitinib used during the experiment. These results show the high potential of the selected MS168 derivative.

2.10. *In vivo* studies

The *in vivo* studies on the Zebrafish model (Fig. 11) indicated that MS168, MS181, and MS165 do not exhibit toxicity in doses of 5 mM in the FET test. The calculated LC_{50} values equal 6.772, 8.341, and 6.221 μM, respectively. When compared to the antiproliferative effects observed in LN-229 cells in a 2D *in vitro* culture, where the values were ci. 0.021, 0.087, and 0.160 μM for MS168, MS181, and MS165, respectively (Table 1), we can see a significant difference in the toxicity profile. The concentrations that show substantial effects in the cell culture model are much lower than those observed in the Danio rerio model. This suggests that, when testing *in vivo*, particularly in a xenograft model, the compounds may be administered at much higher doses than those used in *in vitro* 2D cultures, providing a unique opportunity to evaluate their therapeutic potential in a more complex biological environment.

Moreover, when compared to the results obtained for healthy NHDF cells in 2D cultures, where the antiproliferative effects were significantly higher, ci. 10.64 and 12.14 μM for MS168 and MS181 (Table 1), it becomes evident that the compounds display a much more selective action against cancerous cells. This selective anticancer effect, coupled with the significantly lower toxicity to healthy cells, suggests a potential for targeted therapeutic activity without harming normal tissue.

The results presented in Fig. 12 indicate the effects of the tested compounds on tumor size in the LN-229 xenograft model after 72 h of treatment. While none of the compounds induced a drastic tumor reduction within this short treatment window, some modest but statistically significant differences were observed at the highest tested concentration (2.5 μM) for MS168 and MS165. It is important to note that the concentrations used in the xenograft model were relatively low compared to the effective doses observed in the 3D spheroid model (Table 2). For MS168 and MS181, the effective antiproliferative concentrations in 3D cultures were 17.58 ± 3.01 μM and 19.93 ± 2.76 μM, respectively, which is substantially higher than the maximum tested *in vivo* dose of 2.5 μM. This discrepancy suggests that higher concentrations might be needed to achieve meaningful tumor reduction, but their administration was limited due to systemic toxicity in the Danio rerio model. On the other hand, for MS165, the effective concentration in 3D spheroids (2.974 ± 0.987 μM) was closer to the highest dose tested in xenografts, which may explain its observed efficacy in tumor size reduction. The observed limited tumor shrinkage could be attributed to multiple factors, including the complexity of the tumor microenvironment in xenografts, the short duration of treatment, as well as potential differences in drug distribution within the fish model. Despite these limitations, the observed reduction in tumor size for MS168 and MS165 provides encouraging perspectives for further studies on a glioblastoma mouse model.

3. Conclusion

In the present work, we introduce a multifaceted mechanism of action of TSC derivatives based on the formation of chelates with metals, including iron, with the direct consequence of ROS formation. The generation of complexes was measured by spectroscopic methods along with the determination of the stoichiometric metal-ligand ratio. Elevated concentrations of ROS in the cell disrupt redox homeostasis, leading to oxidative stress, which was confirmed in this study by independent methods.

The ability to inhibit tyrosine kinases showed the potential of the selected TSCs to inhibit insulin receptor activity, which was confirmed *in silico* by the molecular docking method and by the method of the MST. Detailed analysis of proteins involved in iron metabolism performed with the assistance of the Western Blot technique showed that the TSCs studied induce oxidative stress and have a significant effect on iron-dependent targets. The studies performed demonstrate that the tested TSCs exhibit multi-target effects depending on their chemical structure. The 3D GBM research model, allowed us to focus on aspects related to the characteristics of this cell line in the context of the effect of TSCs on iron metabolism and BBB penetration.

In addition, the research was presented on a 3D model better reflecting the actual conditions in a real tumor, which was further validated using Danio rerio xenograft models. Importantly, the *in vivo* toxicity assessment in the Danio rerio model demonstrated that despite significant antiproliferative activity against tumor cells *in vitro*, the TSCs tested do not show toxicity *in vivo*. This demonstrates the high selectivity of TSC derivatives towards normal cells. Preliminary studies on xenografts indicate a reduction in tumor size after treatment with the studied TSCs. The trend towards a reduction in tumor volume at the low doses

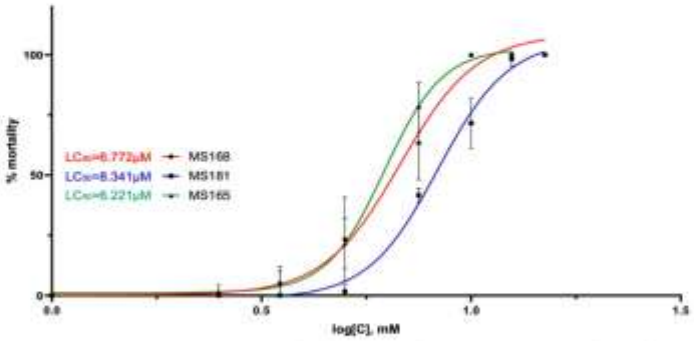

Fig. 11. *In vivo* toxicity of the 96-hour incubation with tested compounds in the FET test on the Danio rerio experimental model: MS168, MS181, and MS165. The results of the mortality rate are presented as a nonlinear fit of log-concentration vs. response (nonlinear regression). Data presented as mean ± SD from at least three independent experiments.

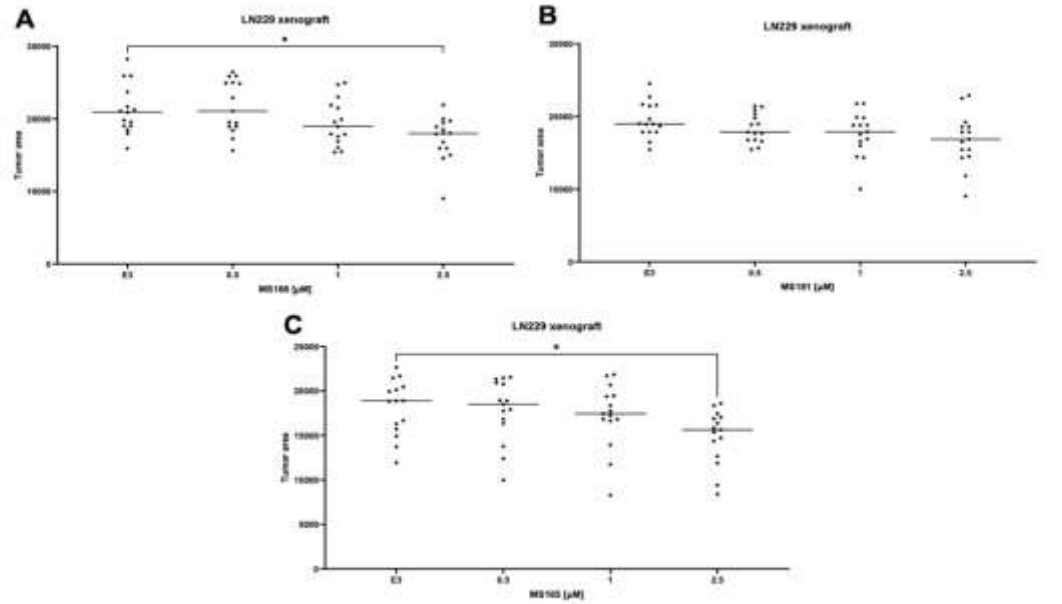

Fig. 12. Tumor area measurements for the LN-229 xenograft Danio rerio model after 72 h of incubation with three tested compounds: (**A**) MS168, (**B**) MS181, and (**C**) MS165, at three different concentrations: 0.5, 1, and 2.5 μM, compared to the untreated control group (E3). One-way ANOVA; $^{*}p < 0.05$.

used is indicative of the potential efficacy of TSCs at higher doses, as demonstrated by *in vitro* studies on a 3D model.

4. Materials and methods

4.1. Spectroscopic studies

Absorption spectra of the tested compounds and their complexes with Fe^{3+} ions were measured using a multi-plate reader (Varioskan LUX, Thermo Scientific). Spectra were recorded over 285 nm to 800 nm, with a step size of 5 nm. All measurements were performed at room temperature (RT) using a 96-well black plate with a transparent bottom (Nunc). Each well contained 200 μL of a solution comprising 50 μM of the tested compound and varying concentrations of Fe^{3+} ions. The plates were incubated for 4 h at RT before measurement. All solutions of the tested compounds and metal ions were prepared immediately in DMSO before the experiment. The obtained spectra were analyzed using OriginPro 2023 software. The stoichiometry of the complexes formed between the tested compounds (L) and Fe^{3+} ions (M) was determined using the molar ratio method. After recording the absorption spectra, plots were generated to depict the relationship between the absorbance at the maximum of the complex band and the [L]/[M] ratio.

4.2. Crystal structure determination

X-ray intensity data for MS168 were collected with graphite monochromated Mo Kα radiation at 298.0 [1] K and ω scan mode using the Xcalibur Oxford Diffraction diffractometer with Sapphire3 CCD detector. Absorption correction was applied using the multi-scan method using the CrysAlis^{Pro} software. The structure was solved by the direct method. All the non-hydrogen atoms were refined with anisotropic displacement parameters using the full-matrix, least-squares technique. All the hydrogen atoms were refined as "riding" on the adjacent carbon atom with isotropic displacement parameters equal 1.2 times (for aromatic and methylene H atoms) or 1.5 times (for hydroxyl H atoms) the value of the equivalent temperature factor of the parent atom. The SHELXS2013 and SHELXL2013 programs [50] were used for all the calculations. A brief description of the structure and the most important crystallographic data are placed in the Supplementary Information (Figure S1 and Tables S1 and S2).

4.3. Molecular docking

Docking to the IGF1R (PDB ID: 2ZM3) structure was performed using the IFD (Induced Fit Docking) protocol in the Schrodinger Suite. The structures were prepared for docking with Protein Preparation Wizard. The conformers of the ligands were created with LigPrep and Epik. The protonation states of the proteins and ligands were calculated at a pH of 7.4. The protein-ligand interactions were investigated using the protein-ligand interaction tool in Schrodinger Maestro 12. The figures showing the 3D docking configurations and interactions were also prepared with the Maestro interface.

4.4. Kinase activity inhibition

Assays using the Kinase Selectivity TK-1 and TK-2 profiling systems and ADP-Glo Kinase Assay (all from Promega) were performed to determine the inhibition of the receptor or non-receptor tyrosine kinases. Briefly, the kinases from TK-1 kit (EGFR, HER2, HER4, IGF1R, InsR, KDR, PDGFRa, and PDGFRb) or TK-2 kit (ABL1, BRK, BTK, CSK, Fyn A, Lck, Lyn B, and Src) and substrate/cofactor strips were prepared according to the manufacturer's instructions and protocols previously described by our group [35]. The compounds being tested were dissolved in DMSO to a concentration of 100 μM, which was then used as the stock solution to prepare the 1 μM final concentration in a 1x Kinase Reaction Buffer (40 mM Tris – pH 7.5; 20 mM $MgCl_2$; 0.1 mg/mL BSA; 50 μM DTT). The experiment began with transferring 1 μL of the prepared solutions of the tested compounds onto a 384-well white plate that

was designed for luminescence (Corning). Then, 2 μL of the kinases from the eight-well strip were added into each well, and the plate was incubated for 10 min at RT, after which 2 μL of the substrates from the eight-well substrate/cofactor strip were added to each well, and the plate was left at RT for 1 h. Solutions of 1x Kinase Reaction Buffer with a 5 % vehicle (DMSO) were used as the negative controls without inhibitors or enzymes. The activity of each kinase was determined using an ADP-Glo Kinase Assay (Promega). Firstly, to stop the reaction, 5 μL of ADP-Glo reagent was added to each well, and the plate was incubated for 40 min at RT. Afterwards, 10 μL of the Kinase Detection Reagent was added to each well, and the luminescence was measured in a Varioskan LUX multi-plate reader following a 30-minute incubation at RT. The experiments were performed at least three times. The data was expressed as the percentage of the inhibition of tyrosine kinase after treatment with the tested compounds.

4.5. Binding assays (microscale thermophoresis – MST)

The MST experiments were conducted with the Monolith NT.115 Blue/Red instrument (NanoTemper Technologies) in buffer containing 50 mM HEPES (pH = 7.5), 300 mM NaCl, 10 mM $MgCl_2$, and 0.05 % Tween 20. The recombinant human IGF-I R/IGF1R (His-tagged) protein (Biotechne) was labeled using the Monolith His-Tag labeling kit RED-tris-NTA 2nd Generation (NanoTemper Technologies) for detection in the MST experiments. The final concentration of protein in the assays was 50 nM. The MS168 and MR5K3 were dissolved in DMSO to a concentration of 8.35 mM. Then, the final serial dilution of compounds was set up, starting with a concentration of 10 μM, with a 2-fold dilution down to 0.000305 μM in the assay buffer. For K_d determination, the fluorescently labeled protein was incubated with serial dilution of MS168 or MR5K3 for 15 min at RT. The samples were centrifuged (12,000 rpm; 10 min), then loaded into standard capillaries and measured at 25 °C, using 80 % LED and 40 % MST power. Each assay was repeated at least three times. Data analyses were performed using MO.Affinity Analysis 2.3 software (NanoTemper Technologies). All final graphs were prepared using GraphPad Prism 9.

4.6. Cell culture

The human glioblastoma cell lines LN-18, LN-229, and T98G were purchased from the ATCC, while the U-251 cell line was kindly provided by Professor G. Kramer-Marek from the Institute of Cancer Research (London, UK). The normal human astrocyte (NHA) cell line was acquired from Gibco. A human cerebral endothelial (hCMEC/D3) cell line was obtained from Cedarlane. All the cancer cell lines were cultured in Dulbecco's Modified Eagle's Medium (DMEM) supplemented with heat-inactivated fetal bovine serum (FBS) (10 % v/v; Sigma Aldrich) and penicillin/streptomycin antibiotics (1 % v/v; Gibco), NHA cells were cultured in astrocyte medium with 10 % FBS, an N-2 supplement, EGF (20 ng/mL), and an antibiotic–antimycotic solution (1 % v/v) (all reagents from Gibco), while hCMEC/D3 cells were cultured in Endothelial Cell Growth Medium MV with 2 % fetal calf serum, 0.4 % endothelial cell growth supplement, EGF (10 ng/mL), heparin (90 μg/mL), hydrocortisone (1 μg/mL) (all from PromoCell) and an antibiotic-antimycotic solution (1 % v/v) (Gibco). The cells were kept under standard conditions at 37 °C in a humid atmosphere with 5 % CO_2. Each of the cell lines used during experiments was previously tested against *Mycoplasma* contamination using the PCR technique with specific primers.

4.7. Cytotoxicity studies

4.7.1. 2D monolayer culture model

All the glioblastoma cell lines and normal astrocytes were used during cytotoxicity assays on the 2D monolayer culture. Seeding was done in 96-well transparent plates (Nunc) at a density of 5000 cells per well, followed by incubation for 24 h at 37 °C in a humid atmosphere with 5 % CO_2. After that time, the medium was removed from the wells and 200 μL of varying concentrations of the tested compounds were added. In the control wells, the contents of the wells were exchanged with 200 μL of fresh medium. Plates were then returned to the incubator for three days at the same conditions as previously. Subsequently, the compound solutions were replaced with 100 μL of DMEM without phenol red and 20 μL of CellTiter 96® AQueous One Solution-MTS reagent (Promega) and incubated for 1 h at 37 °C in a humid atmosphere with 5 % CO_2. The absorbance of the plate was then measured at the wavelength λ = 490 nm using a multi-plate reader (Varioskan LUX, Thermo Scientific). Results were normalized against untreated control cells, and IC_{50} values, defined as the concentration of a compound that reduces cell proliferation by 50 %, were calculated using GraphPad Prism 9. Each compound was tested in duplicate within a single experiment, and experiments were repeated three to four times.

4.7.2. 3D spheroid culture model

Cytotoxicity tests on the 3D spheroid cell culture of glioblastoma cells were conducted using 96-well non-adherent transparent plates with a U-shaped bottom (Nunc). Cells were seeded at a density of 4000 cells per well and incubated for 3 days at 37 °C in a humid atmosphere with 5 % CO_2. After incubation, 100 μL of the medium was carefully removed from each well to avoid disturbing the spheroids. Subsequently, 100 μL of the tested compound solutions, prepared at double the desired concentration, were added to the wells, and the plates were incubated for 3 days at 37 °C in a humid atmosphere with 5 % CO_2. After the incubation period, the plates were removed from the incubator and allowed to cool to RT for approximately one hour. Then, 100 μL of the medium was removed from each well and replaced with 100 μL of the CellTiter-Glo® 3D Cell Viability Assay reagent (Promega). The plates were mixed on a shaker (400 rpm; 5 min) and incubated at RT for an additional 25 min. Finally, 100 μL of the medium from each well was transferred to a 96-well white solid plate (Pierce), and the luminescence of the samples was recorded. Results were normalized against untreated control cells, and IC_{50} values, defined as the concentration of a compound that reduces cell proliferation by 50 %, were calculated using GraphPad Prism 9. Each compound was tested in duplicate within a single experiment, and experiments were repeated three to four times.

4.8. Blood-brain barrier permeability assay

4.8.1. Blood-brain barrier permeability assay

Drug permeability assays were performed using the HTS Transwell 96-well Permeable Support System with a 0.4 μm pore size (Corning). The hCMEC/D3 cells were seeded in the 96-well insert plate (apical plate) at a density of 15,000 cells per well with a receiver plate filled with 20 mL of medium and incubated for 5 days at 37 °C in a humid atmosphere with 5 % CO_2. Then, after 4 days, the U-251 cells were seeded in a 96-well plate (basolateral plate) at a density of 8000 cells per well and incubated overnight. The following day, the assay was performed. Solutions of the tested compounds - MS168, alongside the positive reference drug temozolomide and the negative reference drug gefitinib - were prepared in double the desired concentration. Fifty μL of the medium was carefully removed from apical plate wells and exchanged with 50 μL of the prepared solutions. The apical plate was then put into the basolateral plate, and both were co-incubated for 2 h, during which the integrity of the endothelial cell monolayer was assessed by the Lucifer Yellow/Rhodamine 123 assay. 60 μM Lucifer Yellow (LY) and 50 μL Rhodamine 123 (Rh123) fluorescent dye solution in Hanks' Balanced Salt Solution (HBSS) buffer supplemented with 1 % DMSO was prepared and briefly vortexed. 100 μL of LY solution was added into selected wells in the apical plate, while 100 μL or 200 μL of Rh123 solution was added into separate wells in the apical and basolateral plates, respectively. Immediately after that, the fluorescence (λ_{LY} = 428 nm; λ_{Rh123} = 508 nm) was measured, and readings were repeated after 1 and 2 h, respectively. When all fluorescence readings were done,

plates were separated, and the basolateral plate was incubated for another 3 days. Subsequently, the cytotoxicity of drugs applied during the described assay was measured using an MTS assay. The basolateral plate with seeded U-251 cells containing dissolved drugs that passed through an insert during the co-incubation period was kept for three days at 37 °C in a humid atmosphere with 5 % CO_2. Then, all medium was removed from the wells and replaced with 100 µL of DMEM without phenol red and 20 µL of CellTiter 96® AQueous One Solution-MTS reagent (Promega) and incubated for 1 h. The absorbance of the plate was then measured at the wavelength λ = 490 nm using a multi-plate reader Synergy 4 (BioTek).

4.8.2. Visualization of tight junctions in the blood-brain barrier

The integrity of the cell monolayer was confirmed through immunofluorescence imaging. hCMEC/D3 cells were seeded onto µ-Slide 8 Well Glass Bottom slides (Ibidi) pre-coated with laminin at a density of 10,000 cells per well and incubated for five days at 37 °C in a humidified atmosphere with 5 % CO_2. After incubation, wells were briefly washed with PBS and fixed with 4 % paraformaldehyde for 10 min for ZO-1 imaging or 16 % paraformaldehyde for 15 min for occludin imaging. The wells were then washed three times with PBS (5 min per wash), followed by cell membrane permeabilization with 0.3 % Triton X-100 (5 min for ZO-1 and 15 min for occludin) and an additional three PBS washes. Subsequently, all wells were blocked with 5 % goat serum for 1 h and incubated overnight at 4 °C with specific primary antibodies (ZO-1: 1:100; occludin: 1:100). The following day, cells were stained with Hoechst 33342 (10 µg/mL) for 15 min and washed three times with PBS. Fluorescence images ($\lambda_{excitation}$ = 485 nm, $\lambda_{emission}$ = 520 nm) were acquired using a Zeiss Axio Observer.Z1 equipped with a 63 × objective and an FITC filter. The images were then processed using ZEN 3.10 software.

4.9. Annexin V binding assay

The U-251 cells were seeded in 96-well transparent non-adherent plates with U-shaped bottoms (Nunc). Cells were seeded at a density of 4000 cells per well and incubated for 3 days at 37 °C in a humid atmosphere with 5 % CO2. Then, fresh solutions of tested compounds were prepared: MS168 (65 µM), MS179 (5 and 10 µM), MR5K3 (1 and 2 µM), MS165 (2.5 and 5 µM), and osimertinib (30 and 60 µM). 100 µL of medium was removed from each well and replaced with 100 µL of drug solution, followed by an incubation for 2 days. Each concentration was applied to 10 spheroids, which were then collected into a 1.5 mL Eppendorf tube and centrifuged (300 g; 5 min). The supernatant was carefully removed, and the pellet was suspended in 250 µL of StemPro™ Accutase™ Cell Dissociation Reagent (Gibco) to disassociate collected spheroid into single cells. After 10 min of incubation, the cell suspension was pipetted and checked under the microscope – if spheroids were still intact, the incubation cycle was repeated up to three additional times. Single-cell suspension was then centrifuged (300 g; 5 min), resuspended in 1 mL of cold PBS, and again centrifuged under the same conditions. The supernatant was removed, and a mixture of 100 µL of Annexin V Binding Buffer, 5 µL of Annexin V, and 5 µL of 7-AAD was added. The tubes were briefly vortexed and incubated in the dark at RT for 15 min. Subsequently, 200 µL of Annexin V Binding Buffer was added, and cell subpopulations (live, early and late apoptotic, and dead) were counted using a microcapillary Muse Cell Analyzer. The measurements were repeated three times.

4.10. Generation of reactive oxygen species

The U-251 cells were seeded in 96-well black non-adherent plates with U-shaped bottoms (Corning). Cells were seeded at a density of 4000 cells per well and incubated for 5 days at 37 °C. The next day, the medium was removed, and freshly prepared solutions of tested compounds were added: MS168 at the concentration of 65 µM, MS179 at 5 µM, MR5K3 at 1 µM, MS165 at 2.5 µM, and osimertinib at 60 µM. During the kinetic experiment, 3, 6, 9, 12, and 24-hour incubation times were measured. CellROX® Green Reagent (Molecular Probes™) was used to determine the amount of ROS generated in treated samples. To normalize the results, the quantity of cells in the measured wells was estimated by measuring the amount of protein present within the well. A spheroid lysis was performed immediately after the CellROX measurement, contents of the wells were carefully removed with the spheroid still present inside, then 100 µL of freshly prepared RIPA buffer (a mixture of Halt Phosphatase Inhibitor Cocktail, Halt Protease Inhibitor Cocktail, and 0.5 M EDTA, obtained from Thermo Scientific) was added. The plate was placed on ice and incubated for 20 min, buffer was then mixed inside wells using a multi-channel pipette, followed by centrifugation of a plate (4000 rpm; 10 min). 20 µL of the obtained supernatant was transferred to a 96-well flat-bottomed plate, and the protein content was measured using a Micro BCA™ Protein Assay Kit (Thermo Scientific) according to the manufacturer's protocol. Experiments were performed three times, with each compound tested in duplicate. The results are expressed as the percentage of the ROS level compared to untreated control cells.

4.11. Immunoblotting

The U-251 cells were seeded in 3 cm non-adherent Nunclon Sphera dishes (Nunc) at a density of 200,000 cells per dish in 2 mL of medium and incubated for 10 days at 37 °C. On the fifth day, an additional 1 mL of fresh medium was added. After the 10-day incubation, the contents of the dishes were collected into 5 mL Eppendorf tubes and centrifuged (300 g; 5 min). The resulting spheroid pellet was resuspended in 2 mL of freshly prepared solutions of the tested compounds: MS168 (65 µM), MS179 (5 µM), MR5K3 (1 µM), MS165 (2.5 µM), and osimertinib (30 µM). The cells were then reintroduced into the dishes and incubated for 24 h. Following this incubation, the cells were collected again into Eppendorf tubes, centrifuged (2000 rpm; 5 min), and resuspended in 300 µL of RIPA buffer containing Halt Phosphatase Inhibitor Cocktail, Halt Protease Inhibitor Cocktail, and 0.5 M ethylenediaminetetraacetic acid (EDTA) (all from Thermo Scientific). The tubes were incubated on ice for 20 min, followed by 15 s of sonication. The resulting cell lysates were centrifuged (10,000 rpm; 5 min). The supernatant was transferred to new Eppendorf tubes and stored at −80 °C. Protein concentration was assessed before each experiment using the Micro BCA™ Protein Assay Kit (Thermo Scientific) according to the manufacturer's protocol. Samples prepared for immunoblotting contained 10 µg of protein. Western blotting was performed using polyacrylamide gel electrophoresis, wet transfer onto nitrocellulose membranes, and blocking with 5 % non-fat milk powder in 1X TTBS. Membranes were incubated overnight at 4 °C with primary antibodies, followed by three 5-minute washes. This was followed by a 60-minute incubation with secondary antibodies at RT, three additional 5-minute washes, and a final 5-minute incubation with SuperSignal™ West Pico Chemiluminescent Substrate (Thermo Scientific) at RT. The chemiluminescence signals from prepared membranes were recorded using a ChemiDoc™ XRS + System (Biorad). During immunoblotting, the following primary antibodies were used: 4F2hc (#47213), Akt (#9272), GPX4 (#52455), HO-1 (#5853), IRP1 (#20272), IRP2 (#37135), p44/42 MAPK (#9102), phospho-p44/42 MAPK (#9101), $p27^{Kip1}$ (#3688), and p70 S6 kinase (#2708) (all from Cell Signaling), ferrochelatase (sc-377377) (Santa Cruz Biotechnology), FXN (STJ113368) (St John's Laboratory), and RAS (ab52939) (Abcam). Secondary anti-mouse (#7076) and anti-rabbit (#7074) antibodies were obtained from Cell Signaling. The obtained results were analyzed using ImageJ 1.41. Measurements of all chosen targets were repeated at least four times.

4.12. In vivo studies

4.12.1. Zebrafish Toxicity Studies

Toxicity analysis was conducted using freshly obtained zebrafish (Danio rerio) embryos, which were distributed onto 24-well plates, with 5 embryos per well, two wells per group. The embryos were maintained in E3 medium and subjected to treatment with MS168, MS181, and MS165 at doses ranging from 0 to 20 μM on separate plates. Treated embryos were incubated in a controlled environment in an incubator at a constant temperature of 28 ± 0.5 °C and a day-night cycle of 14 h of light followed by 10 h of darkness. After 96 h of exposure, the following developmental endpoints were assessed: [1] coagulation of embryos, [2] absence of somite formation, [3] tail separation, and [4] absence of cardiac activity.

4.12.2. Zebrafish xenograft experiments

Tumor LN-229 cell lines were cultured until cells reached 70 % of confluence, then washed with phosphate-buffered saline (PBS), detached, and stained with Vybrant CM-DiI (ThermoFisher; 4 μL/mL in 1X PBS) for 10 min at 37 °C in darkness. The stained cell suspension was resuspended in PBS to a final concentration of 2.5×10^6 cells/mL. Fluorescently labeled cancer cells were injected into the yolk sac 2 days post-fertilization (dpf) of zebrafish embryos. Before injection, embryos were anesthetized with tricaine. Each embryo received approximately 500–1000 cells. Successfully engrafted embryos were imaged (Zeiss Discovery V8) to assess tumor size and subsequently allocated into treatment groups: E3, MS168 – 0.5, 1, 2.5 μM, MS181 – 0.5, 1, 2.5 μM, and MS165 – 0.5, 1, 2.5 μM. Then, the embryos were incubated at 31 °C for 72 h but monitored daily to eventually remove dead embryos. At 72 h post-injection, tumor size was measured via image analysis. Fluorescence images were captured using a Zeiss Discovery V8 fluorescence microscope and analyzed with FIJI/ImageJ software to quantify tumor-derived fluorescence at injection point and 72 h post-injection.

4.13. Statistics

IC_{50} values of tested compounds were determined with nonlinear regression analysis. Results obtained during Annexin V binding assays and ROS level measurements were analyzed using one-way ANOVA multi-comparison analyses with Bonferroni's post hoc test (*$p < 0.05$, **$p < 0.01$, ***$p < 0.001$, ****$p < 0.0001$ vs. control) as a result correction. The activity of receptor tyrosine kinases between tested TSC compounds and positive control – Osimertinib were analyzed using two-way ANOVA multi-comparison analyses with Dunnett's post hoc test. All aforementioned statistical analyses were performed using GraphPad Prism 9 software. The rest of the data was shown in the form of mean ± SD for three to four independent experiments.

CRediT authorship contribution statement

Maria Książek: Methodology, Investigation. **Anna Mrozek-Wilczkiewicz:** Writing – original draft, Supervision, Project administration, Methodology, Investigation, Funding acquisition, Conceptualization. **Anna Boguszewska-Czubara:** Writing – review & editing, Methodology, Investigation. **Marcin Pacholczyk:** Writing – review & editing, Methodology, Investigation. **Mateusz Korzec:** Methodology, Investigation. **Maciej Serda:** Methodology, Investigation. **Patrycja Rawicka:** Methodology, Investigation. **Patryk Zioła:** Writing – original draft, Methodology, Investigation, Formal analysis. **Katarzyna Malarz:** Writing – original draft, Supervision, Project administration, Methodology, Investigation.

Declaration of Competing Interest

The authors declare that they have no known competing financial interests or personal relationships that could have appeared to influence the work reported in this paper.

Acknowledgements

The financial support of the National Science Centre grants 2020/39/O/NZ5/02342 (AMW, PZ) and 2019/35/B/NZ5/04208 (KM) is greatly appreciated. Crystallographic data for MS168 was deposited in the Cambridge Crystallographic Data Center (CCDC: 1422303). This data can be obtained free of charge from The Cambridge Crystallographic Data Centre via www.ccdc.cam.ac.uk/structures.

Authors' Contributions

PZ performed the biological assays and the chelation studies, analyzed the data, and wrote the manuscript; KM performed the kinase activity inhibition and binding affinity studies, described these data, and supervised PZ during the biological part; PR planned, performed, described, and supervised PZ in the chelation studies; MK and MS performed the synthesis; ABC performed and analyzed *in vivo* studies; MP performed and analyzed molecular docking; MKS performed single crystal measurement and refined the crystal structure of MS168; and AMW created the research hypothesis, planned the experiments, analyzed the data, and wrote the manuscript.

Appendix A. Supporting information

Supplementary data associated with this article can be found in the online version at doi:10.1016/j.biopha.2025.118692.

Data availability

Data will be made available on request.

References

[1] J.A. Lessa, M.A. Soares, R.G. dos Santos, I.C. Mendes, L.B. Salum, H.N. Daghestani, et al., Gallium(III) complexes with 2-acetylpyridine-derived thiosemicarbazones: antimicrobial and cytotoxic effects and investigation on the interactions with tubulin, BioMetals 26 (1) (2013) 151–165.

[2] I. D'Agostino, G.E. Mathew, P. Angelini, R. Venanzoni, G. Angelini Flores, A. Angeli, et al., Biological investigation of N-methyl thiosemicarbazones as antimicrobial agents and bacterial carbonic anhydrases inhibitors, J. Enzym. Inhib. Med Chem. 37 (1) (2022) 986–993.

[3] B. Shakya, P.N. Yadav, Thiosemicarbazones as potent anticancer agents and their modes of action, Mini Rev. Med. Chem. 20 (8) (2020) 638–661.

[4] H.S. Adhikari, A. Garai, K.D. Manandhar, P.N. Yadav, Pyridine-based NNS tridentate chitosan thiosemicarbazones and their Copper(II) complexes: synthesis, characterization, and anticancer activity, ACS Omega 7 (35) (2022) 30970–30988.

[5] K. Bajaj, R.M. Buchanan, C.A. Grapperhaus, Antifungal activity of thiosemicarbazones, bis(thiosemicarbazones), and their metal complexes, J. Inorg. Biochem. 225 (2021) 111620.

[6] T. Li, M. Le, H. Wen, J. Du, Z. Wang, S. Zhang, et al., Natural products in crop protection: thiosemicarbazone derivatives of 3-acetyl-N-benzylindole as antifungal agents and their mechanism of action, Pest Manag Sci. 79 (8) (2023) 2801–2810.

[7] R. Krishnan, K. Prathiba, V. Jayaprakash, A. Basu, N. Mishra, B. Zhou, et al., Synthesis and ribonucleotide reductase inhibitory activity of thiosemicarbazones, Bioorg. Med. Chem. Lett. 18 (23) (2008) 6248–6250.

[8] N.S. Moorthy, N.M. Cerqueira, M.J. Ramos, P.A. Fernandes, Development of ribonucleotide reductase inhibitors: a review on structure activity relationships, Mini Rev. Med Chem. 13 (13) (2013) 1862–1872.

[9] G.J. Kontoghiorghes, C.N. Kontoghiorghe, Iron and chelation in biochemistry and medicine: new approaches to controlling iron metabolism and treating related diseases, Cells 9 (6) (2020).

[10] O.V. Selyutina, P.A. Kononova, V.E. Kushnar, E.A. Shelepova, M.G. Azad, R. Afroz, et al., Ascorbate-and iron-driven redox activity of Dp44mT and emodin facilitates peroxidation of micelles and bicelles, Biochim. Et. Biophys. Acta (BBA) Gen. Subj. 1866 (4) (2022) 130078.

[11] S. Plantamura, D. Sun, J. Van Valkenburgh, J. Valenzuela, B. Buehle, D. Steele, et al., Activity and electrochemical properties: iron complexes of the anticancer drug triapine and its analogs, JBIC J. Biol. Inorg. Chem. 24 (5) (2019) 631–652.

[12] K.D. Welch, T.Z. Davis, S.D. Aust, Iron autoxidation and free radical generation: effects of buffers, ligands, and chelators, Arch. Biochem Biophys. 397 (2) (2002) 360–369.

[13] J.M. Myers, Q. Cheng, W.E. Antholine, B. Kalyanaraman, A. Filipovska, E.S. Arner, et al., Redox activation of Fe(III) thiosemicarbazones and Fe(III)-bleomycin by thioredoxin reductase: specificity of enzymatic redox centers and analysis of reactive species formation by ESR spin trapping, Free Radic. Biol. Med 60 (2013) 183–194.
[14] K. Malarz, A. Mrozek-Wilczkiewicz, M. Serda, M. Rejmund, J. Polański, R. Musioł, The role of oxidative stress in activity of anticancer thiosemicarbazones, Oncotarget 9 (25) (2018) 17688–17710.
[15] C.M. Weekley, C. He, Developing drugs targeting transition metal homeostasis, Curr. Opin. Chem. Biol. 37 (2017) 26–32.
[16] C.C. Bridges, R.K. Zalups, Cystine and glutamate transport in renal epithelial cells transfected with human system xc(-) (c). Kidney Int 68 (2) (2005) 653–664.
[17] A. Walcourt, J. Loustalot-Mills, J. Kovaiyan, B.B. Adenuga, D.S. Kalinowski, D. R. Lovejoy, et al., Anti-plasmodial activity of aroylhydrazone and thiosemicarbazone iron chelators: effect on erythrocyte membrane integrity, parasite development and the intracellular labile iron pool, J. Inorg. Biochem 129 (2013) 43–51.
[18] Y. Yu, D.S. Kalinowski, Z. Kovacevic, A.R. Siafakas, P.J. Jansson, C. Stefani, et al., Thiosemicarbazones from the old to new: iron chelators that are more than just ribonucleotide reductase inhibitors, J. Med Chem. 52 (17) (2009) 5271–5294.
[19] G. Shenoy, J.R. Connor, A closer look at the role of iron in glioblastoma, Neuro Oncol. 25 (12) (2023) 2136–2149.
[20] T. Huequeraz, S.A. Ghiasi, M. de Wit, I. de Heer, K. Draaisma, J. van Riet, et al., The EGFRvIII transcriptome in glioblastoma: a meta-omics analysis, Neuro Oncol. 24 (3) (2022) 429–441.
[21] N. Rabab, F.E. Ait Mohand, N. Kravchenko-Balasha, Understanding glioblastoma signaling, heterogeneity, invasiveness, and drug delivery barriers, Int J. Mol. Sci. 24 (18) (2023).
[22] F. Liu, S. Ye, L. Zhao, Q. Niu, The role of IGF/IGF-1R signaling in the regulation of cancer stem cells, Clin. Transl. Oncol. 26 (12) (2024) 2924–2934.
[23] M. Serda, A. Mrozek-Wilczkiewicz, J. Jampilek, M. Peska, E. Kralova, M. Vepova, et al., Investigation of the biological properties of (hetero)aromatic thiosemicarbazones, Molecules 17 (11) (2012) 13403–13502.
[24] M. Serda, D.S. Kalinowski, N. Basko, E. Potuckova, A. Mrozek-Wilczkiewicz, R. Musiol, et al., Exploring the anti-cancer activity of novel thiosemicarbazones generated through the combination of retro-fragments: dissection of critical structure-activity relationships, PLoS One 9 (10) (2014) e110291.
[25] A. Mrozek-Wilczkiewicz, K. Malarz, M. Rejmund, J. Polanski, R. Musiol, Anticancer activity of the thiosemicarbazones that are based on di-2-pyridine ketone and quinoline moiety, Eur. J. Med. Chem. 171 (2019) 180–194.
[26] S. Sarkar, T. Mondal, S. Roy, R. Saha, A.K. Ghosh, S.S. Panja, A multi-responsive thiosemicarbazone-based probe for detection and discrimination of group 12 metal ions and its application in logic gates, N. J. Chem. 42 (18) (2018) 15157–15169.
[27] M.F. Pouet, E. Baures, S. Vaillant, O. Thomas, Hidden isosbestic point(s) in ultraviolet spectra, Appl. Spectrosc. 58 (4) (2004) 486–490.
[28] R. Gawecki, P. Rawicka, M. Rogalska, M. Serda, A. Mrozek-Wilczkiewicz, Iron metabolism in aminolevulinic acid-photodynamic therapy with iron chelators from the thiosemicarbazone group, Int J. Mol. Sci. 25 (19) (2024) 10468.
[29] S. Gui, P. Cao, X. Zhong, Y. Lin, B. Lin, M. Jiang, Designing an anticancer Pd(II) complex as poly(ADP-ribose) polymerase 1 inhibitor, Int J. Biol. Macromol. 297 (2025) 139885.
[30] J.Y. Hu, Y. Guo, R.A. Mao, L.Y. Dang, Z.Z. Gu, Z. Wang, et al., Copper complexes with quinoline-thiosemicarbazone hybrid ligand promoting apoptosis by causing DNA and mitochondria dual lesions, J. Mol. Struct. 1314 (2024) 138719.
[31] Y. Fu, Y. Liu, J. Wang, C. Li, S. Zhou, Y. Yang, et al., Calcium release induced by 2-pyridinecarboxaldehyde thiosemicarbazone and its copper complex contributes to tumor cell death, Oncol. Rep. 37 (3) (2017) 1662–1670.
[32] A. Tarman, T. Kurz, Lysosomal iron, iron chelation, and cell death, Antioxid. Redox Signal 18 (8) (2013) 888–898.
[33] M.A. Greenough, J. Camakaris, A.I. Bush, Metal dyshomeostasis and oxidative stress in alzheimer's disease, Neurochem. Int 62 (5) (2013) 540–555.
[34] A. Popovic-Bijelic, C.R. Kowol, M.E. Lind, J. Luo, F. Himo, E.A. Enyedy, et al., Ribonucleotide reductase inhibition by metal complexes of triapine (3-aminopyridine-2-carboxaldehyde thiosemicarbazone): a combined experimental and theoretical study, J. Inorg. Biochem 105 (11) (2011) 1422–1431.
[35] K. Malarz, J. Mularski, M. Pachończyk, R. Musiol, Styrylquinazoline derivatives as ABL inhibitors selective for different DFG orientations, J. Enzym. Inhib. Med Chem. 38 (1) (2023) 2201410.
[36] R. Alcaraz, P. Muniz, M. Cavia, D. Palacios, K.G. Samper, R. Gil-Garcia, et al., Thiosemicarbazone metal complexes exhibiting cytotoxicity in colon cancer cell lines through oxidative stress, J. Inorg. Biochem 206 (2020) 110993.
[37] S.K. Chiang, S.E. Chen, L.C. Chang, The role of HO-1 and its crosstalk with oxidative stress in cancer cell survival, Cells 10 (9) (2021).
[38] F.J. Li, H.Z. Long, Z.W. Zhou, H.Y. Luo, S.G. Xu, L.C.System X(c) Gao, C) (-)/GSH/GPX4 axis: an important antioxidant system for the ferroptosis in drug-resistant solid tumor therapy, Front Pharm. 13 (2022) 910292.
[39] Y. Liu, S. Lu, L.L. Wu, L. Yang, L. Yang, J. Wang, The diversified role of mitochondria in ferroptosis in cancer, Cell Death Dis. 14 (8) (2023) 519.
[40] M. Serda, D.S. Kalinowski, A. Mrozek-Wilczkiewicz, R. Musiol, A. Szurko, A. Ratuszna, et al., Synthesis and characterization of quinoline-based thiosemicarbazones and correlation of cellular iron-binding efficacy to anti-tumor efficacy, Bioorg. Med Chem. Lett. 22 (17) (2012) 5527–5531.
[41] D.L. Zhang, M.C. Ghosh, T.A. Rouault, The physiological functions of iron regulatory proteins in iron homeostasis - an update, Front Pharm. 5 (2014) 124.
[42] C.O. Obu, T. Rouiyan, H.A. Dailey, A.E. Medlock, Ferrochelatase: mapping the intersection of iron and porphyrin metabolism in the mitochondria, Front Cell Dev. Biol. 10 (2022) 894591.
[43] M.E. Bahar, H.J. Kim, D.R. Kim, Targeting the RAS/RAF/MAPK pathway for cancer therapy: from mechanism to clinical studies, Signal Transduct. Target Ther. 8 (1) (2023) 455.
[44] A.I. Duarte, P. Santos, C.R. Oliveira, M.S. Santos, A.C. Rego, Insulin neuroprotection against oxidative stress is mediated by akt and GSK-3beta signaling pathways and changes in protein expression, Biochim Biophys. Acta 1783 (6) (2008) 994–1002.
[45] C.N. Han, Y.J. Geng, F. Li, T. Yang, D.F. Su, J.L. Duan, et al., Insulin-like growth factor-1 receptor activation prevents hydrogen peroxide-induced oxidative stress, mitochondrial dysfunction and apoptosis, Apoptosis 16 (11) (2011) 1118–1127.
[46] Y.T. Gu, Y.X. Xue, Y.F. Wang, J.H. Wang, Q.R. ShangGuan, J.X. Zhang, et al., Role of ROS/RhoA/PCBL/PKB signaling in NS1619-mediated blood-tumor barrier permeability increase, J. Mol. Neurosci. 48 (1) (2012) 302–312.
[47] M.D. Caverzan, L.E. Ibarra, Advancing glioblastoma treatment through iron metabolism: a focus on TIRI and ferroptosis innovations, Int J. Biol. Macromol. 278 (Pt 2) (2024) 134777.
[48] J. Shi, M. Barakat, D. Chen, L. Chen, Bicellular tight junctions and wound healing, Int J. Mol. Sci. 19 (12) (2018).
[49] Y.D. Zeng, H. Liao, T. Qin, L. Zhang, W.D. Wei, J.Z. Liang, et al., Blood-brain barrier permeability of gefitinib in patients with brain metastases from non-small-cell lung cancer before and during whole brain radiation therapy, Oncotarget 6 (10) (2015) 8366–8376.
[50] G.M. Sheldrick, Crystal structure refinement with SHELXL, Acta Crystallogr C. 71 (Pt 1) (2015) 3–8.

4.3. [P3]. Styrylquinoline derivatives as IGF1R inhibitors

Autorzy: Zioła P., Malarz K., Pacholczyk M., Cieślik W., Rawicka P., Musioł R., Mrozek-Wilczkiewicz A.

Referencja: *ACS Medicinal Chemistry Letters*, 2026, **17(2)**, 351-357

Numer DOI: 10.1021/acsmedchemlett.5c00526

Impact Factor czasopisma: 4 (2024)

Liczba punktów MNiSW czasopisma: 140 (2026)

Mój udział w pracy polegał na opracowaniu metodologii, wykonaniu badań cytotoksyczności oraz pisaniu manuskryptu.

ACS Medicinal Chemistry Letters

pubs.acs.org/acsmedchemlett

Letter

Styrylquinoline Derivatives as IGF1R Inhibitors

Patryk Ziola, Katarzyna Malarz, Marcin Pacholczyk, Wioleta Cieślik, Patrycja Rawicka, Robert Musiol, and Anna Mrozek-Wilczkiewicz*

Cite This: ACS Med. Chem. Lett. 2026, 17, 351−357

Read Online

ACCESS | Metrics & More | Article Recommendations | Supporting Information

ABSTRACT: Styrylquinoline analogues exhibiting antiproliferative activity against glioblastoma multiforme were tested for tyrosine kinase inhibition. A preliminary structure activity relationship analysis based on previous results showed that the styrylquinoline fragment is a promising privileged structure. The addition of appropriate pharmacophores to both the quinoline structure and the benzene ring, which was attached to the 2-position, significantly altered the antiproliferative properties. Namely, OH or NO_2 substituents had a positive effect on activity, while F and OAc molecular fragments had a negative impact. Screening conducted on a panel of receptor tyrosine kinases revealed the high potential of the tested compounds for use as insulin-like growth factor 1 receptor inhibitors. Molecular docking performed on the insulin-like growth factor 1 receptor unphosphorylated inactive conformation supports screening results suggesting high binding affinity of the active styrylquinoline derivatives.

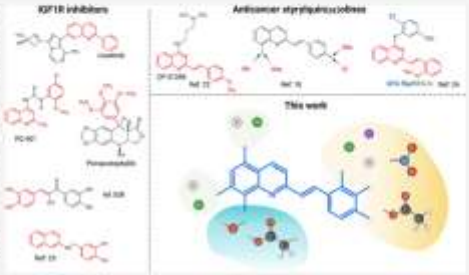

KEYWORDS: *styrylquinoline, IGF1R inhibitors, antiproliferative activity, glioblastoma multiforme*

Cell growth in organisms is regulated by multiple systems, including growth factors and their corresponding receptors. These molecules play crucial roles in signal transduction and, consequently, in the regulation of cell proliferation and survival—a relationship that becomes especially evident in cancer progression. Overexpression or mutations of certain growth factor receptors are characteristic of many types of neoplasms, such as aberrant activity of the insulin-like growth factor 1 receptor (IGF1R), a receptor tyrosine kinase (RTK) that plays a major role in cell proliferation, carcinogenesis, and tumor growth.[1] IGF1R is activated by binding to two insulin-like growth factors (IGF1 and IGF2) or to insulin, with the highest affinity being to IGF1, leading to an initiation of downstream signaling pathways.[2] Its mutation or dysregulation has been noticed in multiple cancers, including breast, prostate, and colorectal cancers, often contributing to treatment resistance and poor prognosis. Recent reports suggest that IGF1R-targeted therapy could also be effective against glioblastoma multiforme (GBM).[3] Inhibition of IGF1R's tyrosine kinase activity is expected to weaken downstream signaling and thereby impede tumor growth. Therefore, targeting IGF1R has been revealed as a promising strategy in cancer therapy. Although this therapeutic direction remains largely unexplored, there is an increasing number of reports on new inhibitors of IGF1R and their potential use.[4]

The importance of heterocyclic moieties in inhibition is evident in the well-known IGF1R and insulin receptor (IR) inhibitors. These receptor tyrosine kinases share approximately 70% sequence homology and are activated by the same growth factors, and multiple studies have demonstrated crosstalk between them.[5] Due to their high similarity and complementary roles in cellular signaling, many IGF1R inhibitors also inhibit IR to a comparable extent. A key example is linsitinib (Figure 1), a small-molecule ATP-competitive dual IGF1R/IR inhibitor.[6] Despite the high affinity for these RTKs, linsitinib exhibits high selectivity, showing more than 100-fold selectivity over other similar kinases. Therefore, this compound is the most advanced prospective drug with a mechanism connected with the inhibition of insulin-like and thyrotropin (TSH-R) receptors, being in phase 2b clinical trials.[7] Recently, Boutin et al. revealed that linsitinib inhibits crosstalk between IGF1R and TSH-R in human thyrocytes and also in vivo.[8]

Other examples of IGF1R/IR inhibitors are PQ401, with a quinolone scaffold, and NVP-AEW-541, which is based on pyrimidine. Similarly, BMS-754807 binds with its benzimidazole moiety to IGF1R, forming hydrogen bonds and occupying the binding pocket.[9] An interesting example of a small

Received: September 2, 2025
Revised: January 9, 2026
Accepted: January 12, 2026
Published: January 16, 2026

ACS Publications © 2026 American Chemical Society

https://doi.org/10.1021/acsmedchemlett.5c00526
ACS Med. Chem. Lett. 2026, 17, 351−357

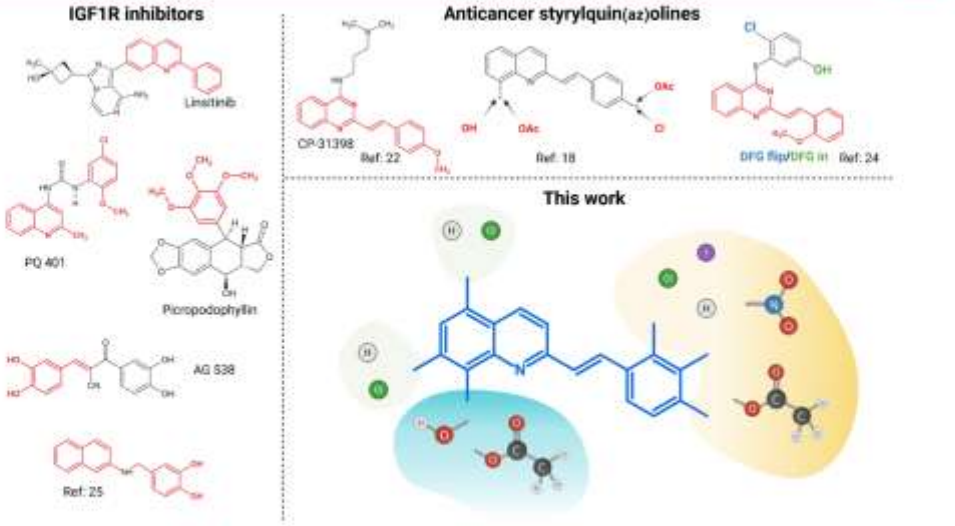

Figure 1. Design idea according to small fragments exchange method. Analysis of known inhibitors of IGF1R and anticancer SQs supports the current investigation. The (styryl)quinoline motif is denoted in red.

molecule inhibitor is the curcumin derivative, AG538, which is a competitive tyrphostin (tyrosine phosphorylation inhibitor). Its activity model may also explain the anticancer activity of curcumin, which has been connected with the downregulation of IGF1R gene expression at the transcriptional level.[10] Moreover, the natural compound picropodophyllin, isolated from podophyllum resin, has been described as an IGF1R inhibitor; however, its plausible mechanism of action also covers an insulin-independent pathway via mitotic catastrophe and tubulin depolarization.[11] Picropodophyllin is a highly selective IGF1R inhibitor that functions through a non-ATP-competitive mechanism.[12] It blocks IGF1R autophosphorylation and consequently suppresses the Akt pathway. Partial degradation of IGF1R (30%−50%) after contact with picropodophyllin has also been observed, which may contribute to its anticancer properties. Notably, picropodophyllin does not inhibit IR, but demonstrates a greater selectivity against IGF1R than its other inhibitors. Usage of picropodophyllin and its analogues, such as an AXL-1717, which has entered phase 2 clinical trials, allows for the development of an alternative treatment strategy against IGF1R-dependent neoplasms.[13]

An intriguing observation can be made regarding the structural features of the described inhibitors: they incorporate multiple pharmacophores, including quinoline, caffeic acid, and styryl moieties. This structural convergence prompted us to revisit our styrylquinoline (SQ) library as potential inhibitors of the target protein. Although direct studies exploring interactions between SQs and IGF1R are limited, the intrinsic characteristics of SQs, particularly their planar, aromatic architecture, and metal-chelating ability, support their candidacy for targeting ATP-binding pockets or modulating downstream kinase activity. Our research group has previously explored SQs over several years for their antimicrobial[14,15] and anticancer[16−18] properties (Figure 1). Their activity is largely mediated through the generation of reactive oxygen species, the disruption of the mitochondrial membrane,[19] and the activation of the p53-dependent apoptotic pathway. Given that IGF1R signaling is closely linked to the regulation of apoptosis, oxidative stress responses, and mitochondrial function,[20] the relevance of SQs in this context becomes even more appealing.

Further structural refinements, such as the introduction of thiadiazole or quinazoline fragments, have enabled SQs to act as multikinase inhibitors. El-Sayed et al. reported thiadiazole-based SQs with submicromolar activity against HepG2 liver and colon cancer lines, functioning as EGFR (epidermal growth factor receptor) kinase inhibitors comparable to sorafenib.[21] In our research, similar activity was observed,[22] which suggested possible cross-reactivity or dual-target engagement within the RTK family. We also indicated significant interplay between iron ion chelation and cellular inhibition of the EGFR receptor signaling pathway.[23] More recently, in a series of SQs, structural features responsible for the selective inhibition of the different orientations of the DFG motif (Asp-Phe-Gly) in ABL kinase were revealed, further highlighting the potential of this direction of research.[24]

Moreover, studies on IGF1R inhibitors further support our observation. The knowledge that has been gathered on known inhibitors enables the identification of key interactions, and even specific fragments, that may determine the desired biological activity. An interesting example is the work of Moriev et al.,[25] in which the authors identified several novel chemotypes with attractive properties and structural novelties as potential IGF1R inhibitors. They focused on two main approaches for selecting these compounds: ligand- and target-based selection. One of their structures resembled the SQ skeleton. Similarly, Fang et al., by virtual screening of the NCI database of IGF1R inhibitors, selected several quinoline-based structures as potentially active.[26]

SQ derivatives have been studied by our team for many years, in particular those with substitution at the 2-position. The compounds investigated in this study were synthesized

https://doi.org/10.1021/acsmedchemlett.5c00526
ACS Med. Chem. Lett. 2026, 17, 351−357

Table 1. Cytotoxicity of 2-Styryloquinoline Derivatives against GBM Cell Lines[a]

Compound coding (coding from [19], *coding from [18])	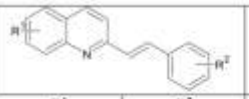		IC_{50} values [μM]				
	R^1	R^2	LN-18	LN-229	T98G	U-87 MG	U-251
ES5 (10u)	8-OAc	2-Cl	4.107 ± 0.568	>25	>25	7.700 ± 0.906	>25
ES2B (4b*)	8-OH	3-OAc	6.659 ± 0.564	10.64 ± 0.705	>25	10.68 ± 0.470	18.08 ± 0.755
ES17B (6b)	8-OH	2-OAc-4-Cl	>25	>25	>25	16.04 ± 1.020	>25
ES18B (8b)	8-OH	2-Cl-6-F	>25	>25	>25	>25	>25
ES58 (7c)	5,7-Cl-8-OAc	2-Cl	12.91 ± 1.505	12.76 ± 2.125	>25	2.800 ± 0.547	10.71 ± 0.805
ES20A	5,7-Cl-8-OAc	2,3-Cl	>25	>25	>25	16.10 ± 2.670	>25
ES20B (5d)	5,7-Cl-8-OH	2,3-Cl	**1.459 ± 0.458**	>25	>25	6.983 ± 0.984	>25
ES24A (9c)	5,7-Cl-8-OAc	2-Cl-6-F	>25	>25	>25	10.31 ± 1.199	>25
ES24B (6d)	5,7-Cl-8-OH	2-Cl-6-F	>25	>25	>25	3.293 ± 0.822	>25
ES29B (7d)	5,7-Cl-8-OH	2-I	6.535 ± 1.094	11.43 ± 1.520	>25	1.713 ± 0.391	2.606 ± 0.815
ES28B (9d)	5,7-Cl-8-OH	3-CN	8.619 ± 1.038	>25	>25	3.925 ± 0.801	3.880 ± 0.639
ES25A (21c)	5,7-Cl-8-OAc	2-NO_2	4.469 ± 0.566	9.102 ± 0.733	**18.36 ± 1.850**	1.210 ± 0.327	7.897 ± 0.726
ES25B (12d)	5,7-Cl-8-OH	2-NO_2	6.030 ± 0.786	>25	>25	2.931 ± 0.433	6.843 ± 0.820
ES26A (22c)	5,7-Cl-8-OAc	3- NO_2	8.459 ± 0.474	9.818 ± 1.305	>25	8.768 ± 1.297	5.188 ± 0.732
ES26B (13d)	5,7-Cl-8-OH	3- NO_2	10.18 ± 1.567	10.82 ± 1.510	>25	11.66 ± 1.700	6.753 ± 1.224
ES27A (23c)	5,7-Cl-8-OAc	4- NO_2	13.39 ± 2.380	13.82 ± 1.810	>25	14.65 ± 1.660	7.097 ± 0.331
ES27B (14d)	5,7-Cl-8-OH	4- NO_2	11.30 ± 0.455	9.327 ± 1.492	>25	7.972 ± 0.705	8.013 ± 1.807
ES45A (24c)	5,7-Cl-8-OAc	2,4- NO_2	2.393 ± 0.645	13.42 ± 2.075	>25	2.444 ± 0.392	1.068 ± 0.472
ES45B (15d)	5,7-Cl-8-OH	2,4- NO_2	2.903 ± 0.860	**7.526 ± 0.795**	>25	**1.130 ± 0.242**	**0.258 ± 0.065**
ES55A (18c)	5,7-Cl-8-OAc	2-OAc-3- NO_2	>25	19.36 ± 1.585	>25	11.92 ± 1.245	8.320 ± 1.222
Erlotinib			>25	>25	>25	>25	>25

[a]Color scale: green (<5 μM), yellow (5−10 μM), orange (10−20 μM), red (>20 μM). Bold indicates the most active compound for each cell line. IC_{50} values are presented in the form of mean ± SD from 3−6 independent experiments.

and characterized in our previous studies.[18,19] One of the topics we focused on was their activity in the context of their impact on the p53 protein. In these studies, we analyzed colon cancer cell lines (HCT 116) with a different expression of the *TP53* tumor suppressor gene. In the present paper, we present a structure−activity relationship (SAR) analysis based on the activity data of the GBM cell lines LN-18, LN-229, T98G, U-87 MG, and U-251 (Table 1). A general SAR analysis revealed several key patterns consistent across most of the tested GBM cell models. The highest sensitivity was observed for the U-251, U-87 MG, and LN-18 cell lines, which showed the greatest proportion of active compounds with the lowest IC_{50} values. These cell lines are also among the most widely used in glioblastoma research and closely reflect the typical drug response profile of GBM. The LN-229 cell line exhibited moderate sensitivity, but some compounds (e.g., **ES25A** and **ES45B**) showed significant activity. In contrast, the T98G line was the most resistant, with only **ES25A** showing moderate activity (18.36 μM), confirming its value as a model of treatment resistance.

In the analyzed compounds, the presence of chlorine substituents on the quinoline ring (5,7-Cl) was significant. Their presence generally correlated with higher biological activity, which could have resulted from their impact on lipophilic properties (higher log *P*) and their ability to interact with biological targets. The substituent at the 8-position of the

https://doi.org/10.1021/acsmedchemlett.5c00526
ACS Med. Chem. Lett. 2026, 17, 351−357

Table 2. Inhibition of IGF-1R Kinase by Tested Compounds[a]

		Degree of inhibition [%]									
Kinase name	conc [μM]	ES2B	ES20B	ES25A	ES25B	ES26B	ES28B	ES29B	ES45A	ES45B	ES58
IGF-1R	1	62.95	18.66	8.25	6.35	9.31	11.17	18.08	61.56	51.59	58.00

[a]Color scale: green (>60%), yellow (>50%), orange (>10%), red (<10%). Degrees of inhibition are presented as mean percentages from three independent experiments.

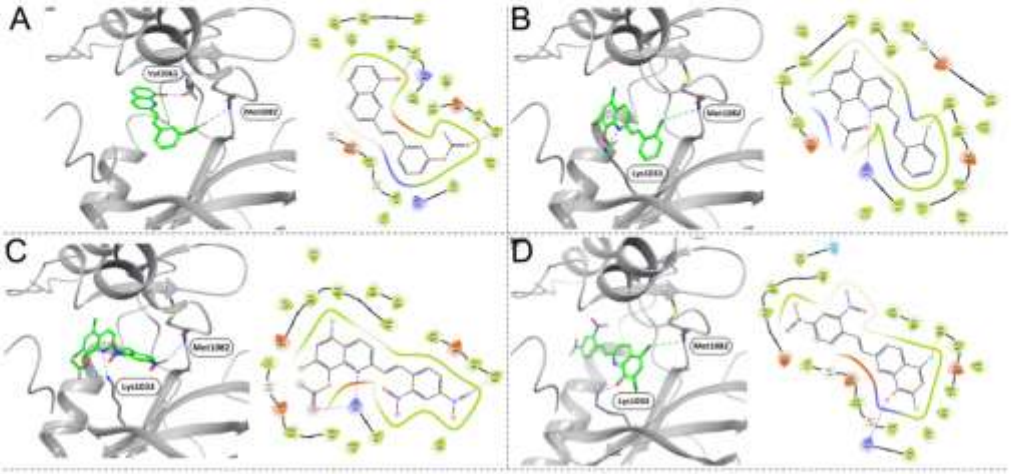

Figure 2. Molecular docking studies of **ES2B**: (A) **ES58**, (B) **ES45A**, (C) **ES45B**, and (D) **IGF1R** unphosphorylated inactive conformation.

quinoline played a further significant role. In most cases, the hydroxyl substituent (8-OH) exhibited better biological properties than the acetoxy group (8-OAc), as observed, among others, in the compound pairs **ES45B**/**ES45A**, **ES27B**/**ES27A**, and **ES20B**/**ES20A**. The presence of the OH group was associated with a lower IC_{50} value, which may have resulted from improved binding ability to biological targets or increased polarity, facilitating cellular penetration. However, this relationship was not entirely clear-cut—in some cases, such as **ES25B**/**ES25A** and **ES26B**/**ES26A**, the differences in activity were modest or even reversed, depending on the cell line. This finding suggests that the effectiveness of the hydroxyl group may depend on the presence of other substituents, their interactions, and the molecular characteristics of the specific cell line. Compounds containing nitro (NO_2) substituents on the phenyl ring demonstrated particularly strong activity, which is consistent with our previous work.[19,27] The presence of these groups resulted in the lowest IC_{50} values across the entire compound set. Compound **ES45B**, containing an NO_2 group in both the ortho and para positions of the phenyl ring and an 8-OH group in the quinoline, was the most active compound in the entire series, demonstrating an IC_{50} of 0.26 μM against the U-251 cell line. High activity of this compound was also observed in the LN-18 (2.90 μM) and U-87 MG (1.13 μM) cell lines, suggesting that the presence of two NO_2 groups on the phenyl ring significantly enhanced the anticancer activity. Compounds with a single nitro substituent were characterized by lower, but still significant, activity. For example, the **ES25A** derivative demonstrated activity against all the lines, including the resistant T98G line (18.36 μM), while **ES26A** showed moderate activity against LN-18, LN-229, and U-87 MG. Comparison of these data indicates that the presence of a single NO_2 group may be sufficient for a moderate biological effect, while the system with two nitro groups acts synergistically, especially in the context of appropriately selected other substituents (e.g., OH at the 8-position of quinoline).

It is also worth noting the patterns of inactivity in the studied series. Certain substituent combinations appear to significantly reduce the biological activity of the compounds, which may indicate their particularly unfavorable structural profile. For example, the presence of a fluorine group at the ortho position of the phenyl ring (e.g., **ES18B** or **ES24A**) correlated with inactivity in most cell lines, suggesting that fluorine, despite its frequent presence in drug design, may interfere with interactions with the molecular target at this position or negatively impact the pharmacokinetic properties of the molecule. In comparison, substitution of the ortho position of the phenyl ring with iodine (**ES29B**) or chlorine (e.g., **ES5**, **ES58**, and **ES20B**) correlated with moderate to high biological activity in various cancer lines. These results may indicate that heavier halogens in this position, unlike fluorine, favor interactions with the biological target, probably due to steric effects, polarizability, and their potential to create halogen bonding interactions. A similar effect is illustrated by the comparison of compounds **ES26A** and **ES55A**. Both contained a nitro group at the same position (3-NO_2), while **ES55A** differed from **ES26A** only in the presence of an additional acetoxy group (2-OAc). Despite this minor structural difference, the biological activity of **ES55A** decreased significantly, compared to **ES26A**, suggesting that the introduction of the OAc group to the ortho position of the

https://doi.org/10.1021/acsmedchemlett.5c00526
ACS Med. Chem. Lett. 2026, 17, 351−357

phenyl ring negatively impacted the activity profile (see also compound **ES17B**), probably by increasing steric hindrance or adversely affecting the electronic properties of the molecule. Such cases highlight the importance of substituent interactions and their spatial arrangement for biological efficacy. Inactive compounds thus offer valuable insight into the structural boundaries of this class and serve as a useful reference point for the future design of improved analogues.

Promising results for the SQ activity on GBM lines were the basis for conducting research on the inhibition of receptor tyrosine kinases. The experiments were performed on a panel of kinases (the Kinase Selectivity TK-1 Profiling System and ADP-Glo Kinase Assay from Promega), and only those for which inhibition occurred to the highest degree are presented here. As shown in Table 2, interactions between IGF1R and specific 2-SQ derivatives varied significantly. Several compounds (marked in green and yellow)—namely, **ES2B**, **ES45A**, **ES58**, and **ES45B**—exhibited strong inhibitory potential, reducing IGF1R activity by 51.59%−62.95% at a concentration of 1 μM.

The remaining compounds (marked in orange and red) inhibited IGF1R activity to a lesser extent (ranging from 6.35 to 18.66% at the same concentration). Further analysis of the chemical structures revealed that the presence and number of nitro groups influence a compound's inhibitory potential. We therefore hypothesized that the presence of two nitro groups, as in the case of the two strongest inhibitors (**ES45A** and **ES45B**), may noticeably alter the molecule's charge distribution, enhancing its affinity for IGF1R.

In order to confirm this preliminary hypothesis and evaluate structural details of the inhibitory potential of SQs against the IGF1R kinase, we performed molecular docking studies. Given the 2-SQ scaffold, we targeted compounds toward the kinase orthosteric ATP binding pocket. From several available structures crystallized with small molecule inhibitors, we selected structures in the IGF1R unphosphorylated inactive conformation (PDB ID: 3O23), originally cocrystallized with hydantoin inhibitor. Schrodinger's Induced Fit Docking (IFD) protocol, which allows for a certain extent of amino acid side chain and protein backbone adaptation upon docking, resulted in the molecular poses depicted in Figure 2 and Figure S1.

The docking results revealed that high inhibitory potency was strongly correlated with the formation of multiple, diverse interactions within the kinase active site. The most potent inhibitors—**ES2B**, **ES45A**, **ES58**, and **ES45B**—exhibited inhibition greater than 50% at 1 μM concentration, correlating with the number and quality of protein−ligand contacts. For example, **ES2B** formed a hydrogen bond between the gatekeeper Met1082 backbone N−H and the acetoxy substituent on the phenyl ring, while also enabling the backbone carbonyl of Val1063 to accept a hydrogen bond from the hydroxyquinoline O−H, providing a critical dual anchoring effect (Figure 2A). The **ES58** interaction was characterized by Lys1033 (β3) donating a side chain N−H hydrogen bond to the quinoline N atom, complemented by a halogen bond between the Met1082 backbone N−H and a chlorine substituent on the phenyl ring (Figure 2B). **ES45A** stood out by forming three key hydrogen bonds: Lys1033 interacted with both the quinoline N and the acetoxy group (8-OAc) on the quinoline ring, while Met1082 formed a hydrogen bond with the NO_2 substituent on the phenyl ring (Figure 2C). In **ES45B**, the Met1082 backbone N−H formed a halogen bond with a Cl atom on the quinoline, and the positively charged Lys1033 side chain electrostatically interacted with a negatively charged O-substituent on the quinoline (Figure 2D). Moderately active compounds, such as **ES20B** and **ES28B**, relied on dual interactions via a halogen bond (Met1082 N−H to Cl on quinoline) and Lys1033-mediated electrostatic attraction to an O- on quinoline, while **ES29B** uniquely combined Lys1033−O- binding with a T-shaped $\pi-\pi$ stacking interaction between its phenyl ring and the Phe1131 side chain, the latter imparting additional activity (Figure S1A−C). In contrast, the least active compounds (**ES25A**, **ES25B**, and **ES26B**) were limited to a single hydrogen bond or charge−charge interaction involving Lys1033 and their respective substituents (Figure S1D−F).

Collectively, these findings demonstrate that potent IGF1R kinase inhibition depends on a multiplicity of complementary binding interactions, particularly those engaging gatekeeper Met1082 and Lys1033 (β3), such as combined hydrogen bonds, halogen bonds, electrostatic contacts, and aromatic stacking, while reliance on only one type of interaction results in markedly reduced activity. The graph showing the correlation between the results of molecular docking and ex vivo experiments proves the consistency of these data (Figure 3). These results indicate that the main skeleton of SQ has the characteristics of a privileged structure, which, when decorated with substituents in an appropriate manner, forms a pharmacophore that exhibits strong interaction with IGF1R.

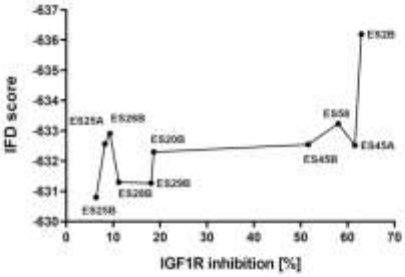

Figure 3. Graph showing the relationship between the in silico scoring of the tested compounds to IGF1R unphosphorylated inactive conformation and the% inhibition determined in vitro.

■ ASSOCIATED CONTENT

Data Availability Statement

Data are available at zenodo.org/records/17404684.

Supporting Information

The Supporting Information is available free of charge at https://pubs.acs.org/doi/10.1021/acsmedchemlett.5c00526.

Supporting Information is available at Material and methods, including Molecular docking, Cell culture, Cytotoxicity studies, and Kinase activity inhibition. Additional figures are also provided (PDF)

■ AUTHOR INFORMATION

Corresponding Author

Anna Mrozek-Wilczkiewicz − *A. Chełkowski Institute of Physics, University of Silesia in Katowice, 41-500 Chorzów, Poland; Department of Systems Biology and Engineering,*

https://doi.org/10.1021/acsmedchemlett.5c00526
ACS Med. Chem. Lett. 2026, 17, 351−357

Silesian University of Technology, Akademicka 16, 44-100 Gliwice, Poland; orcid.org/0000-0003-2228-1475; Email: anna.mrozek-wilczkiewicz@us.edu.pl

Authors

Patryk Zioła – *A. Chełkowski Institute of Physics, University of Silesia in Katowice, 41-500 Chorzów, Poland*

Katarzyna Malarz – *A. Chełkowski Institute of Physics, University of Silesia in Katowice, 41-500 Chorzów, Poland;* orcid.org/0000-0003-4283-3126

Marcin Pacholczyk – *Department of Systems Biology and Engineering, Silesian University of Technology, Akademicka 16, 44-100 Gliwice, Poland*

Wioleta Cieślik – *Institute of Chemistry, University of Silesia in Katowice, 41-500 Chorzów, Poland*

Patrycja Rawicka – *A. Chełkowski Institute of Physics, University of Silesia in Katowice, 41-500 Chorzów, Poland*

Robert Musiol – *Institute of Chemistry, University of Silesia in Katowice, 41-500 Chorzów, Poland*

Complete contact information is available at: https://pubs.acs.org/10.1021/acsmedchemlett.5c00526

Author Contributions

Patryk Zioła: Investigation, Methodology, Writing – original draft. **Katarzyna Malarz**: Investigation, Methodology, Supervision. **Marcin** – original draft. Patrycja Rawicka: Methodology, Data curation. **Robert Musiol**: Resources, Writing – original draft. **Anna Mrozek-Wilczkiewicz**: Conceptualization, Funding acquisition, Supervision, Writing – original draft.

Funding

This work was supported by the National Science Centre grant 2020/39/O/NZ5/02342.

Notes

The authors declare no competing financial interest.

■ ABBREVIATIONS

IGF1R = insulin-like growth factor 1 receptor
RTK = receptor tyrosine kinaseGBM glioblastoma multiforme
IR = insulin receptor
SQ = styrylquinoline
EGFR = epidermal growth factor receptor
SAR = structure–activity relationship
IFD = Induced Fit Docking

■ REFERENCES

(1) Simpson, A.; Petnga, W.; Macaulay, V. M.; Weyer-Czernilofsky, U.; Bogenrieder, T. Insulin-Like Growth Factor (IGF) Pathway Targeting in Cancer: Role of the IGF Axis and Opportunities for Future Combination Studies. *Target Oncol.* **2017**, *12* (5), 571–597.

(2) Li, R.; Pourpak, A.; Morris, S. W. Inhibition of the insulin-like growth factor-1 receptor (IGF1R) tyrosine kinase as a novel cancer therapy approach. *J. Med. Chem.* **2009**, *52* (16), 4981–5004.

(3) Ma, Y.; Tang, N.; Thompson, R. C.; Mobley, B. C.; Clark, S. W.; Sarkaria, J. N.; Wang, J. InsR/IGF1R Pathway Mediates Resistance to EGFR Inhibitors in Glioblastoma. *Clin. Cancer Res.* **2016**, *22* (7), 1767–1776.

(4) Crudden, C.; Song, D.; Cismas, S.; Trocme, E.; Pasca, S.; Calin, G. A.; Girnita, A.; Girnita, L. Below the Surface: IGF-1R Therapeutic Targeting and Its Endocytic Journey. *Cells* **2019**, *8* (10), 1223.

(5) Turvey, S. J.; McPhillie, M. J.; Kearney, M. T.; Muench, S. P.; Simmons, K. J.; Fishwick, C. W. G. Recent developments in the structural characterisation of the IR and IGF1R: implications for the design of IR-IGF1R hybrid receptor modulators. *RSC Med. Chem.* **2022**, *13* (4), 360–374.

(6) Mulvihill, M. J.; Cooke, A.; Rosenfeld-Franklin, M.; Buck, E.; Foreman, K.; Landfair, D.; O'Connor, M.; Pirritt, C.; Sun, Y.; Yao, Y.; et al. Discovery of OSI-906: a selective and orally efficacious dual inhibitor of the IGF-1 receptor and insulin receptor. *Future Med. Chem.* **2009**, *1* (6), 1153–1171.

(7) Luffy, M.; Ganz, A. L.; Wagner, S.; Wolf, J.; Ropertz, J.; Zeidan, R.; Kent, J. D.; Douglas, R. S.; Kahaly, G. J. Linsitinib inhibits proliferation and induces apoptosis of both IGF-1R and TSH-R expressing cells. *Front. Immunol.* **2024**, *15*, 1488220.

(8) Boutin, A.; Eliseeva, E.; Templin, S.; Marcus-Samuels, B.; Anderson, D. E.; Gershengorn, M. C.; Neumann, S. Linsitinib Decreases Thyrotropin-Induced Thyroid Hormone Synthesis by Inhibiting Crosstalk Between Thyroid-Stimulating Hormone and Insulin-Like Growth Factor 1 Receptors in Human Thyrocytes In Vitro and In Vivo in Mice. *Thyroid* **2025**, *35* (2), 216–224.

(9) Tognon, C. E.; Sorensen, P. H. Targeting the insulin-like growth factor 1 receptor (IGF1R) signaling pathway for cancer therapy. *Expert Opin. Ther. Targets* **2012**, *16* (1), 33–48.

(10) Xia, Y.; Jin, L.; Zhang, B.; Xue, H.; Li, Q.; Xu, Y. The potentiation of curcumin on insulin-like growth factor-1 action in MCF-7 human breast carcinoma cells. *Life Sci.* **2007**, *80* (23), 2161–2169.

(11) Waraky, A.; Akopyan, K.; Parrow, V.; Stromberg, T.; Axelson, M.; Abrahmsen, L.; Lindqvist, A.; Larsson, O.; Aleem, E. Picropodophyllin causes mitotic arrest and catastrophe by depolymerizing microtubules via insulin-like growth factor-1 receptor-independent mechanism. *Oncotarget* **2014**, *5* (18), 8379–8392.

(12) Bao, X. H.; Naomoto, Y.; Hao, H. F.; Watanabe, N.; Sakurama, K.; Noma, K.; Motoki, T.; Tomono, Y.; Fukazawa, T.; Shirakawa, Y.; et al. IGF-IR and its inhibitors in gastrointestinal carcinomas (Review). *Oncol. Lett.* **2010**, *1* (1), 195–201.

(13) Bergqvist, M.; Holgersson, G.; Bondarenko, I.; Grechanaya, E.; Maximovich, A.; Andor, G.; Klockare, M.; Thureson, M.; Jerling, M.; Harmenberg, J. Phase II randomized study of the IGF-1R pathway modulator AXL1717 compared to docetaxel in patients with previously treated, locally advanced or metastatic non-small cell lung cancer. *Acta Oncol.* **2017**, *56* (3), 441–447.

(14) Szczepaniak, J.; Cieslik, W.; Romanowicz, A.; Musiol, R.; Krasowska, A. Blocking and dislocation of Candida albicans Cdr1p transporter by styrylquinolines. *Int. J. Antimicrob. Agents* **2017**, *50* (2), 171–176.

(15) Musiol, R.; Jampilek, J.; Buchta, V.; Silva, L.; Niedbala, H.; Podeszwa, B.; Palka, A.; Majerz-Maniecka, K.; Oleksyn, B.; Polanski, J. Antifungal properties of new series of quinoline derivatives. *Bioorg. Med. Chem.* **2006**, *14* (10), 3592–3598.

(16) Musiol, R. Styrylquinoline - A Versatile Scaffold in Medicinal Chemistry. *Med. Chem.* **2020**, *16* (2), 141–154.

(17) Malarz, K.; Mularski, J.; Kuczak, M.; Mrozek-Wilczkiewicz, A.; Musiol, R. Novel Benzenesulfonate Scaffolds with a High Anticancer Activity and G2/M Cell Cycle Arrest. *Cancers (Basel)* **2021**, *13* (8), 1790.

(18) Mrozek-Wilczkiewicz, A.; Spaczynska, E.; Malarz, K.; Cieslik, W.; Rams-Baron, M.; Krystof, V.; Musiol, R. Design, Synthesis and In Vitro Activity of Anticancer Styrylquinolines. The p53 Independent Mechanism of Action. *PLoS One* **2015**, *10* (11), No. e0142678.

(19) Mrozek-Wilczkiewicz, A.; Kuczak, M.; Malarz, K.; Cieslik, W.; Spaczynska, E.; Musiol, R. The synthesis and anticancer activity of 2-styrylquinoline derivatives. A p53 independent mechanism of action. *Eur. J. Med. Chem.* **2019**, *177*, 338–349.

(20) Papaconstantinou, J. Insulin/IGF-1 and ROS signaling pathway cross-talk in aging and longevity determination. *Mol. Cell. Endocrinol.* **2009**, *299* (1), 89–100.

(21) El-Sayed, M. A.; El-Husseiny, W. M.; Abdel-Aziz, N. I.; El-Azab, A. S.; Abuelizz, H. A.; Abdel-Aziz, A. A. Synthesis and biological evaluation of 2-styrylquinolines as antitumour agents and EGFR kinase inhibitors: molecular docking study. *J. Enzyme Inhib Med. Chem.* **2018**, *33* (1), 199–209.

(22) Mularski, J.; Malarz, K.; Pacholczyk, M.; Musiol, R. The p53 stabilizing agent CP-31398 and multi-kinase inhibitors. Designing, synthesizing and screening of styrylquinazoline series. *Eur. J. Med. Chem.* **2019**, *163*, 610−625.
(23) Malarz, K.; Kuczak, M.; Rurka, P.; Rawicka, P.; Boguszewska-Czubara, A.; Jampilek, J.; Mularski, J.; Musiol, R.; Mrozek-Wilczkiewicz, A. Unveiling the role of Ndrg1 gene on the oxidative stress induction behind the anticancer potential of styrylquinazoline derivatives. *Sci. Rep.* **2025**, *15* (1), 16081.
(24) Malarz, K.; Mularski, J.; Pacholczyk, M.; Musiol, R. Styrylquinazoline derivatives as ABL inhibitors selective for different DFG orientations. *J. Enzyme Inhib. Med. Chem.* **2023**, *38* (1), 2201410.
(25) Moriev, R.; Vasylchenko, O.; Platonov, M.; Gryguzenko, O.; Volkova, K.; Zozulya, S. Identification of Novel IGF1R Kinase Inhibitors by Molecular Modeling and High-Throughput Screening. *Acta Naturae* **2013**, *5* (2), 90−99.
(26) Fan, C.; Huang, Y. X.; Bao, Y. L.; Sun, L. G.; Wu, Y.; Yu, C. L.; Zhang, Y.; Song, Z. B.; Zheng, L. H.; Sun, Y.; et al. Virtual screening of specific insulin-like growth factor 1 receptor (IGF1R) inhibitors from the National Cancer Institute (NCI) molecular database. *Int. J. Mol. Sci.* **2012**, *13* (12), 17185−17209.
(27) Kuczak, M.; Cieslik, W.; Musiol, R.; Mrozek-Wilczkiewicz, A. 4-Furanylvinylquinoline derivative as a new scaffold for the design of oxidative stress initiator and glucose transporter inhibitor drugs. *Sci. Rep.* **2024**, *14* (1), 28454.

https://doi.org/10.1021/acsmedchemlett.5c00526
ACS Med. Chem. Lett. 2026, 17, 351−357

5. OŚWIADCZENIA WSPÓŁAUTORÓW

dr hab. Anna Mrozek-Wilczkiewicz, prof. UŚ

Instytut Fizyki im. Augusta Chełkowskiego

Wydział Nauk Ścisłych i Technicznych

Uniwersytet Śląski w Katowicach

ul. 75 Pułku Piechoty 1A

41-500 Chorzów

Chorzów, 22.05.2026

OŚWIADCZENIE

Oświadczam, że w pracy:

> **[P1].** Malarz K., Zioła P., Zych D., Rurka P., Mrozek-Wilczkiewicz A.: **„ Imbalance of redox homeostasis and altered cellular signaling induced by the metal complexes of terpyridine",** *Scientific Reports*, 2024, **14**, 26951

mój udział polegał na przygotowaniu hipotezy badawczej, omówieniu wyników oraz pisaniu manuskryptu.

> **[P2].** Zioła P., Malarz K., Rawicka P., Korzec M., Serda M., Boguszewska-Czubara A., Pacholczyk M., Książek M., Mrozek-Wilczkiewicz A.: **„The multifaceted mechanism of action of quinoline thiosemicarbazone based on disruption of iron homeostasis and selective IGF1R inhibition leading to oxidative stress induction",** *Biomedicine & Pharmacotherapy*, 2025, **192**, 118692

mój udział polegał na przygotowaniu hipotezy badawczej, zaplanowaniu eksperymentów, omówieniu wyników oraz pisaniu manuskryptu.

> **[P3].** Zioła P., Malarz K., Pacholczyk M., Cieślik W., Rawicka P., Musioł R., Mrozek-Wilczkiewicz A.: **„Styrylquinoline Derivatives as IGF1R Inhibitors",** *ACS Medicinal Chemistry Letters*, 2026, **17(2)**, 351-357

mój udział polegał na przygotowaniu hipotezy badawczej, pozyskaniu finansowania, nadzorze merytorycznym prowadzonych eksperymentów oraz pisaniu manuskryptu.

Signature Not Verified
Dokument podpisany przez Anna Mrozek-Wilczkiewicz
Data: 2026.05.22 11:39:47 CEST

Podpis

dr Katarzyna Malarz, prof. UŚ

Instytut Fizyki im. Augusta Chełkowskiego

Wydział Nauk Ścisłych i Technicznych

Uniwersytet Śląski w Katowicach

ul. 75 Pułku Piechoty 1A

41-500 Chorzów

Chorzów, 15.05.2026

OŚWIADCZENIE

Oświadczam, że w pracy:

> **[P1].** Malarz K., Zioła P., Zych D., Rurka P., Mrozek-Wilczkiewicz A.: **„ Imbalance of redox homeostasis and altered cellular signaling induced by the metal complexes of terpyridine",** *Scientific Reports*, 2024, **14**, 26951

mój udział polegał na zaprojektowaniu eksperymentów, wykonaniu badań cytotoksyczności i zatrzymania cyklu komórkowego, analizie wyników badań oraz pisaniu manuskryptu.

> **[P2].** Zioła P., Malarz K., Rawicka P., Korzec M., Serda M., Boguszewska-Czubara A., Pacholczyk M., Książek M., Mrozek-Wilczkiewicz A.: **„The multifaceted mechanism of action of quinoline thiosemicarbazone based on disruption of iron homeostasis and selective IGF1R inhibition leading to oxidative stress induction",** *Biomedicine & Pharmacotherapy*, 2025, **192**, 118692

mój udział polegał na wykonaniu badań inhibicji aktywności kinaz i powinowactwa wiązania z wykorzystaniem metody termoforezy mikroskalowej (MST), analizie uzyskanych wyników oraz na merytorycznym nadzorze nad prowadzonymi eksperymentami.

> **[P3].** Zioła P., Malarz K., Pacholczyk M., Cieślik W., Rawicka P., Musioł R., Mrozek-Wilczkiewicz A.: **„Styrylquinoline Derivatives as IGF1R Inhibitors",** *ACS Medicinal Chemistry Letters*, 2026, **17(2)**, 351-357

mój udział polegał na opracowaniu metodologii, wykonaniu badań inhibicji aktywności kinaz, oraz na merytorycznym nadzorze nad prowadzonymi eksperymentami.

Podpis

dr Wioleta Cieślik

Instytut Chemii

Wydział Nauk Ścisłych i Technicznych

Uniwersytet Śląski w Katowicach

ul. 75 Pułku Piechoty 1A

41-500 Chorzów

Chorzów, 17.05.2026

OŚWIADCZENIE

Oświadczam, że w pracy:

> **[P3].** Zioła P., Malarz K., Pacholczyk M., Cieślik W., Rawicka P., Musioł R., Mrozek-Wilczkiewicz A.: **„Styrylquinoline Derivatives as IGF1R Inhibitors",** *ACS Medicinal Chemistry Letters*, 2026, **17(2)**, 351-357

mój udział obejmował przeprowadzenie analizy zależności struktura–aktywność (SAR) badanych pochodnych styrylochinoliny oraz współudział w opracowaniu i pisaniu manuskryptu.

Cieślik Wioleta

Podpis

dr hab. Mateusz Korzec, prof. UŚ
Instytut Chemii
Wydział Nauk Ścisłych i Technicznych
Uniwersytet Śląski w Katowicach
ul. Szkolna 9
40-006 Katowice

Katowice, 17.05.2026

OŚWIADCZENIE

Oświadczam, że w pracy:

> **[P2].** Zioła P., Malarz K., Rawicka P., Korzec M., Serda M., Boguszewska-Czubara A., Pacholczyk M., Książek M., Mrozek-Wilczkiewicz A.: **„The multifaceted mechanism of action of quinoline thiosemicarbazone based on disruption of iron homeostasis and selective IGF1R inhibition leading to oxidative stress induction",** *Biomedicine & Pharmacotherapy*, 2025, **192**, 118692

mój udział polegał na syntezie badanych tiosemikarbazonów.

Podpis

Korzec Mateusz

dr Maria Książek

Instytut Fizyki im. Augusta Chełkowskiego

Wydział Nauk Ścisłych i Technicznych

Uniwersytet Śląski w Katowicach

ul. 75 Pułku Piechoty 1A

41-500 Chorzów

Chorzów, 20.05.2026

OŚWIADCZENIE

Oświadczam, że w pracy:

> **[P2].** Ziola P., Malarz K., Rawicka P., Korzec M., Serda M., Boguszewska-Czubara A., Pacholczyk M., Książek M., Mrozek-Wilczkiewicz A.: **„The multifaceted mechanism of action of quinoline thiosemicarbazone based on disruption of iron homeostasis and selective IGF1R inhibition leading to oxidative stress induction”,** *Biomedicine & Pharmacotherapy*, 2025, **192**, 118692

mój udział polegał na wykonaniu rentgenowskich pomiarów strukturalnych monokryształów związku MS168 oraz rozwiązaniu i udokładnieniu struktury krystalicznej tego związku.

Maria Książek

Podpis

UNIWERSYTET ŚLĄSKI
W KATOWICACH

prof. dr hab. Robert Musioł
Instytut Chemii
Uniwersytet Śląski w Katowicach
Szkolna 9, 40-007 Katowice

Katowice, 18.05.2026

OŚWIADCZENIE

Oświadczam, że w pracy:

[P3]. Zioła P., Malarz K., Pacholczyk M., Cieślik W., Rawicka P., Musioł R., Mrozek-Wilczkiewicz A.: **„Styrylquinoline Derivatives as IGF1R Inhibitors”,** *ACS Medicinal Chemistry Letters*, 2026, **17(2)**, 351-357

mój udział polegał na projektowaniu syntezy badanych styrylochinolin, częściowej analizie wyników oraz pisaniu manuskryptu.

Podpis

Uniwersytet Śląski w Katowicach
Wydział Nauk Ścisłych i Technicznych
Instytut Chemii
ul. Szkolna 9, 40-006 Katowice
tel. 32 359 15 45, e-mail: ich.wnst@us.edu.pl
www.us.edu.pl/instytut/ich

dr Patrycja Rawicka

Instytut Fizyki im. Augusta Chełkowskiego

Wydział Nauk Ścisłych i Technicznych

Uniwersytet Śląski w Katowicach

ul. 75 Pułku Piechoty 1A

41-500 Chorzów

Chorzów, 15.05.2026

OŚWIADCZENIE

Oświadczam, że w pracy:

> **[P2].** Zioła P., Malarz K., Rawicka P., Korzec M., Serda M., Boguszewska-Czubara A., Pacholczyk M., Książek M., Mrozek-Wilczkiewicz A.: **„The multifaceted mechanism of action of quinoline thiosemicarbazone based on disruption of iron homeostasis and selective IGF1R inhibition leading to oxidative stress induction"**, *Biomedicine & Pharmacotherapy*, 2025, **192**, 118692

mój udział polegał na zaplanowaniu, współudziale, nadzorze merytorycznym i analizie wyników badań chelatacji.

> **[P3].** Zioła P., Malarz K., Pacholczyk M., Cieślik W., Rawicka P., Musioł R., Mrozek-Wilczkiewicz A.: **„Styrylquinoline Derivatives as IGF1R Inhibitors"**, *ACS Medicinal Chemistry Letters*, 2026, **17(2)**, 351-357

mój udział polegał na opracowaniu metodologii oraz analizie uzyskanych danych.

Podpis

Patrycja Rawicka

mgr Patryk Rurka
Instytut Fizyki im. Augusta Chełkowskiego
Wydział Nauk Ścisłych i Technicznych
Uniwersytet Śląski w Katowicach
ul. 75 Pułku Piechoty 1A
41-500 Chorzów

Chorzów, 18.05.2026 r.

OŚWIADCZENIE

Oświadczam, że w pracy:

> **[P1]**. Malarz K., Zioła P., Zych D., Rurka P., Mrozek-Wilczkiewicz A.: **„ Imbalance of redox homeostasis and altered cellular signaling induced by the metal complexes of terpyridine"**, *Scientific Reports*, 2024, **14**, 26951

mój udział polegał na wykonania badań cytotoksyczności z dodatkiem przeciwutleniaczy, pomiaru ilości reaktywnych form tlenu oraz ekspresji genów.

Podpis

dr hab. Maciej Serda, prof. UŚ
Instytut Chemii
Wydział Nauk Ścisłych i Technicznych
Uniwersytet Śląski w Katowicach
ul. 75 Pułku Piechoty 1A
41-500 Chorzów

Chorzów, 15.05.2026

OŚWIADCZENIE

Oświadczam, że w pracy:

> **[P2].** Zioła P., Malarz K., Rawicka P., Korzec M., Serda M., Boguszewska-Czubara A., Pacholczyk M., Książek M., Mrozek-Wilczkiewicz A.: **„The multifaceted mechanism of action of quinoline thiosemicarbazone based on disruption of iron homeostasis and selective IGF1R inhibition leading to oxidative stress induction",** *Biomedicine & Pharmacotherapy*, 2025, **192**, 118692

mój udział polegał na syntezie badanych tiosemikarbazonów.

Podpis

Digitally signed by Maciej Serda
Date: 2026.05.15 14:12:49 CEST

Opole, 18.05.2026

dr hab. inż. Dawid Zych, prof. UO
Instytut Chemii
Wydział Chemii i Farmacji
Uniwersytet Opolski
ul. Oleska 48
45-052 Opole

OŚWIADCZENIE

Oświadczam, że w pracy:

> **[P1].** Malarz K., Zioła P., Zych D., Rurka P., Mrozek-Wilczkiewicz A.: **„Imbalance of redox homeostasis and altered cellular signaling induced by the metal complexes of terpyridine"**, *Scientific Reports*, 2024, **14**, 26951

mój udział polegał na zaplanowaniu oraz wykonaniu syntez badanych terpirydyn.

Dawid Zych

6. LITERATURA

1. Bray F, Laversanne M, Sung H, Ferlay J, Siegel RL, Soerjomataram I, et al. Global cancer statistics 2022: GLOBOCAN estimates of incidence and mortality worldwide for 36 cancers in 185 countries. CA Cancer J Clin. 2024;74(3):229-63.
2. Abbott NJ, Patabendige AA, Dolman DE, Yusof SR, Begley DJ. Structure and function of the blood-brain barrier. Neurobiol Dis. 2010;37(1):13-25.
3. Smyth LCD, Kipnis J. Redefining CNS immune privilege. Nat Rev Immunol. 2025;25(10):766-75.
4. Upton DH, Ung C, George SM, Tsoli M, Kavallaris M, Ziegler DS. Challenges and opportunities to penetrate the blood-brain barrier for brain cancer therapy. Theranostics. 2022;12(10):4734-52.
5. Delgado-Lopez PD, Corrales-Garcia EM. Survival in glioblastoma: a review on the impact of treatment modalities. Clin Transl Oncol. 2016;18(11):1062-71.
6. Ostrom QT, Patil N, Cioffi G, Waite K, Kruchko C, Barnholtz-Sloan JS. CBTRUS Statistical Report: Primary Brain and Other Central Nervous System Tumors Diagnosed in the United States in 2013-2017. Neuro Oncol. 2020;22(12 Suppl 2):iv1-iv96.
7. Kleihues P, Ohgaki H. Primary and secondary glioblastomas: from concept to clinical diagnosis. Neuro Oncol. 1999;1(1):44-51.
8. Kanu OO, Hughes B, Di C, Lin N, Fu J, Bigner DD, et al. Glioblastoma Multiforme Oncogenomics and Signaling Pathways. Clin Med Oncol. 2009;3:39-52.
9. Pombo Antunes AR, Scheyltjens I, Duerinck J, Neyns B, Movahedi K, Van Ginderachter JA. Understanding the glioblastoma immune microenvironment as basis for the development of new immunotherapeutic strategies. Elife. 2020;9:e52176.
10. Pouyan A, Ghorbanlo M, Eslami M, Jahanshahi M, Ziaei E, Salami A, et al. Glioblastoma multiforme: insights into pathogenesis, key signaling pathways, and therapeutic strategies. Mol Cancer. 2025;24(1):58.
11. Andreini C, Putignano V, Rosato A, Banci L. The human iron-proteome. Metallomics. 2018;10(9):1223-31.
12. Teh MR, Armitage AE, Drakesmith H. Why cells need iron: a compendium of iron utilisation. Trends Endocrinol Metab. 2024;35(12):1026-49.
13. Szlasa W, Gachowska M, Kiszka K, Rakoczy K, Kiełbik A, Wala K, et al. Iron chelates in the anticancer therapy. Chemical Papers. 2021;76(3):1285-94.
14. Galy B, Conrad M, Muckenthaler M. Mechanisms controlling cellular and systemic iron homeostasis. Nat Rev Mol Cell Biol. 2024;25(2):133-55.
15. Torti SV, Torti FM. Iron and Cancer: 2020 Vision. Cancer Res. 2020;80(24):5435-48.
16. Schonberg DL, Miller TE, Wu Q, Flavahan WA, Das NK, Hale JS, et al. Preferential Iron Trafficking Characterizes Glioblastoma Stem-like Cells. Cancer Cell. 2015;28(4):441-55.
17. Merlot AM, Kalinowski DS, Kovacevic Z, Jansson PJ, Sahni S, Huang ML, et al. Exploiting Cancer Metal Metabolism using Anti-Cancer Metal- Binding Agents. Curr Med Chem. 2019;26(2):302-22.
18. Trujillo-Alonso V, Pratt EC, Zong H, Lara-Martinez A, Kaittanis C, Rabie MO, et al. FDA-approved ferumoxytol displays anti-leukaemia efficacy against cells with low ferroportin levels. Nat Nanotechnol. 2019;14(6):616-22.
19. Trenker R, Jura N. Receptor tyrosine kinase activation: From the ligand perspective. Curr Opin Cell Biol. 2020;63:174-85.
20. Adams TE, Epa VC, Garrett TP, Ward CW. Structure and function of the type 1 insulin-like growth factor receptor. Cell Mol Life Sci. 2000;57(7):1050-93.

21. Turvey SJ, McPhillie MJ, Kearney MT, Muench SP, Simmons KJ, Fishwick CWG. Recent developments in the structural characterisation of the IR and IGF1R: implications for the design of IR-IGF1R hybrid receptor modulators. RSC Med Chem. 2022;13(4):360-74.
22. Ebrahimi N, Fardi E, Ghaderi H, Palizdar S, Khorram R, Vafadar R, et al. Receptor tyrosine kinase inhibitors in cancer. Cell Mol Life Sci. 2023;80(4):104.
23. Yin S, Girnita A, Stromberg T, Khan Z, Andersson S, Zheng H, et al. Targeting the insulin-like growth factor-1 receptor by picropodophyllin as a treatment option for glioblastoma. Neuro Oncol. 2010;12(1):19-27.
24. Hagerstrand D, Lindh MB, Pena C, Garcia-Echeverria C, Nister M, Hofmann F, et al. PI3K/PTEN/Akt pathway status affects the sensitivity of high-grade glioma cell cultures to the insulin-like growth factor-1 receptor inhibitor NVP-AEW541. Neuro Oncol. 2010;12(9):967-75.
25. A Phase 1 Clinical Trial of Oral Gallium Maltolate for the Treatment of Relapsed and Refractory Glioblastoma [Internet]. 2020. Available from: https://clinicaltrials.gov/study/NCT04319276.
26. A Phase 0 Clinical Trial of Oral Gallium Maltolate for Recurrent Glioblastoma [Internet]. 2026. Available from: https://clinicaltrials.gov/study/NCT07515924.
27. Guerrero-Lopez P, Martin-Pardillos A, Bonet-Aleta J, Mosseri A, Hueso JL, Santamaria J, et al. 2D versus 3D tumor-on-chip models to study the impact of tumor organization on metabolic patterns in vitro. Sci Rep. 2025;15(1):19506.
28. D'Aprile S, Denaro S, Lavoro A, Candido S, Giallongo S, Torrisi F, et al. Glioblastoma mesenchymal subtype enhances antioxidant defence to reduce susceptibility to ferroptosis. Sci Rep. 2024;14(1):20770.
29. Malarz K, Zych D, Gawecki R, Kuczak M, Musiol R, Mrozek-Wilczkiewicz A. New derivatives of 4'-phenyl-2,2':6',2''-terpyridine as promising anticancer agents. Eur J Med Chem. 2021;212:113032.

7. AKTYWNOŚĆ NAUKOWA

Publikacje nie wchodzące w skład rozprawy doktorskiej:

1. Orszulak L., Lamrani T., Tarnacka M., Hachuła B., Jurkiewicz K., **Zioła P.,** Mrozek-Wilczkiewicz A., Kamińska E., Kamiński K.; The Impact of Various Poly (vinylpyrrolidone) Polymers on the Crystallization Process of Metronidazole; *Pharmaceutics*; 2024; 16(1); 136; https://doi.org/10.3390/pharmaceutics16010136 (pkt. $MNiSW_{2026}$= 100; IF_{2024}=5.5)
2. Orszulak L., Lamrani T., Bernat R., Tarnacka M., Zakowiecki D., Jurkiewicz K., **Zioła P.,** Mrozek-Wilczkiewicz A., Zieba A., Kaminski K., Kaminska E.; The Influence of PVP Polymer Topology on the Liquid Crystalline Order of Itraconazole in Binary Systems; *Molecular Pharmaceutics*; 2024; 21(6); 3027-3039; https://doi.org/10.1021/acs.molpharmaceut.4c00215 (pkt. $MNiSW_{2026}$= 140; IF_{2024}=4.5)
3. Dudek K., Strach A., Wasilkowski D., Łosiewicz B., Kubisztal J., Mrozek-Wilczkiewicz A., **Zioła P.,** Barylski A.; Comparison of Key Properties of Ag-TiO2 and Hydroxyapatite-Ag-TiO2 Coatings on NiTi SMA; *Journal of Functional Biomaterials*; 2024; 15(9); 264; https://doi.org/10.3390/jfb15090264 (pkt. $MNiSW_{2026}$= 100; IF_{2024}=5.2)
4. Malarz K., Borzęcka W., **Zioła P.,** Domiński A., Rawicka P., Bialik-Wąs K., Kurcok P., Torres T., Mrozek-Wilczkiewicz A.; pH-sensitive phthalocyanine-loaded polymeric nanoparticles as a novel treatment strategy for breast cancer; *Bioorganic Chemistry*; 2025; 155; 108127; https://doi.org/10.1016/j.bioorg.2025.108127 (pkt. $MNiSW_{2026}$= 100; IF_{2024}=4.7)
5. Rurka P., Mularski J., **Zioła P.,** Boguszewska-Czubara A., Jampilek J., Mrozek-Wilczkiewicz A., Malarz K.; An insight into the anticancer potential of sulfonated styrylquinazolines as multifunctional agents targeting microtubules; *Bioorganic Chemistry*; 2026; 170; 109517; https://doi.org/10.1016/j.bioorg.2026.109517 (pkt. $MNiSW_{2026}$= 100; IF_{2024}=4.7)

Prezentacje posterów na konferencjach naukowych:

1. **Zioła P.,** Malarz K., Zych D., Mrozek-Wilczkiewicz A. "Antiproliferative ability of new terpyridine complexes". XXV Gliwice Scientific Meetings, 19-20.11.2021, Gliwice
2. **Zioła P.,** Malarz K., Zych D., Rurka P., Mrozek-Wilczkiewicz A. "Anticancer properties of terpyridine derivatives complexed with metal ions". 9th Young Medicinal Chemist Symposium; 08-09.09.2022, Nicea, Francja
3. **Zioła P.,** Malarz K., Serda M., Pacholczyk M., Mrozek-Wilczkiewicz A. "Multifaceted mechanism of action of thiosemicarbazone derivatives: inhibition of tyrosine kinases and generation of reactive oxygen species". 11th Young Medicinal Chemist Symposium; 05-06.09.2024, Rzym, Włochy
4. **Zioła P.,** Malarz K., Serda M., Pacholczyk M., Mrozek-Wilczkiewicz A. "Quinoline thiosemicarbazones as anticancer agents: tyrosine kinase inhibition and reactive oxygen species generation". XXVIII Gliwice Scientific Meetings, 21-22.11.2024, Gliwice

Wystąpienia ustne na konferencjach naukowych:

1. **Zioła P.,** Malarz K., Zych D., Rurka P., Mrozek-Wilczkiewicz A. "Właściwości antynowotworowe pochodnych kompleksów terpirydyny z jonami metali". IX Śląskie Spotkania Naukowe; 27-28.05 2022, Istebna

2. **Zioła P.,** Malarz K., Borzęcka W., Domiński A., Rawicka P., Torres T., Kowalczuk M., Mrozek-Wilczkiewicz A. "Polimeryczne nanocząstki kompleksujące ftalocyjaniny obiecującą nową metodą leczenia nowotworu piersi". X Śląskie Spotkania Naukowe; 19-21.05 2023, Pokrzywna

3. **Zioła P.,** Malarz K., Serda M., Pacholczyk M., Mrozek-Wilczkiewicz A. "Wielopłaszczyznowy mechanizm działania pochodnych z grupy tiosemikarbazonu – wpływ na generowanie stresu oksydacyjnego oraz inhibicja kinaz tyrozynowych". XI Śląskie Spotkania Naukowe; 17-19.05.2024, Ustroń

4. **Zioła P.,** Malarz K., Rawicka P., Korzec M., Serda M., Boguszewska-Czubara A., Pacholczyk M., Książek M., Mrozek-Wilczkiewicz A. "Wielokierunkowy mechanizm działania chinolinowych pochodnych tiosemikarbazonów – inhibicja

IGF1R oraz indukcja stresu oksydacyjnego prowadząca do ferroptozy". XII Śląskie Spotkania Naukowe; 9-11.05.2025, Złoty Potok

Staże naukowe:

1. Staż naukowy w zespole badawczym „Preclinical Molecular Imaging" pod kierunkiem prof. Gabrieli Kramer-Marek, 01.09-01.12.2023, The Institute of Cancer Research (ICR), Londyn, Wielka Brytania

Projekty:

1. Anna Mrozek-Wilczkiewicz, PRELUDIUM BIS 2 (2020/39/O/NZ5/02342). Chelatory żelaza jako inhibitory kinaz tyrozynowych - nowa strategia leczenia glejaka wielopostaciowego – **wykonawca**